Krishna Dutta
Archana Mallik
H. R. Kotadia
S. Das   *Editors*

# Processing and Characterization of Materials

Select Proceedings of ICPCM 2021

Springer

# Springer Proceedings in Materials

## Volume 26

**Springer Proceedings in Materials** publishes the latest research in Materials Science and Engineering presented at high standard academic conferences and scientific meetings. It provides a platform for researchers, professionals and students to present their scientific findings and stay up-to-date with the development in Materials Science and Engineering. The scope is multidisciplinary and ranges from fundamental to applied research, including, but not limited to:

- Structural Materials
- Metallic Materials
- Magnetic, Optical and Electronic Materials
- Ceramics, Glass, Composites, Natural Materials
- Biomaterials
- Nanotechnology
- Characterization and Evaluation of Materials
- Energy Materials
- Materials Processing

To submit a proposal or request further information, please contact one of our Springer Publishing Editors according to your affiliation:

European countries: **Mayra Castro** (mayra.castro@springer.com)
India, South Asia and Middle East: **Priya Vyas** (priya.vyas@springer.com)
South Korea: **Smith Chae** (smith.chae@springer.com)
Southeast Asia, Australia and New Zealand: **Ramesh Nath Premnath** (ramesh.premnath@springer.com)
The Americas: **Michael Luby** (michael.luby@springer.com)
China and all the other countries or regions: **Mengchu Huang** (mengchu.huang@springer.com)

This book series is indexed in **SCOPUS** database.

Krishna Dutta · Archana Mallik · H. R. Kotadia · S. Das
**Editors**

# Processing and Characterization of Materials

Select Proceedings of ICPCM 2021

🪄 Springer

*Editors*
Krishna Dutta
Department of Metallurgical and Materials
Engineering
NIT Rourkela
Odisha, India

Archana Mallik
Department of Metallurgical and Materials
Engineering
NIT Rourkela
Rourkela, India

H. R. Kotadia
School of Engineering
Liverpool John Moores University
Liverpool, UK

S. Das
Department of Metallurgical and Materials
Engineering
NIT Raipur
Chhattisgarh, India

# Contents

# About the Editors

**Dr. Krishna Dutta** is currently working as an associate professor at the Department of Metallurgical and Materials Engineering, National Institute of Technology Rourkela, Odisha, India. He obtained his B.E. (Metallurgical Engineering) from Jadavpur University, Kolkata, India; M.Tech. (Materials and Metallurgical Engineering) from the Indian Institute of Technology, Kanpur, and Ph.D. (Metallurgical and Materials Engineering) from Indian Institute of Technology, Kharagpur. His major areas of research interest include fatigue and fracture behaviour of metals and alloys, ratcheting, ratcheting–creep interaction, laser surface modification, spot-welds, high-entropy alloys, and composites. He has published 45 peer-reviewed international research papers in science citation-indexed journals, about 15 conference proceeding papers and two book chapters. Dr. Dutta is a life member of the Indian Institute of Metals.

**Dr. Archana Mallik** is currently working as an associate professor at the Department of Metallurgical and Materials Engineering, National Institute of Technology Rourkela, Odisha, India. She received her B.Tech. degree from Indira Gandhi Institute of Technology, Sarang, Odisha in 2002 and M.Tech. from Indian Institute of Technology BHU UP in 2004. Then after, she completed her Ph.D. degree in Metallurgical and Materials Engineering from National Institute of Technology Rourkela in the year 2010. Dr. Archana Mallik has authored more than 70 international and national scientific publications. She is also a member of several professional bodies including editorial advisory boards. She is a regular referee of various prestigious journals. She has delivered several invited talks in national conferences and institutions. Prof. Archana's research has been funded by different governmental agencies including CSIR, BRNS, and SERB India.

**Dr. H. R. Kotadia** is working as an associate professor in School of Engineering Liverpool John Moores University, UK. He has done his undergraduate studies from the M.S. University, Baroda, India, masters from University of Sheffield, Sheffield, UK, and Ph.D. Brunel University London, UK. He has profound understanding of fundamental material science and engineering challenges in metallic materials.

He has published over 60 peer-reviewed articles in reputable international journals and conferences. His research has led to real industrial impact through the development of new alloys and processing. Through his work, he has established and will continue to establish an extensive network with renowned academics in the UK, Germany, France, USA, Australia, Japan, China, Malaysia, and India, and companies in the UK, South Korea and Netherland including JLR, Henkel Technologies, Dynex Semiconductor, Schlumberger, AWE, Novelis, Hydro, TATA, and POSCO.

**Dr. S. Das** is currently working as an associate professor at the Department of Metallurgical and Materials Engineering, National Institute of Technology Raipur, Chhattisgarh, India. He obtained his undergraduate as well as masters (in Metallurgical Engineering) from Bengal Engineering and Science University, Kolkata, India, and doctorate degree from the Indian Institute Technology from Indian Institute Technology, Kharagpur. His major areas of research interests include casting and solidification of aluminium and magnesium alloys as well as designing of casting equipment. He has several years of research experiences from South Korea, Sweden, and BCAST London, UK. He has published around 65 peer-reviewed international research papers in science citation-indexed journals and conference proceeding papers. He is also a life member of various scientific organizations. His research has been funded by several industrial as well as national and international bodies.

# In-House Electrochemical Synthesis of Graphene and Its Exploration as an Anticorrosive Coating on Copper

**Siddhanta Sekhar Mishra, Subhendra Keshari Sahoo, Biswajit Biswal, Amlan Das , and Archana Mallik**

**Abstract** 2D materials have created quite an impetus in the field of material science. From the carbon family, graphene has emerged as a unique productive material, which has found use in multiple applications. Graphene's outstanding physical and chemical characteristics have created high interest among researchers to use in the field of nanoscience. Humanity has for long been plagued by the metal killer "corrosion"; posing severe economical and technological losses. With the discovery of graphene, a ray of hope has gleamed for corrosion prevention techniques. The present work focusses on the synthesis of FLGNs (few layered graphene nanosheets) via electrochemical exfoliation of pyrolitic graphite and its application as a coating material. Characterization techniques were employed to confirm the presence of graphene and to observe the morphology of the graphene layers. Coating of FLGNs on copper strips was performed through electrochemical deposition. The corrosion behaviour and coating stability of the coated sample were analysed by means of PDP (Potentiodynamic polarization) and EIS (Electrochemical Impedance Spectroscopy) tests. Furthermore, AFM, FESEM and Profilometer give glimpses about the surface roughness and morphology of the coated samples. The surface roughness increment after the corrosion test of different samples and the Tafel plot shows the effect of coating on corrosion behaviour and how it can be improved under suitable conditions.

**Keywords** FLGNs · Exfoliation · PDP · EIS · Tafel plots · Randel's circuit

## 1 Introduction

Corrosion has been a tedious question mark for all industrial applications owing to its severe implications. India alone loses around 7% of its GDP (Gross Domestic Product) annually due to corrosion. There is a need to develop non-toxic and sustainable methods for counteracting corrosion. Graphene bears relevance to the current

S. S. Mishra · S. K. Sahoo · B. Biswal · A. Das · A. Mallik (✉)
Electrometallurgy and Corrosion Laboratory, National Institute of Technology, Rourkela, Odisha, India
e-mail: archananitrkl@gmail.com

work due to its impermeable nature and chemical stability. Bunch et al. fabricated a graphene sealed microchamber to test it impermeability to gases like helium [1]. Graphene's geometric pore is around 0.064 nm, which makes molecular passage difficult. The inert behaviour of graphene is the basis for protective coatings against corrosion. Till date, graphene has been synthesized through various techniques like mechanical-based exfoliation, liquid-based exfoliation, chemical synthesis, epitaxial growth and vapour deposition routes. However, synthesis of graphene through electrochemical route gives both qualitative and quantitative amount of graphene. The process requires simple instruments without any specific expertise or environmental conditions [2–4]. Various researchers have reported the exfoliation of graphite/ graphite modified electrodes from various ionic electrolytes, which includes acids, organic and inorganic solvents [5–11]. LiCl [12], LiOH [13], LiClO$_4$ [14], LiPF$_6$ [15] have also been used as solvents for cathodic exfoliation approaches that can be explored for synthesizing high-quality GNs. Zhou et al. [16] by using Na+ or dimethyl sulfoxide complexes as intercalation agents reported cathodic exfoliation of graphite electrode. The exfoliated graphite is stabilized by the addition of ionic acetate salt in the electrolyte, which produces few-layer graphene nanosheets. Das et al. [17, 18] have produced FLGNs (few layer graphene nanosheets) from various solvents using low cost methodologies and have discussed it's efficient corrosion protection behaviour. Other authors have also reported graphene's prominence as an anti-corrosive coating [19–21].

The current work discusses the synthesis of graphene from an aqueous mixture of NaOH and H$_2$O$_2$. The obtained graphene was processed further so that it can used for electrophoretic deposition onto copper strips. Synthesized FLGNs have been characterized using XRD and SEM. Corrosion and impedance tests of coated samples conducted in chloride solutions show lower current densities for coated copper. The stability of the coating layer is examined by EIS test. FTIR, SEM, AFM and profilometer analysis have also been carried out to characterize the coated samples.

## 2 Experimental Methodology

Pyrolytic graphite sheet (99% pure) was cut into required dimensions of 15 cm × 1 cm × 0.3 cm and was cleaned with acetone. Non-conductive tapes were applied onto graphite rods to prevent exfoliation of the entire graphite electrode (which may lead to non-uniform exfoliation). The electrodes were subjected to pre-cathodic treatment by applying a voltage of 3 V for 10 min using a DC power supply. This was done to remove any physically adsorbed impurities of the graphite electrode, increase availability of surface pores for efficient intercalation and expansion of graphite lattice. Two sets of experiments were done, one using NaOH as electrolyte, i.e. 5 M NaOH aqueous solution and another aqueous mixture of NaOH and H$_2$O$_2$ (i.e. 5 M NaOH + 0.1 M H$_2$O$_2$) as electrolyte. Exfoliation was observed when potential of 6 V was applied, which continued upto 8 V until the current parameter became high.

After the completion of exfoliation process, the solution was washed with distilled water followed by sonication and centrifugation. Further, the solution was oven dried at 110 °C for 24 h to obtain graphene powders. Figure 1 displays the various stages of the exfoliation process which includes exfoliated graphene rod, graphene colloidal solutions and graphene powders.

The synthesized graphene powder was used to prepare aqueous solution of 0.1, 0.5 and 1 wt.%, respectively, and was sonicated in bath sonicator for 1–1.5 h for mono dispersion of graphene powder in the solution. This solution was used as the electrolyte for the electrochemical coating process. Thin copper (Cu) sheets of dimensions (10 cm × 1 cm × 0.1 cm) were surface polished using emery papers of 1/0, 2/0, 3/0 and 4/0 grades. Care was taken to ensure that no cracks or visible defects were present on the Cu surface before it could be used for coating process. Graphite electrode was used as counter electrode (cathode) and Cu sheet was the working electrode (anode). The area to be coated was exposed to the electrolytic medium and electric current was passed through the electrolyte. The coating process was executed for 15–20 min with an applied voltage of 15–20 V.

Corrosion tests for the coated samples were initialized by subjecting it to 0.1 M NaCl solution environment. The corrosion experiment comprised of a three-electrode system wherein working electrode (WE) was coated Cu sheet, a platinum rod was deployed as counter electrode (CE) and a saturated calomel electrode (SCE) was taken as reference. Initially, 0 V potential was allowed to pass through the circuit
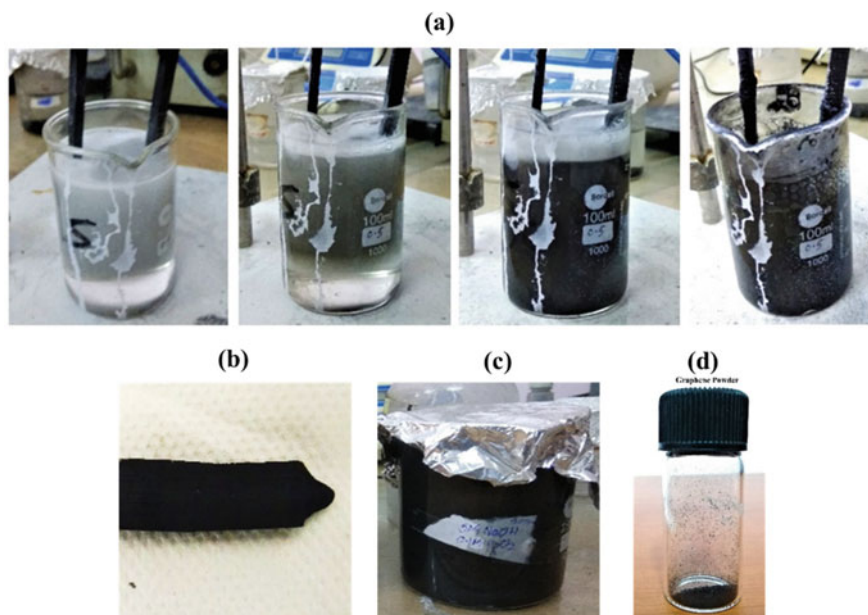


**Fig. 1** **a** Different stages of exfoliation, **b** exfoliated graphite electrode, **c** graphene solution, **d** graphene powder

for 20 min in order to determine the OCP (open circuit potential). Post OCP determination, potentiodynamic polarization test was initiated within a voltage range of −4 V to 2 V to acquire the polarization curve. Tafel extrapolation method gave the corrosion parameters.

## 3 Results and Discussion

### 3.1 *X-ray Diffraction Analysis of Synthesized Graphene*

X-ray diffraction analysis involved the multipurpose XRD system (Rigaku Japan/Ultima-IV). The scan range was fixed to be from 5º to 65º, scan rate 10º/min and step size 0.002. XRD primarily helped in interpreting the structure and comparison of eventual range in the inter-planar expansion of graphite powder and FLGNs. Figure 2 shows intensive peaks at 26.74° corresponding to 002 crystal planes. The intensity of peaks corresponding to 5 M NaOH + 0.1 M $H_2O_2$ FLGNs decreases than that of pure graphite powder while for FLGN synthesized using 5 M NaOH there is a huge drop in intensity at angle 26.70º. This suggests that the number of layers in 5 M NaOH graphene is less in comparison to 5 M NaOH + 0.1 M $H_2O_2$ graphene.

**Fig. 2** XRD plot of graphite, FLGNs exfoliated in NaOH (5 M) + $H_2O_2$ (0.1 M) solution and FLGNs exfoliated in NaOH (5 M) solution
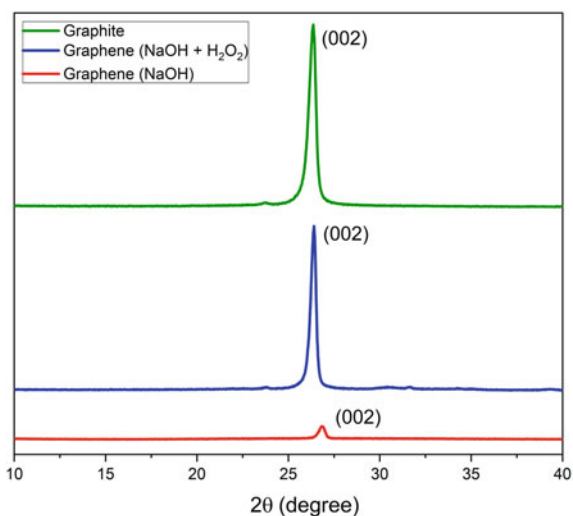
## 3.2 Microstructural Analysis of Synthesized Graphene

Figure 3b and c shows the SEM images, which clearly indicate multi-layered stacked structure of synthesized graphene. Loose bonding of the layers makes the structure more irregular and multiple FLGNs are observed. It can be noted that some exfoliated layers are larger in size which indicates that complete exfoliation and sonication is not achieved. The stacking of the layers with different brightness shows the transparency of the thin layers of graphene. The flakes have a random distribution over the surface and the size distribution of the FLGNs is large. Due to the addition of peroxide ($H_2O_2$) in NaOH solution, the FLGNs produced are uniform and the flakes are comparatively smaller.

After microstructural investigation, energy dispersive spectroscopy (EDS) is employed for specifying the elemental presence in the samples. It is dependent on the interaction of X-rays produced during electron bombardment with the sample. Figure 4a and b shows the characteristic peaks of main elements (C, O) for FLGNs samples of NaOH and NaOH + $H_2O_2$. The percentage of C and O in NaOH is 69.78% and 30.22%, respectively. The percentage of C and O in NaOH + $H_2O_2$ is 65.40% and 34.60%, respectively. EDS points out the presence of oxygen in the graphene powders. This is due to the attachment of oxygen functional groups to the edges of graphene network.

Fourier Transform Infra-Red (FTIR) spectroscopy is instrumental in distinguishing various aspects of chemical bonding. It is utilized on graphite and synthesized graphene powders to confirm the presence of functional groups and type of bond behaviour. Figure 4c represents the FTIR spectra of the three samples. The peaks at different wavelengths are characteristic to different types of bonds. Graphite powder does not show any peak due to the absence of the functional groups and the FLGNs exfoliated in NaOH + $H_2O_2$ solution show rare peaks due to instrumental error. Two very close peaks at 2948.98 cm$^{-1}$ show the C–H bond elongation, and the C–H bending at 1445.32 cm$^{-1}$ shows the hydroxylation of the FLGNs. This shows the separation of the layers and hence the stretching of the bonds due to interlayer pulling. A sharp peak at 839.88 cm$^{-1}$ for the FLGNs exfoliated in NaOH solution
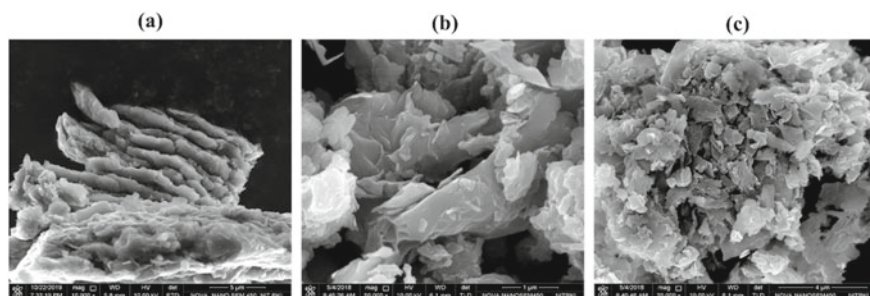


**Fig. 3** **a** SEM image of graphite, **b** SEM image of FLGNs exfoliated in NaOH solution and **c** SEM image of FLGNs exfoliated in NaOH + $H_2O_2$ solution
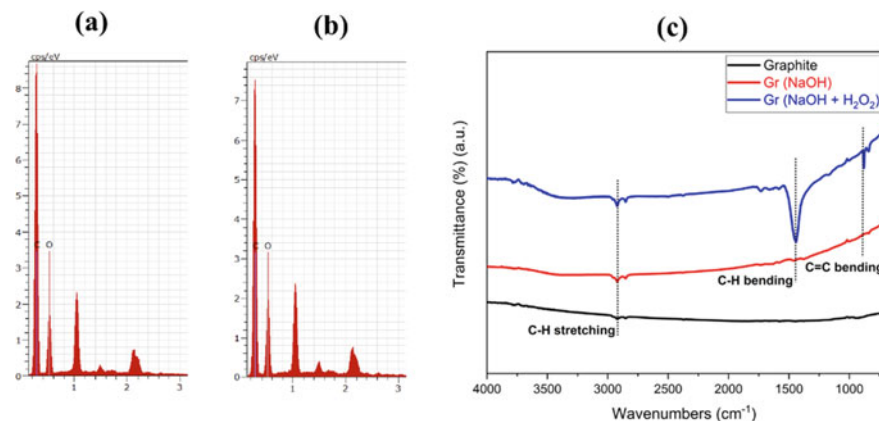
**Fig. 4** **a** EDS of NaOH FLGNs, **b** EDS of NaOH + H$_2$O$_2$ FLGNs and **c** FTIR spectra of graphite and FLGNs

shows C=C bending which may be due to the hexagonal structure damage of the FLGNs in the solution.

### 3.3 Corrosion Thermodynamic and Kinetics Analysis—Linear Sweep Voltammetry

Corrosion is a detrimental phenomenon, which occurs due to reaction of materials with their environment. It is an unalterable reaction, which causes the materials to lose it exiting properties to return to its original natural state.

Figure 5 shows the Tafel plots obtained from the corrosion test. The curve provides a simultaneous view about the behaviour of metal in the corrosive environment, formation of passive layer (which decreases further corrosion) and prediction of corrosion (Tafel extrapolation). All the three samples show passivation behaviour at a voltage above 0.5 V, and the corrosion current is limited to a maximum value beyond which it cannot exceed once the passive layer forms. There is no significant changes in the corrosion behaviour of the coated sample as well as the blank sample, which indicates the non-uniform coating layer formation as depicted in Table 1. The corrosion current is slightly more for graphene-coated Cu sheet (0.5 wt.%), which may be due to the combined effect of coating layer and the oxide layer formation. There is formation of small cavities or pits on the surface of the Cu sheet, which leads to pitting corrosion. The coating on Cu may lose adherence due to the absence of a binding agent as a result, the layer can easily rip off the sample when it is exposed to the chloride medium.

**Fig. 5** Polarization curve for the samples during corrosion test
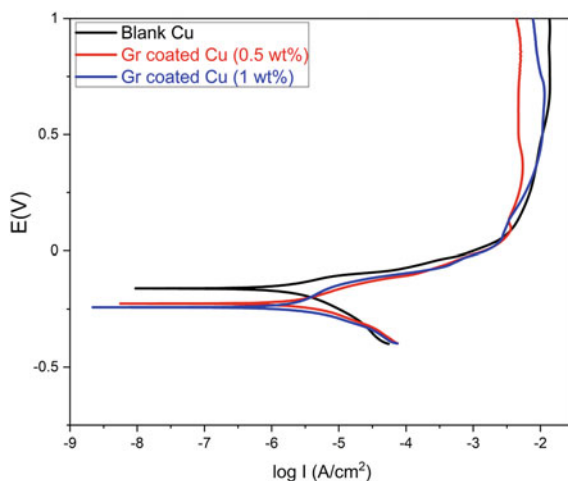


**Table 1** Corrosion data from Tafel fitting of the LSV curves

| Sample | $\beta_a$ | $\beta_c$ | $E_o$ | $I_o$ | Corrosion rate (mm/a) |
|---|---|---|---|---|---|
| Blank Cu sheet | 61.622 | 145.31 | −0.160 | $2.47 \times 10^{-6}$ | 0.029 |
| Graphene-coated Cu sheet (0.5 wt.%) | 80.309 | 105.24 | −0.226 | $2.32 \times 10^{-6}$ | 0.027 |
| Graphene-coated Cu sheet (1 wt.%) | 124.06 | 95.938 | −0.242 | $1.93 \times 10^{-6}$ | 0.022 |

## 3.4 Film Stability Analysis—Electrochemical Impedance Spectroscopy

The stability of the coating layer is scrutinized through EIS test and the data are represented via Nyquist plot and the Bode plot. The nature of the curve from both the plots helps us determine the solution resistance, stability of the oxide layer or the coated layer. In Fig. 6, Nyquist plot shows the stability and the resistance to corrosion. In the X axis, the solution resistance increases as we shift from origin to right. So, more bending of the arc in case of blank Cu shows the increment in the solution resistance and hence its corrosion resistance is higher. Coated sample shows very little arc length, which shows that the corrosion resistance in the coated sample is less due to non-uniform coating layer formation on the copper surface. Figure 7 shows the variation in impedance with the change in frequency. As it can be seen, the impedance is much higher for blank copper showing its high corrosion resistance and it decreases for the coated sample. In addition, there is more variation of the impedance as we increase frequency.
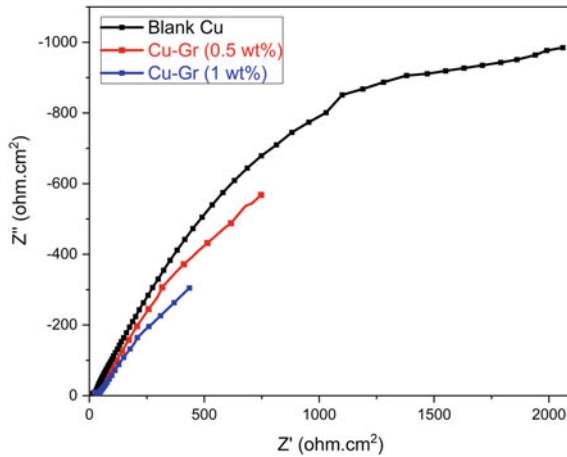
**Fig. 6** Nyquist plot of the EIS test
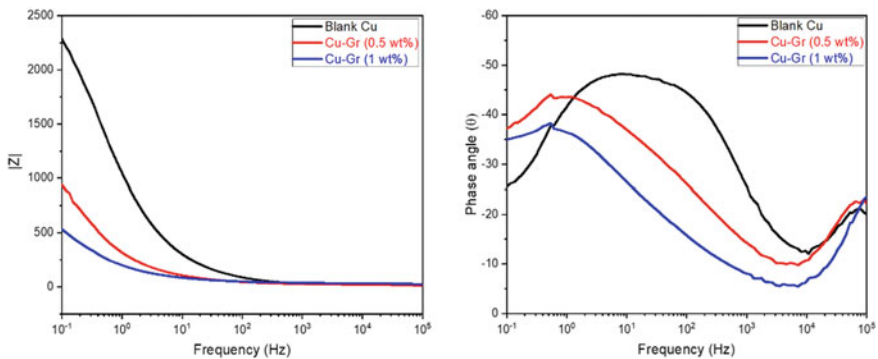


**Fig. 7** Bode plot of the EIS test

## 3.5 Visual Analysis of Graphene-Coated Copper (Before and After Corrosion)

Figure 8 presents a visual comparison of coated samples with bare copper.

The surface gets a prominent dark appearance with an increase in the concentration of graphene in the solution. The coating is seen to be more uniform in 1 wt.% solution.

The occurrence of a greenish layer on the surface is indicative of the oxide layer formation. The oxide is mainly copper oxide, which is originally black in colour but after reacting with moisture it forms a greenish compound, patina. The oxide layer is observed to be more greenish in Cu coating (0.5 wt.% graphene solution) and more blackish in Cu coating (1 wt.% graphene solution).
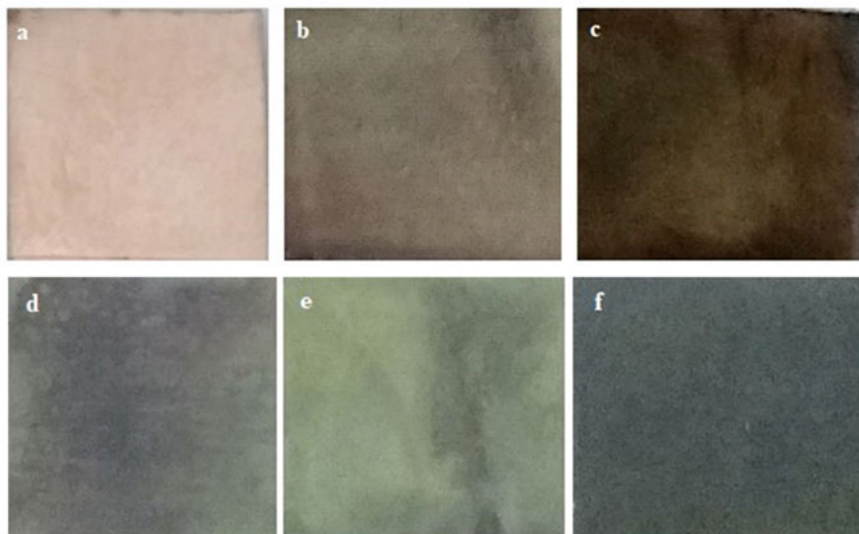
**Fig. 8** Before corrosion **a** Blank copper, **b** Cu coating done in 0.5 wt.% graphene solution, **c** Cu coating done in 1 wt.% graphene solution; after corrosion **d** Blank copper, **e** Cu coating done in 0.5 wt.% graphene solution and **f** Cu coating done in 1 wt.% graphene solution

### 3.6 Morphological Analysis of Graphene-Coated Copper (Before and After Corrosion)

Figure 9 shows SEM images for the three samples, wherein uniformity is observed in the surface of blank copper but some irregularities and crack formation are noticed in the coated samples. The coating surface is not uniform and the roughness of the surface is high in the coated sample. In blank copper, the structure is more planar, which is non-existent in the coated samples. The non-uniformity decreases as the concentration of graphene increases in the solution. Figure 10 clearly indicates the oxide layer that forms during corrosion, which is dominant in the microstructure with white flake and needle like structure. In graphene-coated copper sheet, (0.5 wt.%) layered graphite flakes are observed. Also, broad gaps are present within the layers without any pit formation. Graphene-coated Cu sheet (1 wt.%) has the similar structure as that of blank copper. Mixed layers of copper oxide and graphite flakes are also observed.

Figure 11 shows 3D AFM representations of coated sample before corrosion, which displays the height profile of the coating layer. It can be pointed out that the surface irregularity increases with an increase in graphene concentration. The particle size is 0.6 nm for graphene-coated Cu sheet (1 wt.%), which is almost similar to that of graphene coated Cu sheet (0.5 wt.%). The images also show that the uniformity of the coated layer is more for the 1 wt.% solution.
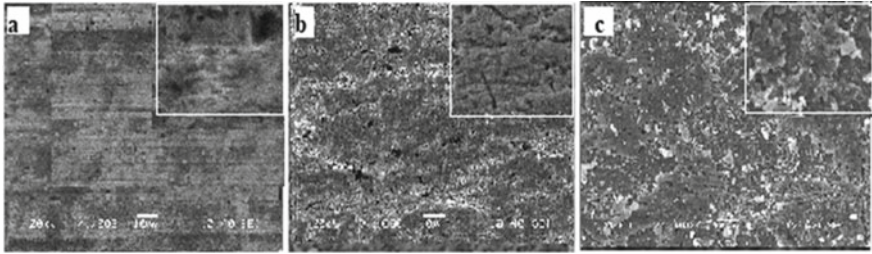
**Fig. 9** SEM image of **a** blank Cu, **b** graphene-coated Cu sheet (0.5 wt.%) and **c** graphene-coated Cu sheet (1 wt.%)
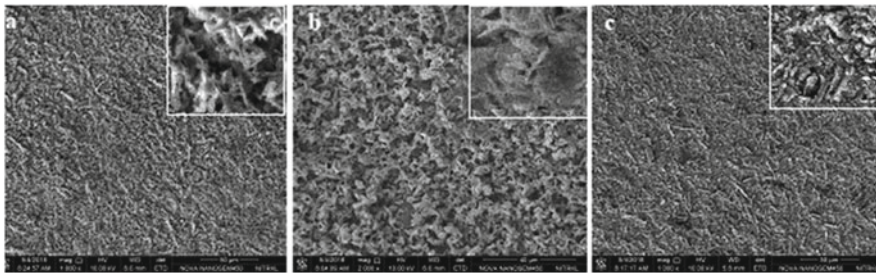


**Fig. 10** FESEM image of **a** blank Cu sheet, **b** graphene-coated Cu sheet (0.5 wt.%) and **c** graphene-coated Cu sheet (1 wt.%) after corrosion
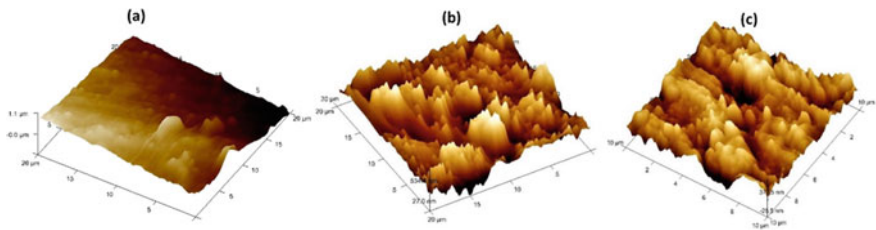


**Fig. 11** AFM images of **a** bare uncoated copper, **b** graphene-coated Cu sheet (0.5 wt.%) and **c** graphene-coated Cu sheet (1 wt.%) before corrosion

The corroded samples in Fig. 12 show a surface roughness increment due to the oxide layer formation. The surface is non-uniform, and this non-uniformity is higher in case of graphene-coated Cu sheet (0.5 wt.%) due to the pre-existence of the non-uniform coating layer and porosity.

Figure 13 shows the surface profile study intended for observing the roughness profiles before corrosion. It is observed that the surface of the coated sample is uneven. The roughness parameter escalates upon increasing the graphene wt.% in the solution, which indicates an increase in coating thickness. Even though there is a
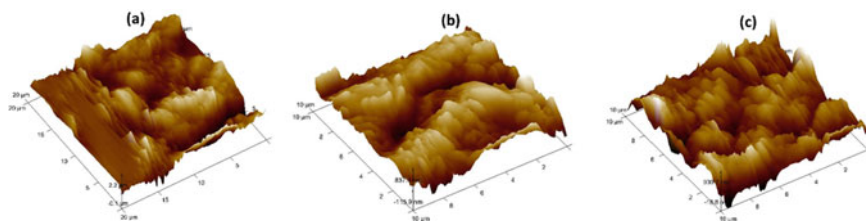
**Fig. 12** AFM images of **a** blank Cu sheet, **b** graphene-coated Cu sheet (0.5 wt.%) and **c** graphene-coated Cu sheet (1 wt.%) after corrosion

decrease in surface uniformity and smoothness, an increment in coating effectiveness is noted.

Figure 14 shows the surface profile analysis and it can be seen that there is more variation in the roughness value indicating the irregularity and non-uniformity of the corroded sample. The roughness value is lowest for blank Cu, i.e. 6242.4 Å and it increases in graphene-coated Cu sheet (0.5 wt.%), i.e. 9976.3 Å and the roughness for graphene-coated Cu sheet (1 wt.%) is 7559.9 Å, which is more than that of the blank Cu. The increment in the roughness is due to the presence of oxide layer and in the coated sample, the coating layer also increases the roughness even more.
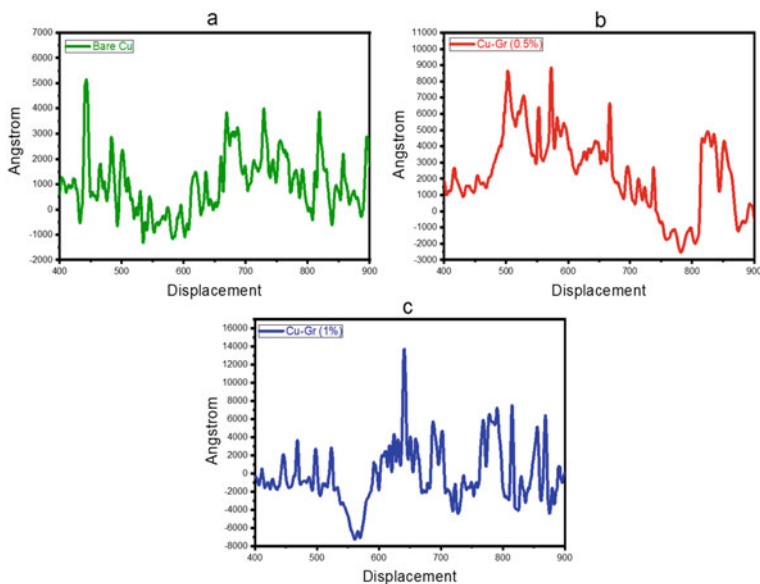


**Fig. 13** Surface roughness profile before corrosion **a** blank Cu sheet, **b** graphene coated Cu sheet (0.5 wt.%), **c** graphene-coated Cu sheet (1 wt.%)
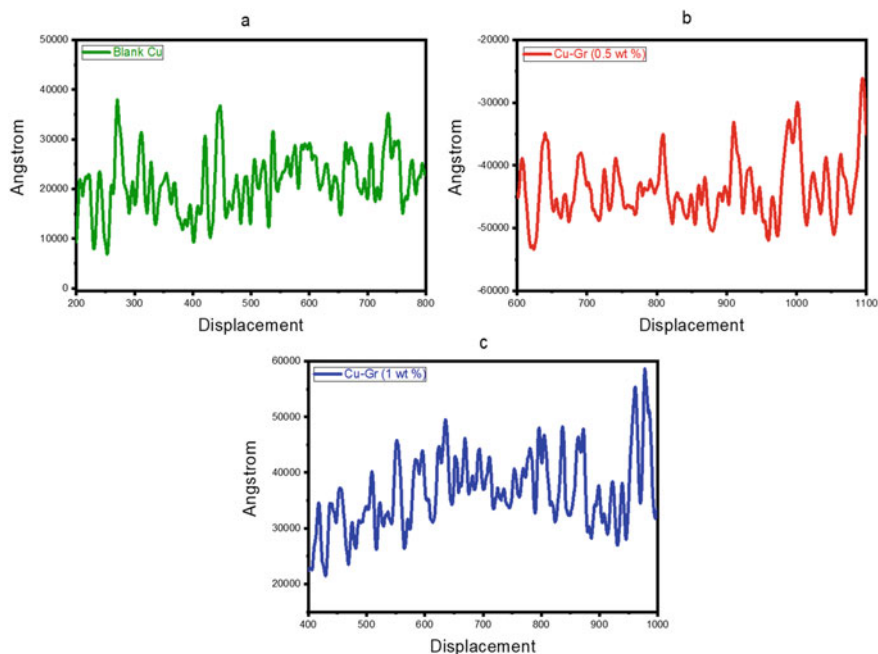
**Fig. 14** Surface profile after corrosion **a** blank Cu after corrosion, **b** graphene-coated Cu sheet (0.5 wt.%) after corrosion and **c** graphene-coated Cu sheet (1 wt.%)

## 3.7 Energy Dispersive Spectroscopy Analysis of Graphene-Coated Samples (Before and After Corrosion)

Figure 15 shows elemental composition of bare copper and graphene-coated copper before corrosion. The presence of C (carbon) peaks points towards graphene, which is almost uniform in both cases. Figure 16 shows different elemental composition of the corroded sample. It can be observed that the Cl content in graphene-coated Cu sheet (0.5 wt.%) is the highest showing high corrosion of the sample. In addition, the oxygen content is more in blank Cu showing more oxide layer formation. Copper content being highest in graphene-coated Cu sheet (1 wt.%) shows less chlorine inclusion, however, no Na was detected in the sample.

(a) Cu – 99%

(b) Cu – 75%, C-25%

(c) Cu-76%, C-24%
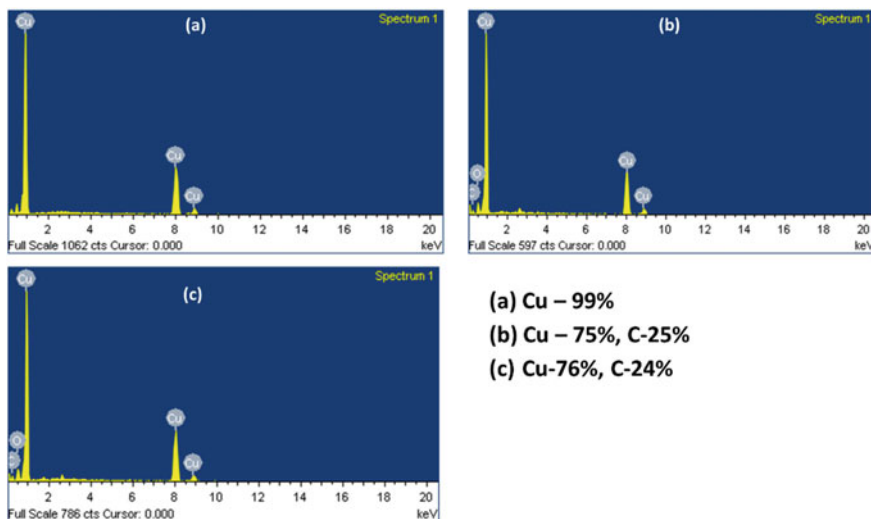
**Fig. 15** EDS spectra before corrosion of **a** bare copper, **b** 0.5% graphene-coated Cu and **c** 1% graphene-coated Cu



| Corroded sample | Elements | | | | |
|---|---|---|---|---|---|
| | Cu | Cl | Na | C | O |
| Blank Cu | 54.31 | 28.07 | 6.51 | - | 11.11 |
| Graphene coated Cu sheet (0.5 wt. %) | 32.92 | 34.26 | 19.14 | 5.95 | 7.73 |
| Graphene coated Cu sheet (1 wt. %) | 64.05 | 24.44 | - | 4.92 | 6.59 |
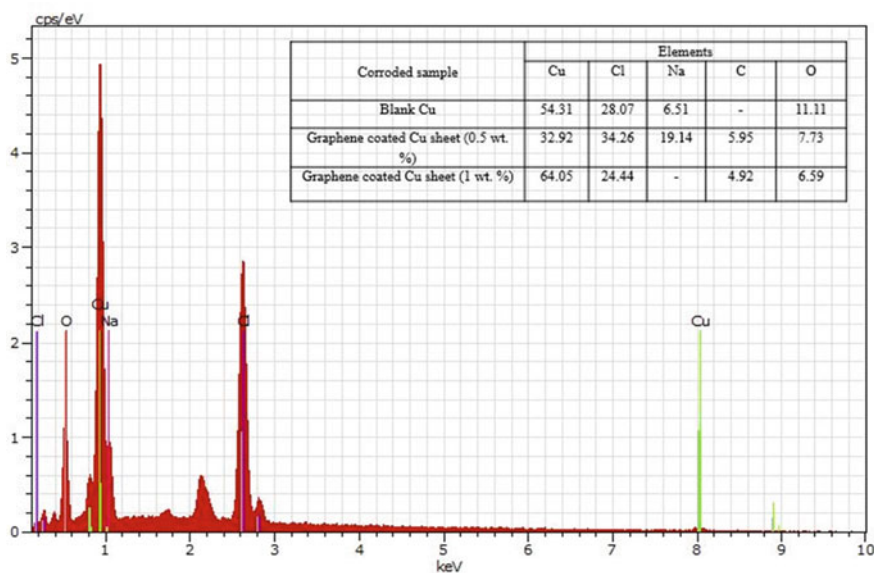
**Fig. 16** EDS spectra of samples after corrosion

## 4 Summary

Graphene was synthesized through electrochemical intercalation of graphite. An easy and green approach, i.e. electrophoretic deposition was used to provide a thin coating of the as-synthesized graphene to provide thin coating layer on copper sheets. The FLGNs produced using NaOH and NaOH + $H_2O_2$ as electrolyte are confirmed through SEM and FESEM. The transparency of the layer shows that the layers are very thin. FTIR spectra show different types of bond stretching and bending for graphene produced through NaOH + $H_2O_2$ solution. In addition, more amount of exfoliated FLGNs were visible in the above electrolyte. The coating for 0.5 wt.% graphene solution showed non-uniform coating whereas for 1 wt.% graphene solution the non-uniformity decreases. In comparison to the uncoated copper sample, the surface roughness for coated sample is more, which shows that the smoothness of the coated layer is less. Due to non-uniformity of the coating layer and less adherence onto the copper surface, the corrosion for coated sample is more. The corrosion can be of pitting in nature if there is presence of defects on the coated layer.

## References

1. Bunch JS, Verbridge SS, Alden JS, Van Der Zande AM, Parpia JM, Craighead HG, McEuen PL (2008) Impermeable atomic membranes from graphene sheets. Nano Lett 8:2458–2462. https://doi.org/10.1021/nl801457b
2. Su C-Y, Lu AY, Xu Y, Chen F-R, Khlobystov AN, Li L-J (2011) High-quality thin graphene films from fast electrochemical exfoliation. ACS Nano 5:2332–2339. https://doi.org/10.1021/nn200025p
3. Krawczyk P, Gurzęda B (2016) Electrochemical properties of exfoliated graphite affected by its two-step modification. J Solid State Electrochem 20:361–369. https://doi.org/10.1007/s10008-015-3051-0
4. Mahato N, Parveen N, Cho MH (2015) Graphene nanodiscs from electrochemical assisted micromechanical exfoliation of graphite: morphology and supramolecular behavior. Mater Express 5:471–479. https://doi.org/10.1166/mex.2015.1270
5. Noel M, Santhanam R, Francisca Flora M (1995) Comparison of fluoride intercalation/de-intercalation processes on graphite electrodes in aqueous and aqueous methanolic HF media. J Power Sources 56:125–131. https://doi.org/10.1016/0378-7753(95)80023-A
6. Kang F, Zhang T-Y, Leng Y (1996) Electrochemical synthesis of sulfate graphite intercalation compounds with different electrolyte concentrations. J Phys Chem Solids 57:883–888. https://doi.org/10.1016/0022-3697(95)00367-3
7. Alliata D, Haring P, Haas O, Kotz R, Siegenthaler H (1999) Anion intercalation into highly oriented pyrolytic graphite studied by electrochemical atomic force microscopy. Electrochem Commun 1:5–9
8. Beck F, Krohn H (1983) Reversible electrochemical intercalation of anions from aqueous solutions in polymer bound graphite electrodes. Synth Met 7:193–199
9. Beck F, Junge H, Krohn H (1981) Graphite intercalation compounds as positive electrodes in galvanic cells. Electrochim Acta 26:799–809
10. Alliata D, Kotz R, Haas O, Siegenthaler H (1999) In situ AFM study of interlayer spacing during anion intercalation into HOPG in aqueous electrolyte. Langmuir 15:8483–8489
11. Skaf DW, Edwards JK (1992) Electrochemical graphite intercalation with nitric acid solution. Synth Met 46:137–145

12. Kamali AR, Fray DJ (2015) Large-scale preparation of graphene by high temperature insertion of hydrogen into graphite. Nanoscale 7:11310–11320. https://doi.org/10.1039/C5NR01132A
13. Huang H, Xia Y, Tao X, Du J, Fang J, Gan Y, Zhang W (2012) Highly efficient electrolytic exfoliation of graphite into graphene sheets based on Li ions intercalation–expansion–microexplosion mechanism. J Mater Chem 22:10452–10456. https://doi.org/10.1039/c2jm00092j
14. Zhang Q, Huang J-Q, Qian W-Z, Zhang Y-Y, Wei F (2013) The road for nanomaterials industry: a review of carbon nanotube production, post-treatment, and bulk applications for composites and energy storage. Small 9:1237–1265. https://doi.org/10.1002/smll.201203252
15. Spahr ME, Palladino T, Wilhelm H, Würsig A, Goers D, Buqa H, Holzapfel M, Novák P (2004) Exfoliation of graphite during electrochemical lithium insertion in ethylene carbonate-containing electrolytes. J Electrochem Soc 151:A1383–A1395. https://doi.org/10.1149/1.1775224
16. Zhou M, Tang J, Cheng Q, Xu G, Cui P, Qin L-C (2013) Few-layer graphene obtained by electrochemical exfoliation of graphite cathode. Chem Phys Lett 572:61–65. https://doi.org/10.1016/j.cplett.2013.04.013
17. Das A, Behera AK, Mallik A (2020) An exploration on anti-corrosion performance of electrochemically synthesized graphene coating on commercially pure copper. Mater Today Proc 33:5341–5347. https://doi.org/10.1016/j.matpr.2020.03.026
18. Das A, Chandran R, Mallik A (2022) Decoration of graphene sheets with silver nanoparticles and their characterization. Mater Today Proc 62:6265–6271. https://doi.org/10.1016/j.matpr.2022.05.521
19. Raza MA, Nadeem A, Ilyas MT (2018) Corrosion study of boron nitride nanosheets deposited on copper metal by electrophoretic deposition. Springer International Publishing, Cham. https://doi.org/10.1007/978-3-319-72526-0
20. Kiran NU, Dey S, Singh BP, Besra L (2017) Graphene coating on copper by electrophoretic deposition for corrosion prevention. Coatings 7:214. https://doi.org/10.3390/coatings7120214
21. Liu J, Hua L, Li S, Yu M (2015) Graphene dip coatings: an effective anticorrosion barrier on aluminum. Appl Surf Sci 327:241–245. https://doi.org/10.1016/j.apsusc.2014.11.187

# A Comprehensive Review of Adaptive Antibacterial Coatings for Implants, Metallic and Herbal Coating Materials and Implant Biomaterial Characterization

**Konduru Ashok Kumar Raju** and **Amit Biswas**

**Abstract** In the present day, implanted biomaterials are an essential element in trauma and orthopaedic surgery outcomes. However, implant-related infections continue to persist and must be resolved. The development of implant-related illnesses through biofilm is the most fundamental pathogenic act based on the present understanding, which begins as soon as germs adhere to an implant and efficiently protects germs from the immune system and medications. During the last decade, several trials have been undertaken to study the effectiveness of changes in surface adherence to the implant, restrict biofilm formation and offer effective biomaterial preservation killing. To move toward a smart methodology in this promising and challenging subject, gave a point-by-point assessment and remarkable meaning of the numerous innovations that are being explored and are now available. The wide categorization of three surface coating techniques is distinguished. Metallic biomaterials are manufactured materials that are utilized in dental implants, orthopaedic fixations, joint replacements and stents to offer internal support to biological tissues. Implant-related problems such as low integration of implants, inflammation, mechanical instability, death, infection, as well as the resulting longer patient care, discomfort and loss of function. In addition to these surface coatings, also present a brief strategy on various natural antibacterial agents and their extraction processes. Biomaterial characterization is the challenging task of estimating biomaterial. As a result, distinct categorization test techniques are categorized here based on their physical and chemical features. Upcoming researchers can easily select the appropriate characterization method based on their applications.

K. A. K. Raju · A. Biswas (✉)
Center of Excellence in Tissue Engineering, Biomaterials and Tissue Engineering Laboratory, Department of Biotechnology and Medical Engineering, National Institute of Technology, Rourkela, Odisha, India
e-mail: amitb79@gmail.com

K. A. K. Raju
e-mail: kingashok143@gmail.com

# 1 Classification of Antibacterial Coating Technologies

## 1.1 Introduction

Despite the reality that advanced perioperative infection prevention measures like prophylactic antibiotics have reduced significantly the occurrence of infections at surgical sites, up to 2.5% of arthroplasties of the hip and knee; 10% of implementation arthroplasties are still contaminated with the peri-prosthetic [1]. Furthermore, according to a recent study, these statistics may be understated and rising [2], although numerous immunological pathogens are frequently recovered [3]. Periprosthetic joint infection is a catastrophic disease that frequently necessitates implant removal, increasing morbidity and death [4], as well as increasing social and economic expenses [5]. Implant infections arise in complex interactions between several factors, bacterial variety , the kind and microbial type, operating method, implant type and antibacterial immunity. No specified technique can be done in a completely clean atmosphere during the initial few hours of operation and contamination of the operating rooms can occur [6]. The host's immunological defences and the systemic antibiotic immunity are typically overcome the modest bacterial burden at the end of surgery [7], but some patients do acquire an SSI, particularly high-risk patients, whose associated co-morbidities increase 20-fold when compared to the population at large [8–10]. Similarly, more sophisticated surgical procedures have been allied to an improved risk of septic complications [11]. Local antibacterial immunity, such as antibiotic-loaded bone cement or bone grafts [12], is also significant in this instance as implant features such as size, shape, material and intended usage [13]. In light of these findings, the need for effective antibacterial surface production, which restricts surrounding tissues to bacterial growth, migration and proliferation, was highlighted at a recent global consensus workshop on PJI [14]. This study contains a full explanation and unique classification of technology that is now available or under development to reduce infections related to implants in orthopaedics and trauma surgery.

At the same time, any coating approach must demonstrate that it is both short and long-term safety. In clinical practice, it is straightforward and cost-effective to prevent osteointegration interference or to create long-term bacterial resistance [15]. Furthermore, bacterial colonization, microbial production and the formation of a stable mature biofilm barrier all take only a few hours. As a result, any antibacterial protection should be active throughout the surgery.

The surgical implant-related bacterial infection is a substantial clinical concern in the medical industry [16]. According to earlier studies, infection rates after total knee and complete hip arthroplasty are estimated to be 0.5% to 5% and 0.6% to 16%,

respectively. Although the situation has improved in the previous 10 years as a result of improved surgical environments and antibiotics, the prevalence remains high. In the United States, for example, roughly 2.6 million orthopaedic implants are inserted in human bodies each year, with around 112,000 (4.3%) becoming contaminated [17]. Following the incidence of these implant-related illnesses, implant removal becomes increasingly common. Aside from aches and pains, implant-related infections place a financial strain on patients and society at large. With a more diversified culture to manage and treat with antibiotics, the recurrence rate of this illness is also quite high, and, to make matters worse, more malignant antibiotic-resistant bacteria have emerged in recent years as a result of drug overuse. Titanium (Ti) and its alloys were originally used in the aircraft sector because of its low density, high strength, great corrosion resistance, and some heat resistance. Bothe et al. and Leventh et al. are reported on the interactions of a variety of metal implants with bone in the early 1940s, when titanium was first clinically presented to the medical sector [18].

In many medical applications, the Pure Titanium and Ti6Al4V alloys began replacing the very promising class of biomaterials with both stainless steel and cobalt-based alloys [19] after more than half a century of research, particularly in orthopaedic and dental applications. Titanium alloys, on the other hand, have several drawbacks, such as strong chemical reactivity, low thermal conductivity, limited resilience owing to high strength at high temperatures and low machine efficiency or grind ability [20].

## 1.2 Antibacterial Coating Classifications

Antibacterial implant protection on the local level can be done in several ways. In light of clinical criteria and expectations, there is currently no single, widely approved categorization of coating technology, no standard certification techniques and control aspects are relatively inadequate. Antibacterial coatings are divided into three kinds based on how they interact with the surrounding tissues (Table 1).

**Passive surface finishing/modification (PSM)**. All surface chemical and/or structural modifications that limit or reduce bacterial production without releasing bactericidal chemicals into the surrounding tissues are covered in this category.

**Active surface finishing/modification (ASM)**. Pre-incorporated antibacterial agents such as antibiotics, antiseptics, metal ions, or other organic and inorganic chemicals are included in this class of active coatings.

**Local carriers or coatings (LCC)**. To preserve the implant, a biodegradable or non-biodegradable antibacterial carrier or coating is added during or after surgery. The coating might work by dispersing high local concentrations of one or more pre-loaded antibacterial, or it might work directly or additively to kill germs. Antibiotic-loaded polymethylmethacrylate (PMMA) was the first coating technique, and it has been used for many years to maintain joint implants [4].

**Table 1** Antibacterial implant protection techniques are classified as follows [4]

| Method of approach | Characteristics | Illustrations | Limitations |
|---|---|---|---|
| Passive surface finishing/ modifications (PSM) | Control of bacterial adhesion | i. A hydrophilic surface<br>ii. Extremely hydrophobic surface<br>iii. Polymers that are anti-adhesive<br>iv. Surface with nanopatterning<br>v. Albumin is a kind of protein<br>vi. Hydrogels are a kind of gel<br>vii. Biosurfactants are substances that clean the body | i. Antibacterial and antibiofilm action is limited<br>ii. Interference with osteointegration is a possibility<br>iii. Long-term consequences are unknown<br>iv. Regulatory concerns |
| Active surface finishing/ modifications (ASM) | Inorganic | Nanoparticles with silver ions | • Inadequate implant coating<br>• The long-term toxicity is questionable<br>• There is a lack of adaptability and application<br>• Large-scale applications are limited<br>• Induction of bacterial resistance is a possibility<br>• Needs to charge costs |
| | | Another metal (zinc, copper, TiO$_2$, etc.) | • Concerns of long-term toxicity<br>• Regulatory concerns |
| | | Iodine is a non-metal | • Inadequate implant coating<br>• Concerns of long-term toxicity<br>• Massive application is difficult<br>• Regulatory constraints |

**Table 1** (continued)

| Method of approach | Characteristics | Illustrations | Limitations |
|---|---|---|---|
| | | Non-metal ions that aren't metals (grapheme, selenium, etc.) | • Compounds that have not been thoroughly investigated<br>• Press-fit insertion resistance of the coating<br>• The long-term toxicity is unknown<br>• Large-scale implementation is challenging |
| | Organic | Antibiotics that are coated or related | • A novel approach to nail coating<br>• Effects on osteointegration over time<br>• Only one antibiotic (gentamicin) |
| | | Antibiotics with covalent bonds | • Improper implant coatings<br>• The long-term toxicity is uncertain<br>• Large-scale applicability is difficult<br>• Regulatory constraints |
| | | Peptides with antimicrobial properties | There is no information on in vivo or clinical consequences |
| | | Cytokines are proteins that are produced by the immune system | Press-fit implantation strength of a coating |
| | | Biofilm disrupting enzymes and agents | The long-term toxicity is unknown |
| | | Derivatives of chitosan | Large-scale application is difficult |
| | Synthetic | Antimicrobial substances that are not antibiotics, Smart coatings | Regulatory constraints |

**Table 1** (continued)

| Method of approach | Characteristics | Illustrations | Limitations |
|---|---|---|---|
| Local carriers or coatings (LCC) | Non-biodegradable | Polymethylmethacrylate with antibiotics | • Induction of resistance and limited variations<br>• There is no antibiofilm impact<br>• Implant coating that isn't complete<br>• It is not recommended for use with cementless implants |
| | Biodegradable | Bone grafts and replacements with antibiotics | • There is a limited supply<br>• As an implant coating, it has not been proved<br>• Cost-effective |
| | | A hydrogel that dissolves quickly | Early clinical application and outcomes |

Although mainly illustrative, this categorization aids in comparing different procedures in clinical practice and in connection to regulatory substance, which should vary per class.

## 2 Metallic Materials and Techniques for Coating

Due to the populations are getting older in advanced nations and patients' wish to keep active at the same level and quality of life, implant use has risen considerably in recent years. As a consequence, demand for high efficiency, implanted biomaterials have steadily increased that may answer specific cardiological, vascular, orthopaedic, traumatic, backbone, dental and injury problems. In fact, in 2012, the biomaterial business amounted to US\$94.1 billion and currently amounts to \$134.3 billion [21]. The diversity and utility of accessible biomaterials and processing and mounting methods into an implanted device have now increased substantially with an extensive range of natural, synthetic and hybrid materials in the market. A range of materials that may be utilized to man-made organs and tissue regeneration were created by the University of California. Metals with the high electrical conductivity, such as electrodes for artificial organs and chemically inert materials used to restore lost

function on a permanent basis, or biodegradable materials, can be used as a temporary framework when tissue and function are able to regenerate.

## 2.1 Metallic Implant Materials

For all bone joint substitutes and dental implants, metal alloys are the most often utilized. The tensile strength and fatigue of most metal implants are improved in orthopaedic surgery than ceramics and polymers. The stainless steel, Cobalt–Chromium (Co–Cr) alloys and titanium and its alloys are among the metals that have been utilized in biomedical implants. The metallic implant applications and mechanical properties are mentioned in Table 2.

**Table 2** Metallic implant mechanical properties and applications

| Biomaterial | Mechanical properties of metals | | | Applications |
|---|---|---|---|---|
| | Young's modulus (GPa) | Tensile strength (MPa) | Hardness (Hv) | |
| Stainless steel | 200 | 510–1351 | 190 | Hip and knee replacements, fracture fixation bone plates, heart valves, dental implants, hip nail, spinal and shoulder prosthesis |
| Titanium and its alloys | 110 | 240–1400 | – | Cochlear substitution, dental implants, orthopaedic implant joint, pacemakers and artificial heart valves, bone and joint replacement |
| Cobalt chromium | 220–230 | 655–1896 | 450 | Total bone and joints replacing (hip and knee), microplates and bone platforms, scrapers, root pacer or suture and orthopaedic implants |
| Alumina | 380 | 249.5–275.1 | 2000–3000 | Artificial replacement for complete articulations, orthodontic anchor and dental implant, femoral components, vertebral spacers and extensors |
| Zirconia | 150–200 | 200–500 | 1000–3000 | Hip, knee, tendon teeth, ligaments, periodontal repair, bone fillings replacement |

### 2.1.1 Stainless Steel

The most often utilized alloys for biomedical purposes like as implants are 316L Stainless Steel and 316LVM (especially for medical applications). The iron, molybdenum, chromium and nickel ions are present in 316L Stainless Steel. The Chromium resist implants from its corrosion and, through a process known as passivation, produces an oxide coating on the metal's surface. 316L has a low carbon content, which indicates that it won't corrode in the body of human. In spite of the corrosion resistance of stainless steel, the chlorine ions can cause it to corrode. Around 90% of 316L stainless steel implants are affected by pitting and cracking. The 316L stainless steel must have ceramic materials coated on the surface for corrosion minimization. Another stainless steel having corrosion-resistant characteristics that has been employed in biomedical applications is 316L VM. Stainless Steel having a Young modulus of 200 GPa due to its different mechanical properties and behaviours. So, it is having larger than bone. Because of its low cost, ease of production and adaptability, stainless steel is only suitable for short-term applications.

### 2.1.2 Cobalt–Chromium (Co–Cr) Alloy

Cobalt-chromium alloys are composed of 58–70% cobalt and 26–30% chromium. In their alpha phase, chromium alloys generate a passivation oxide ($Cr_2O_2$) layer. As a result, even in a chloride environment, it is extremely corrosion resistant. Because of this passivation, Co–Cr is a better long-term option than stainless steel. In complete joint replacement for hips or knees, etc., the mechanical features of Co–Cr such as high strength and good fatigue and wear resistance make it possible, although replacement is not ductile with minimum elongation of 8%. Another often used alloy in implants, particularly for dental applications for long-term usage and the femoral head of joint prosthesis is Co–Cr–Mo (6% molybdenum). Co–Cr has a greater elastic modulus (220–230 GPa) than bone (30 GPa). The release of metal ions, which is a severe disadvantage for cobalt-based alloys, destroys bio-corrosion implants. Ni and Co ions can induce allergy reactions in Co–Ni–Cr–Mo alloys. Neither is, in particular, cancerous and may have severe effects for the metal ions generated. Corrosion products from Co–Cr–Mo are more dangerous than those from stainless steel [22].

### 2.1.3 Titanium and Its Alloys

Since from 1970, the titanium and its alloys have been widely utilized as an implant with characteristics, such as strong mechanical strength, resistance to corrosion, low density and more biocompatibility. It produces a permanent surface oxide layer, which passives and protects against corrosion [23]. Titanium may be alloyed with pure aluminium metal (Al) and vanadium (V). According to the ASTM, pure titanium

is commercially accessible comes in four types of grades (I–IV), containing small proportions of oxygen, hydrogen, nitrogen, carbon, and iron.

The implants' high elastic modulus can cause stress-shielding effects and implant failure. The elastic modulus of titanium implants is 110 GPa, which is lower than that of the stainless steel (210 GPa) and Co–Cr alloys (240 GPa) [24]. The uses for titanium alloys include a few of the application's Joint substitutions, bone fixing, screws, plates, dental implants, cardiac implacers, pacemakers, stents and heart valves. The hexagonal allotropic character of commercially pure titanium (HCP). At 88.2 °C, the hexagon is produced in the α-phase (HPT) and above 88.2 °C and forms a β-focused cubic phase of the body. In order to increase the strength of pure titanium, the metals Al, Ni, Mo, Mn, V, Ta, Nb, CO, Cr, Fe, and Cu are incorporated in the product. There are a variety of titanium alloys intended to fit bone applications, Ti–Al–4V, Ti–Ni–Ta, Ti–Nb–7A–Zr, Ti–15MO–5Zr–3A, Ti–Sn–NB, and NiTi [25].

Titanium is called Ti6Al4V that has a minor alloy concentration of iron and oxygen as well as the most efficient aluminium-titanium alloys with 6% aluminium and 4% vanadium. The resistance to corrosion relies on oxide thickness and titanium nature. The Ni–Ti has been discovered to induce significant cell death. Moreover, titanium implants are more reliable than stainless steel and Cobalt–Chromium alloys for lifetime uses.

## 2.2 Materials for Coating

**Ceramics**. Ceramics are suited to replace different sections of the human body, notably bone and dental curves in the dentistry because of the intrinsic characteristics such as their high-compressive strength, when compared with metallic materials owing to the atomic bonds in higher environments. These bio-ceramic implantable ceramic materials are utilized for the repair and rebuilding of sick and damaged body parts. In terms of their interaction with the biological environment, they are classified as bio-inert, bio-reactive and bio-resorbable [26]. It has been discovered that bioinert ceramic materials offer better mechanical characteristics than other ceramics. Because of their ability to establish connections in physiological solutions, some ceramics are categorized as bioactive ceramics, such as glass and calcium phosphate. Because of their capacity to create a connection between the bone and surrounding tissues, these bioactive ceramics are mostly employed as coating materials in orthopaedic and dental implants. Bioceramics with low tensile strength and fracture toughness only suitable for heavy-duty applications [27]. These disadvantages can be addressed by utilizing them as coatings on metallic materials and for applications involving severe loads, such as joint replacements.

**Hydroxyapatite (HAp)**. Hydroxyapatite $[Ca_{10}(PO_4)6(OH)_2]$ is a calcium phosphate-based bio ceramic that forms the main inorganic component of human bones and teeth. HAp is preferred in biomedical applications due to its bioactive,

osteoconductive and biocompatibility propertiesis. Its weak mechanical characteristics, on the other hand, restrict its usage as a bone replacement in a variety of applications. As a result, it may be utilized as a coating material to improve and give an edge to the mechanical characteristics of stainless steel or titanium alloys, as well as a filler substance to repair damaged bone. By forming an apatite layer after implantation, this bioactive material readily acquires an apparent capacity to connect to the implant-tissue interface with excellent osteoconductive activity. HAp has been modified to produce dense, compact HAp and porous HAp for various biological purposes, as required. Adding the polymer to HAp increases its strength and strength to bone [28]. HAp may also be produced from waste materials such as egg and snail shells, and it has been demonstrated that the products are highly biocompatible with many cell lines of osteoblast and fibroblast.

**Zirconium dioxide (ZrO$_2$)**. Zirconia is a zirconium oxide that is biophysically polycrystalline. Zirconia, dependent on temperature and environment, occurs in three distinct stages, mono, cubic, and tetragonal. It is more difficult and powerful because of the different phases. It is considered to enable the zipper to be used in orthopaedic and dental application by its intrinsic features of particular toughness, strong wear resistance along with a low friction coefficient, and the chemical inertness along with increased elastic modulus. Zirconia implants are a superior alternative to titanium implants because they have higher mechanical strength, a better aesthetic look, and less plaque buildup on them [29].

**Titanium dioxide (TiO$_2$)**. Titanium dioxide has a good corrosion resistance and superior photocatalytic activity along with greater biocompatibility. These characteristics turn TiO$_2$ into an excellent biomaterial in several universal applications in pharmaceutical products, pigments and cosmetics and have been widely used as an integrating agent for tissues of the implant bone in the biomedical sector. These ideal characteristics are based on its physio-chemical qualities, including inertness, thermo-stability, and the ability to take different polymorphic forms like anatase, brookite, rutile, and with less oxygen of α-Ti$_3$O$_5$ [30].

**Silica (SiO$_2$)/Bioglass**. Silica is the silicon dioxide form employed in many applications because of its covalent bonding between the exceptional chemical stability of atoms. The investigative results in new tissue regeneration and medication delivery applications lead to the suit for silica-based biomaterial. In particular, Hench et al. [29] discovered the development of an apatite layer between them to establish strong, chemical bonding's with the bone structure. Since the beginning of bio-glass, several bioactive glasses and ceramics have been produced. These materials include A-W glass ceramic (where A is the apatite and W is the wollastonite), CaOSiO$_2$ glass free from P$_2$O$_5$, silicate, P$_2$O$_5$ and P$_2$O$_5$ glass [31]. Due to the ability to release numerous ions, hydroxyapatite nucleation by interaction with soft tissue and cellular membranes, proteins are also regarded a key role in the production of apatite in vivo and in vitro, to the generation of a hydrated silica gel at the surface. Silica is available in the form of silica spheres, bioglass, ceramic organic glass, silica gel, silica aerogel

and sol–gel metallic. It has been utilized to repair the bones damaged by certain bone disorders because of its direct bone-bonding capabilities.

**Zinc oxide (ZnO)**. The one of safe and high effective antibacterial agent is zinc oxide, which is mostly using in the food and agricultural industries. ZnO was used as an added material to enhance coating qualities of implantable materials like screws and plates with lower bacterial contamination, as well as its antibacterial function, low coefficients of thermal expansion and improved lubricity properties. Different goods, such as cotton textiles, diaper rash, anti-dandruff ointments and anti-dandruff shampoos, have their anti-bacterial characteristics and deodorizing capabilities [32].

## 2.3 Composite

A composite is a mixture of two or more component materials that give synergistic improvements and various physical and mechanical characteristics. In ways that it is an ideal candidate for diverse biomedical applications, composites, characteristics such as surface area, particle size and mechanical qualities are different from their original component materials. The natural hard tissue has somewhat greater mechanical characteristics than individual ceramic biomaterials. So, their mechanical characteristics are typically worse, limiting their applicability in high-bearing load applications. The development of various composite coating materials, including ceramic-ceramic or polymer-ceramic coatings, leads to greater mechanical and biological properties.

**Ceramic–Ceramic composites**. The composites made of Hydroxyapatite (HAp) with a bioactive glass covering have a higher mechanical resistance than HAp without affecting its bioactive characteristics. Different scientists have investigated the composites of bioglass-apatite Ti–6Al–4V coatings [33]. In instance, the Ti–6Al–4V composite of the HAp+$ZrO_2$+$Y_2O_3$ shows better mechanical characteristics with higher bioactivity. Bioceramic-free (porcelain wollastonite) composites have also been investigated and show better mechanical properties [33]. Composites are also investigated. Moreover, an in vivo animal studies have been shown to create good bone osteointegration in HAp and biologically inert alumina composites.

**Polymer-Ceramic composites**. In addition to other inorganic materials including metal oxides ($TiO_2$, $Al_2$, ZnO) and $SiO_2$, the creation of polymer (organic)-inorganic composites has been investigated. A uniformly deposited polyetheretherketone/ bioactive glass composite coating over NiTi was created for enhanced adhesion and with microstructural uniformity [34]. The inclusion of the polymeric substance PEEK resulted from a high strength of good tribological and chemical resistance.

## 2.4 Metallic Doping Ions

In recent years, materials science, in collaboration with biomedicine (medicine and biology), has aided in the development of biomaterials for the restoration or replacement of damaged tissue. Biocompatibility with certain mechanical, biological and physical qualities is necessary for biomaterials [35].

Due to characteristics such as biocompatibility, biodegradability, bioactivity and osteoconduction, various bioceramics and bioactive glasses (BGs) are the most often utilized materials among the several synthetic biomaterials explored for hard tissue regeneration and prosthesis covering [36]. Calcium phosphates [e.g., hydroxyapatite (HAp), α- and β-tricalcium phosphate (TCP)], calcium silicates [e.g., wollastonite ($CaSiO_3$) and larnite (β-$Ca_2SiO_4$)] and BGs which composition is mostly based on the $SiO_2$–$Na_2O$–$CaO$–$P_2O_5$ system (e.g., 45S5 and 58S), are some examples of biomaterials widely investigated for replacement and repair of hard tissue. These bone-bonding materials can form a chemically stable interface with the surrounding tissues by forming a bone-like apatite on the surface [37]. The development of apatite in vivo may be anticipated in vitro by exposing the material to a suitable aqueous solution whose chemical composition mimics physiological liquids [38].

The body has created new generations of bioceramics and BGs due to the bone regeneration capability and the imitation of biological tissue that led the organism to react as if it was in the presence of actual tissue. Materials capable of fixing the implant in the bone and recruiting cells to control its pace of disintegration became more important (Fig. 1). During in vivo dissolution, the control of the release of particular ions can achieve bone formation (Table 3). The high rate of solubility leads to a discrepancy in the bone tissue regeneration in the new bone growth in the ion release from the implantation locale [39]. In addition, inherent osteoinductivity and current sub-optimal kinetic development parameters in the ceramics for calcium phosphates are typically not present. In addition, the mechanical strength and fracture resistance of BGs are low, making implants problematic in load-bearing areas [40].

**Magnesium**. In the process of bone mineralization, osteoblast and osteoclast magnesium is an integral ingredient of the bone metabolism. In various matrices, mg ions ($Mg^{2+}$) were utilized as a dopant for increasing mechanical strength and reducing the rate of deterioration in the matrices [35]. $Mg^{2+}$ is commonly referred to as an alternative or calcium dopant in the structure of HAp, β-TCP and BGs.

**Silver**. Bioceramics and BGs are often resistant to antimicrobials and cause the development of microorganisms on their surfaces. Implant-related infections of microorganisms such as bacteria, viruses, or fungi are one of the leading reasons of implant failure. Bioceramics and BGs, specifically silver ions ($Ag^+$ and silver nanoparticles (AgNPs), have been doped for the improvement of antibacterial characteristics. $Ag^+$ or AgNPs are strongly connected in bacterial cell metabolism with thiol groups of enzymes that lead to cell death. Furthermore, $Ag^+$ and AgNPs are biocompatible, nontoxic at low concentrations, and have excellent thermal and physiological medium stability [36].

**Fig. 1** From 2015 to 2020, the frequency of various metal ions doped in bioactive glasses and bioceramics. Scopus data were used to compile this report
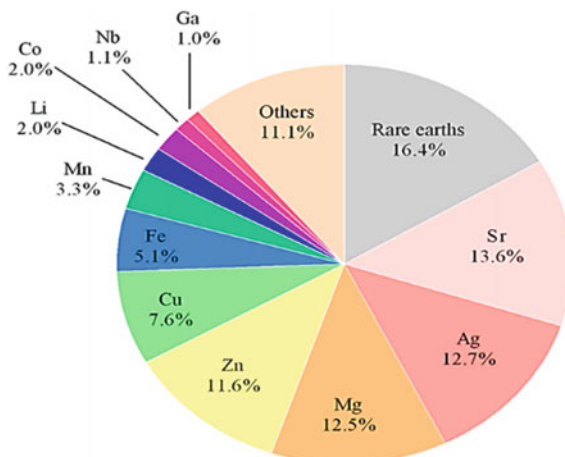


**Table 3** Metal ions' functions and biological effects in various matrices were discussed (all biological responses were observed in vitro, except when identified: in vivo)

| Ion | Ion concentration | Biological effects | References |
|---|---|---|---|
| $Mg^{2+}$ | 5 and 10 wt.% | Angiogenesis and osteogenesis were boosted (in vivo) | [35] |
| $Ag^+$ | 4.8 mol.% | Blood plasma protein adsorption and antibacterial activity | [36] |
| $Cu^{2+}$ | 0.6, 1.2, 1.8 and 2.4 (Cu/Ca molar ratio) | Antibacterial ability | [37] |
| $Sr^{2+}$ | 1:4 ($Sr^{2+}$: $Ca^{2+}$) | • Protein adhesion, cell survival and ALP activity have all improved<br>• New bone and bone veins are formed (in vitro and in vivo) | [38] |
| $Li^+$ | 1 wt.%<br>1.5 mol.% | • Antimicrobial properties<br>• In vitro and in vivo, it improves osteogenesis | [39] |
| $Fe^{2+}$/ $Fe^{3+}$ | 10–30% | • Antibacterial activity<br>• Superparamagnetic | [40] |
| $Zn^{2+}$ | 1 mol.% | • Antibacterial properties<br>• Proliferation of cells that have been stimulated | [41] |
| $Mn^{2+}$ | 1, 3 and 5 mol.% | • Proliferation of cells that have been stimulated<br>• Antibacterial properties | [42] |
| $Co^{2+}$ | – | • Improved osteogenesis<br>• Antibacterial activity | [43] |

**Copper**. Copper (Cu) is an essential trace element for both humans and animals. Copper ions ($Cu^{2+}$) play an important role in hard tissue engineering because they may improve angiogenesis and induce osteogenesis while also providing antimicrobial characteristics to bioceramics and BGs [37]. However, in order for copper particles to be successfully bio-applied, there must be a synergy between $Cu^{2+}$ and the matrix in which it is put. As a result, various matrices have been investigated to be doped with $Cu^{2+}$, the most important of which being HAp, BGs and calcium phosphate [37].

**Strontium**. The osteogenic, angiogenic and antibacterial characteristics of strontium ions ($Sr^{2+}$) have made them a popular dopant in biomaterials. Treatment for osteoporosis is improved when $Sr^{2+}$ is incorporated into the bones. $Sr^{2+}$, when included into BGs, may increase osteoblast activity while limiting osteoclast development, while also retaining the acellular bioactivity of glasses. Because of its physical and molecular similarities to calcium, strontium (Sr) is regarded as a natural bone-seeking element and is commonly utilized in bone replacement matrices such as BGs and HAp [38].

**Lithium**. The introduction of dopant ions in bioceramics matrix may provide a chance to improve certain of these biomaterials' qualities without sacrificing favourable characteristics. One of these ions, lithium ($Li^+$), has been utilized to improve bone regeneration therapies. Lithium is frequently used to treat mental illnesses including depression and mania [39]. As a side effect of lithium maintenance treatment, Zamani et al. (2009) reported an increase in bone mass in psychiatric patients [44]. Some studies have linked this behaviour to lithium's inhibition of glycogen synthase kinase 3 (GSK-3), which protects catenin from degradation and promotes osteogenesis. In osteoblasts, $Li^+$ can boost alkaline phosphatase and osteogenic gene expression. Furthermore, several studies have shown that Li has the ability to stimulate cartilage and subchondral bone regeneration [39]. Because of this, $Li^+$ has the potential to be used to dope biomaterials.

**Iron**. Magnetic nanoparticles have been increasingly used in biological applications. Due to their biocompatibility and superparamagnetic characteristics, iron-based phases like $Fe_3O_4$ and $Fe_2O_3$ are among the most often utilized magnetic nanoparticles in biomedical applications [40]. In addition, iron ions play an important role in the circulatory system. These ions are involved in the transfer of oxygen and nutrients, vessel development and tissue ingrowth [40].

**Zinc**. In matrices like BGs and HAp, zinc ion ($Zn^{2+}$) has been employed as a doping agent (thin films or composites). The addition of $Zn^{2+}$ to these matrices has antibacterial properties as well as promoting angiogenesis and homeostasis. In addition, $Zn^{2+}$ plays an important role in the formation, development and mineralization of bones by increasing the particular activity of ALP [41].

**Manganese**. Manganese (Mn) is a transition metal with more than five valence states, with $Mn^{2+}$ and $Mn^{3+}$ being the most common. Its oxidized chemical forms, such as $MnO_2$ or $Mn_3O_4$, are more frequent in the environment. Manganese has

a role in a variety of biological systems, including digestion, reproduction, nervous system development and skeletal construction. Manganese deficiency causes or raises the risk of osteoporosis [42]. Manganese ion is largely employed as a trace metal transition element in biomaterials, namely, in BGs, HAp and -TCP matrices. The release of active ions during breakdown is linked to biomaterial osteoinductivity. As a result, adding $Mn^{2+}$ ions to BGs, HAp and -TCP matrices is thought to aid bone regeneration by increasing osteoblast response, cell adhesion and osteogenic material production [42].

**Cobalt**. Cobalt (Co) is a trace element that is necessary for life, but only in small amounts since too much of it can induce toxicity and weaken the immune system. Cobalt ions ($Co^{2+}$) have been shown to imitate hypoxia and induce the production of several angiogenic factors. A 5wt. % replacement is usually advised for effective angiogenesis promotion and to avoid any harmful effects of $Co^{2+}$ inside the body [43].

## 2.5   Coating Techniques

Several coating methods have been used. For coating implants, mechanical techniques such as plasma spray, electrophoretic coating, biomimetic deposition, laser deposition and wet methods such as sol–gel-based spin coating, dip coating or electro deposition coating have been most commonly used [33, 45]. The overall benefits and limitations of several types of coating are mentioned in Table 4.

**Thermal spraying**. The method of thermal spray develops in several ways. New applications are probably the most intriguing breakthroughs in coating [34]. Examples include coating applied on new generating sources of energy such as electrolysis, photocatalysis self-cleansing of surfaces, electronic functions, biomaterials, etc.

**Magnetron sputtering**. In the process of wear-resistant coatings, corrosion-resistant coatings, low-friction coatings and ornamental layers, the magnetron sputtering has been employed [46].

**Ion beam deposition**. Deposition by ion beams is utilized to generate ultra-pure thin, epitaxial films at low temperatures, producing unusual, non-traditional film proprieties. In biomedical applications two types of wet chemical techniques are used: sol–gel and biomimetic. These procedures, which include moderate conditions for chemical preparation, produce a three-dimensional coating on the substratum not carried out using physical technology [47]. This biomimetic approach is a simple procedure by which a metal substratum is immersed into a simulated body fluid (SBF) solution to generate a surface coating.

**Pulsed laser deposition**. A physical phenomenon that uses Laser for flattening a target and condensing the target material on a substratum's face is a pulse-laser deposition technology (PLD) [48].

**Table 4** The advantages and limitations of different coating types

| Serial number | Type of coating | Thickness range | Advantages | Limitations |
|---|---|---|---|---|
| 1 | Thermal spraying | 30–200 $\mu$m | • High levels of deposition<br>• Costs are low | • Induces breakdown at high temperatures<br>• Fast cooling generates amorphous ceramic coatings |
| 2 | Magnetron sputtering | 0.5–3 $\mu$m | • The same thickness of the coating<br>• High adherence<br>• Full of dense pores<br>• Function to shield on thermal substrates | • More costly<br>• Low rates of deposition result in amorphous lacquers |
| 3 | Ion beam deposition | 0.05–1 $\mu$m | • Adhesive strength is high<br>• Coating thickness that is consistent | • More costly<br>• Make coatings of amorphous size |
| 4 | Pulsed laser deposition | 0.05–5 $\mu$m | • Coating having amorphous and crystalline phases<br>• The coating is dense and permeable | • More costly<br>• Simultaneous integration of biological agents avoids high temperature |
| 5 | Sol–gel technique | <1 $\mu$m | • Adhesive strength is high | • Inexpensive<br>• Processing temperatures are kept low<br>• Coatings that are too thin<br>• A regulated environment was required<br>• Precursors are expensive |
| 6 | Electrophoretic deposition (EPD) | 0.1 $\mu$m–2.0 mm | • Coating thickness that is consistent<br>• Deposition occurs quickly<br>• Coat a complicated substrate | • It is difficult to create crack-free coatings<br>• High sintering temperatures were required |

**Sol–gel technique**. On the other hand, the sol–gel technology provides a simple wet-chemical method to the biomaterial synthesis, which does not require a higher pH value or higher sintering temperatures [49, 45]. The sol–gel is a colloidal suspension in liquid solution of solid particles, i.e., 1–500 nm, or 'sol'. A sol is used in spraying, spin-coating and dip-coating for depositing layer on a substratum. The gel is calcinated or dried in the substrate to produce a thin surface layer. This approach uses the insertion of the metal sample in the calcium & phosphorus gel at a low temperature to create calcium phosphate layers. The coated layer is calcinated to 400–600 °C, depending on the material as its produced sheet is porous and less dense. In order to increase its attachment strength, a second layer of layer can be used to construct a multilayer material deposition over the implant [45].

**Electrophoretic deposition (EPD)**. The technology of EPD includes the transmission into the electrolytic solution of charged particles and has been thoroughly examined. The ceramic particles are charged in an aqueous or nonaqueous media from an electrical field. The deposition of thin films on a surface of an implantable material characterised by an inadequate protection of a surface layer, enhances wear and corrosion resistance of titanium implants [50]. The suspension in an EPD system comprises of homogeneously distributed powder particles, together with the corresponding anode and cathode electrodes, in an aqueous or non-aqueous media [45]. Depending on the particles, both cathodic and anodic deposition may be possible. Positively charged suspended particles are deposited in the cathodic cell, whereas negatively charged particles migrate to the anode.

The quality of the suspension is determined by suspension characteristics such as particle size, conductivity, dielectric constant and zeta potential, whereas physical parameters such as deposition time, voltages and substrate conductivity affect the success of the electrophoretic deposition (EPD). The lower surface loaded particles tend to attract one other, and the deposited coating was found to be pore [34, 45], while high surface charge particles create during deposition a strong electrostatic repulsive force, resulting in a dense layer. A consistent, properly conductive, medium-diet-constant particulate suspension, therefore, provides superior deposition.

## 3 Herbal Antibiotics for Dental and Orthopaedic Implant Applications

**Antibacterial qualities are found in certain natural components, but are they safe to use and when should they be used?**

Natural antibiotics have yet to be proven scientifically. Even though people have been using similar medicines for hundreds of years, most of them have not been thoroughly evaluated. However, certain medical evaluations have shown positive findings, and further research is being conducted [47]. With the increase of drug-resistant germs,

scientists are turning to nature for novel medication ideas. Here provided a brief overview of the research behind the 10 natural antibiotics.

## 3.1  Garlic

Many people all around the world have identified garlic as having therapeutic and therapeutic properties. Garlic has been demonstrated to be effective against a wide range of germs, including Salmonella and *E. coli*, in studies (*E. coli*). Garlic is also being studied as a treatment for multidrug-resistant TB.

**Extraction**: Garlic is a type of bulbous plant, that grows up to a height of 1.2 m, and in some cases, it may increase too. Garlic is a simple plant to cultivate, especially in moderate regions. Garlic comes in a variety of types or subspecies, consisting of a hard neck and soft garlic. The major bioactive component included in the aqueous extract of garlic or raw garlic homogeneity is allicin (allyl 2-propene-thiosulfinate or di-alyl thio-sulfinate) [48].

When the garlic is diced or crushed, the alliinase enzyme is stimulated, resulting in the production of allicin from allin (exhibit in garlic intact), 1-propylene allyl thio-sulfonate, allyl methyl thiosulfonate, (E, Z)-4,5,9-tritiododeca-L, 6,11-traine 9-oxide (azoin) and YL-glutamate-Alkyl-L-cysteine are all significant components in garlic homogenate. During many hours of incubation at room temperature, homogeneity raises the ratio as adenosine many times.

*Another mostly used garlic preparation process for garlic extract*: The sliced drawn garlic is stored in 15–20% of ethanol for more than 1.5 years, to reduce considerably Allicin, S-allyl cysteine, Sallylmercaptocysteine, Allixin, N-0-(Ideoxy-D-fructos-1-yl)-Larginine during this process, while selenium is a persistent and substantial antioxidant [49]. Garlic oil is usually manufactured by steam distillation and is used in medicine. Hexa sulphides from dialyl, allymethyl and dimethyl mono are found in steam-distilled garlic oil. Allium sativum, like onions, chives and metals, is a part of the lily family botanically.

## 3.2  Honey

Honey has been used as an ointment since Aristotle's time, helping to heal wounds and prevent or expel infection. Healthcare specialists now assist in the treatment of chronic wounds, burns, ulcers, bedsores and skin infections [51]. 2016 research, for example, found that honey dressing can help heal wounds.

Honey's antimicrobial qualities affect hydrogen peroxide levels in general. Despite its low hydrogen peroxide level, Manuka honey kills bacteria. According to 2011 research, the well-known variety of honey blocks a dependable source of

around 60 types of bacteria. It also suggests that honey helps cure wounds infected with methicillin-resistant Staphylococcus aureus (MRSA).

Apart from its antibacterial qualities, it aids wound healing by providing a protective layer that promotes a moist environment. Honey has been used to accelerate wound healing since ancient times, and its ability to heal wounds has been demonstrated. Honey is used to cure sores, bedsores and some other skin problems caused by burns and wounds. Honey has medicinal effects. It has antibacterial properties, helps to keep wounds moist, promotes healing and has a high viscosity, which aids in providing a protective barrier against infection. Honey has been reported to be useful in treating bruises, burns, skin ulcers and burns. Honey's antibacterial qualities speed up the creation of new tissue to cure wounds. In vivo action has been demonstrated for Medihoni and Manuka honey, making them appropriate for the treatment of burns, ulcers and infected wounds [52].

When treated directly to severe surgical incisions with infection, honey eliminates infection quickly. Honey enhances wound healing in infected wounds that are resistant to antibiotics and antiseptics, as well as methicillin-resistant S. aureus [53]. Honey can also be used on wounds and skin grafts.

## 3.3 Ginger

Ginger has been recognized as one of the natural antibiotics by the scientific community. Several studies have shown that ginger can combat a wide range of microorganisms. Researchers are looking at how ginger might help with nausea and motion sickness, as well as lowering blood sugar levels.

**The method of preparation consists of the following steps**:

A, preparation, cleaning, slicing of ginger, drying until the percentage of water is less than 5%, crushing to obtain ginger powder;

B, refluxing and extracting the ginger powder obtained in a step of 1–3 h using 60–70% ethanol, in which the extraction is performed 2–5 times, adding the extraction solutions to obtain the initial extraction solution;

C, Absorption of the primary extraction solution obtained in stage B using macroporous resin and removal of macroporous resin using 70–80% ethanol, 50–60% ethanol and 30–40% ethanol, respectively, mixed with eluting solutions, standing for 1–3 h, hard extraction solution filter;

D, concentrate the solid extraction solution obtained in step C; to make ginger extract, dilute 20–30% of the original amount, leave to stand for 1–2 h, filter and dry [48, 54].

## 3.4 Echinacea

For hundreds of years, Americans and other traditional healers have used Echinacea to cure wounds and infections. So, researchers are starting to figure out why?

The Echinacea purpurea extract Streptococcus pyogenes (S. pyogenes) is used to treat strep throat, blood poisoning and necrotizing fasciitis, sometimes known as meat feasting diseases. Echinacea can also help with inflammation caused by a bacterial infection. It may be purchased at health food stores or online.

This discovery is related to the method of extracting the active ingredients of echinacea by supercritical carbon dioxide. This method mainly consists of these processes: drying the whole echinacea; ultramicro crushing, supercritical carbon dioxide extraction, primary decomposition at reduced pressure, secondary decomposition at reduced pressure and echinacea extract alcohol. The characteristics of this method are: the extraction temperature is low, the velocity is high, the extraction rate is high, the solvent residues are avoided, the active ingredients obtained are high in content and have no undesirable effect on humans and the environment and the like.

## 3.5 Goldenseal

Goldenseal tea or pills are commonly used to treat respiratory and intestinal issues. It can, however, result in bacterial diarrhoea and urinary tract infections. Furthermore, the findings of a recent review indicate the benefits of Goldenseal in the treatment of skin problems caused by trustworthy sources. Goldenseal extract was utilized in one experiment to reduce MRSA tissue damage. Prescription medication users should consult their doctor before taking Goldenseal since this supplement might cause intervention. Berberine is also a key component of Golden Seal's natural antibiotics. This alkaloid is harmful to newborns, pregnant women and nursing mothers. Goldenseal pills can be found at health food stores or on the internet.

## 3.6 Clove

Clove has been utilized in dental operations for centuries. According to new research, clove water extract is a powerful and dependable source against several forms of bacteria, including E. coli. What is the process of extracting clove oil? Clove oil may be produced from the leaves, stems and buds of plants. Some industries sell clove oil, which is produced by distilling water and contains a low amount of eugenol.

### 3.7 Oregano

Oregano is thought to enhance the immune system and function as an antioxidant, according to several studies. It may have anti-inflammatory effects also.

### 3.8 Mint Leaves/Oil

Peppermint leaves have been found to have antiviral and antifungal activity. For both the Gram-positive and the Gram-negative bacteria, peppermint oil and menthol have mild antibacterial effects.

Fresh mint leaves can be found in natural plants or local stores. Fresh leaves are rinsed in distilled water that has been sterilized. To make the aqueous extract, 10 g of leaves was soaked in 100 ml of sterilized distilled water. After that, the extract was filtered twice with Whatman Filter Paper 1. This extract was filtered and dried, weighed and utilized for scientific purposes [48, 54].

### 3.9 Turmeric or Curcumin

Because bacterial resistance to most antibiotics is frequent, the function of natural bioactive compounds in the treatment of infections has been rediscovered. Curcumin is a bioactive compound derived from turmeric. Its potential as an antibacterial agent is now being investigated due to its antimicrobial capabilities.

It has been reported to have anti-inflammatory, antibacterial and anti-cancer properties, as well as promote the death of cells that are dangerous to the body or no longer needed.

The microwave-assisted extraction was performed in a microwave oven (LG Electronics Inc., Thailand) with a microwave frequency of 2450 MHz and a power of 180 W. In a 125 mL Erlenmeyer flask, the green solvents ethanol, PG, PEG 400 and glycerin (20 mL) were introduced individually. For 30 s, the extraction procedure was carried out under microwave radiation. The extract is subsequently filtered and the curcuminoid concentration is determined by HPLC. Three times the experiment was carried out. Further research was conducted using the solvent with the greatest concentration of curcuminoids.

### 3.10 Tulasi Leaves

It acts as a natural immune booster and keeps infections at bay. It has enormous antibacterial, antiviral and antifungal properties that can protect us from a variety of

infections. Basil leaf extract enhances the activity of T helper cells and natural killer cells, boosting [55] immunity.

The extraction was carried out in a cleavage apparatus, with the addition of 500 ml. It contains 30 g of crushed leaves of basil or basil and 300 ml of water added to the flask. The time collected was set at four o'clock. The extracted oil was dissolved in hexane and filtered after separation. It was then dried using $N_2SO_4$ to remove water, and the solutions were separated by a rotary evaporator.

## 4 Structural and Physicochemical Characterization of Biomaterials

There are numerous different sorts of review papers on biomaterial characterization, with many of them concentrating on a specific type of microscopy or material. A detailed list is already provided in the book. On the other hand, textbooks and handbooks on all of the methods listed below (Table 5) often do not address the special demands of biomaterial research, but rather outline the approaches with theoretical and/or practical background.

The Internet is the third source of information. Web pages of biological firms, in particular, can be utilized as access sites for further information, such as www.biomaterials.net, www.bmn.com, www.biomat.net, www.biomaterials.org, ssb.biomaterials.ch, www.dgbm-news.de, www.biomaterials.ca, www.esb-news.org, www.biomaterials.org.au, www.surfaces.org [52].

## 5 Discussions

Over the last two decades, great research has been conducted for the greater protection against bacterial colonization of suitable biomaterials, although the advanced study is only in progress [89]. In reality, despite the most recent successes in preclinical research, there is still a large gap between the proposed tactics and their clinical applicability. Because the majority of the coatings in the research are not suited for orthopaedic implants owing to cytotoxicity, genotoxicity, or immunoreactivity difficulties, their clinical applicability in vivo and in vitro may still be limited by biotechnology, economic, regulatory and medical difficulties [90].

Improved collaboration of governments, regulators, industry leaders and health workers will help people benefit. To transition from exploratory investigations to successful patient care, comprehensive classification and broad language are required to standardize suitable testing and real control needs [91].

There are numerous different sorts of review papers on biomaterial characterization, with many of them concentrating on a specific type of microscopy or material. The text already has a complete list. On the other hand, textbooks and handbooks

**Table 5** An overview of the numerous instrumental techniques used to characterize biomaterials and bone tissue structurally and physiochemically

| Serial number | Physicochemical properties | Characterization methods | Applications | References |
|---|---|---|---|---|
| 1 | Crystalline characteristics | Thermal methods | The impact of heat pressing on a material's properties, crystallization structure kinetics and weakening of a HAp/PLLA composite biomaterial (TGA) | [56] |
| | | XRD: X-ray diffraction | The quantitative and qualitative content, particle size and crystalline structure of biocomposite materials were investigated | [57–59] |
| 2 | Size of the particles | DLS: Dynamic light scattering | The data about particle flexibility as well as the nature of connections between nanoparticles and their surroundings | [60] |
| | | PDS: Particle size distribution | Influence of the particle size upon its kinetic parameters and ultimate micro and/or nano-structural properties of cathodic protection cement | [61] |
| | | SAXS: Small-angle X-ray scattering | The investigation on calcification of the bones | [62] |
| 3 | Chemical and structural analyses | Contact angle analysis | A solid surface's quality is determined using contact angle analysis. It is defined as the angle at which a liquid interacts with a solid surface | [63] |
| | | Zeta potential and surface charge | The zeta potential has the greatest impact on the solution stability of nanoparticle carriers | [64] |
| | | XPS: X-ray photoelectron spectroscopy | Polymeric biomaterials are analysed chemically | [65] |

(continued)

**Table 5** (continued)

| Serial number | Physicochemical properties | Characterization methods | Applications | References |
|---|---|---|---|---|
| | | EDX: Energy dispersive X-ray and Wavelength dispersive X-ray spectroscopy (WDX) | Semi-quantitative examination of irregularly shaped particles using WDX Characterization of composite biomaterials with EDX utilizing BCP and DLPLG | [66, 67] |
| | | Vibrational spectroscopy (Raman, FTIR) | CoHAp purity and cobalt's effect on the crystal structure (Raman spectroscopy) After glucocorticoid therapy, the bone tissue of animal experiments was characterized (FTIR) The use of HAp/PLLA composites as a bone replacement is being investigated (FTIR) | [68–70] |
| | | NMR: Nuclear magnetic resonance | 1H and 13C NMR were used to determine the component structure of the PLGA/HAp core–shell nanostructures The 1H and 31P solid-state NMR characterization of bioceramics, calcium phosphate, rabbit bone and human pathologic bone samples | [71, 72] |

(continued)

**Table 5** (continued)

| Serial number | Physicochemical properties | Characterization methods | Applications | References |
|---|---|---|---|---|
| | | Solid-state nuclear magnetic resonance (ssNMR) | Polymers, biopolymers, bioinorganic systems, biomaterials, proteins, paramagnetic substances and innovative self-assembled structures are all examples of applications. Recent advancements in technology and applications for characterizing inorganic materials | [73, 74] |
| | | ESR: Electron spin resonance | Measurement of $TiO_2$-generated oxidants during adhesion of dental implants | [75, 76] |
| | | AAS: Atomic absorption spectrometry | Biomimetic HAp elemental analysis | [77] |
| | | Inductively coupled plasma-atomic emission spectrometry (ICP-AES) | Trace element determination in tooth enamel Clindamycin is released from PLGA/HAp-based drug delivery systems | [78] |
| 4 | Physiology | SEM: Scanning electron microscopy | Hot-pressed HAp/PLLA biocomposite blocks: microstructure and mechanical qualities Advanced nanocomposite materials for orthopaedic purposes are being evaluated | [79] |
| | | TEM: Transmission electron microscopy | The study of nanosized plate-like HAp | [80] |

(continued)

**Table 5** (continued)

| Serial number | Physicochemical properties | Characterization methods | Applications | References |
|---|---|---|---|---|
| | | HRTEM: High-resolution transmission electron microscopy | Investigation of biological crystal formation processes near implanted synthetic HAp crystals The effect of zinc and alginate ions on the shape and growth process of HAp crystals | [81–83] |
| | | SPM: Scanning probe microscopy | STM analysis of the biomaterial-biological tissue interface AFM analysis of CP granules/particles covered with PLGA | [84, 85] |
| | | SAED: Selected area electron diffraction | The effect of ultrasound on the HAp's growth mechanism | [86] |
| | | EELS: Electron energy-loss spectroscopy | The structural environment of Ca atoms in nano-sized calcium-deficient apatite was investigated. The nanostructure of mineralized ivory dentine has been studied | [87, 88] |

on all of the aforementioned approaches often do not include the special demands of biomaterial research, but rather explain the approaches with their theoretical and/or practical backgrounds.

## 6   Conclusion

This review demonstrated the classification of various antibacterial coating methods. The metallic materials and methods for coating techniques are clearly reviewed and explained. The corrosion is also a key element of implant failure, which cannot be disregarded since it can induce toxicities and undesirable consequences, including tissue destruction. Even though the ceramic-coated metal composites have a promising potential for biomedical applications, their thickening, corrosion, degradation and waste emissions are known limits. Research efforts should be aimed towards further improvement and long-term, sustainable coatings control of their

physiochemical characteristics. Moreover, composite coatings on the implants can be adapted to the host's demands since they give a chance for composition and properties workability. Only target tissues and factors for the different tissue regeneration procedures should be used for the selections of coatings and relevant methods. The natural antibacterial agents are also presented here and given a brief discussion about their extraction processes also.

Biomaterial characterization is the main challenging task to select the suitable test. Here, we provided a complete characterization classification based on their physicochemical characteristics. So, based on your applications you may select the characterization method as listed above.

**Declarations**

**Ethical Approval and Consent to Participate**   Not applicable.

**Consent for Publication**   Not applicable.

**Competing Interests**   The authors declare that they have no competing interests.

**Funding**   Not applicable.

**Availability of Data and Materials**   All data generated or analysed during this study are included in this published article. All figures used in the manuscript are collected from the source of google scholar, images for readers' better understanding with proper permissions.

**Authors Contributions**   Konduru Ashok Kumar Raju has performed the histological examination and contributed the Sect. 2: Metallic Materials and Techniques for Coating, Sect. 3: Herbal Antibiotics for Dental and Orthopaedic implant applications, Sect. 4: Structural and Physicochemical Characterization of Biomaterials and was a major contributor in writing the manuscript. Amit Biswas has performed the histological examination and contributed the Sect. 1: Classification of Antibacterial Coating Technologies. All authors read and approved the final manuscript.

**Publisher's Note**   Publisher remains neutral concerning jurisdictional claims in published maps and institutional affiliations.

# Abbreviations

| | |
|---|---|
| SSI | Surgical site infections |
| MRSA | Methicillin-resistant Staphylococcus aureus |
| S. aureus | Staphylococcus aureus |

| HPLC | High-Performance Liquid Chromatography |
| S. pyogenes | Streptococcus pyogenes |
| E. coli | Escherichia coli |

# References

1. Schatkoski VM et al (Feb 2021) Current advances concerning the most cited metal ions doped bioceramics and silicate-based bioactive glasses for bone tissue engineering. J Ceram Int, 2999–3012. https://doi.org/10.1016/j.ceramint.2020.09.213
2. Dale H, Hallan G, Hallan G, Espehaug B, Havelin LI, Engesaeter LB (2009) Increasing risk of revision due to deep infection after hip arthroplasty. Acta Orthop 80:639–645
3. Aggarwal VK, Bakhshi H, Ecker NU, Parvizi J, Gehrke T, Kendoff D (2014) Organism profile in periprosthetic joint infection: Pathogens differ at two arthroplasty infection referral centres in Europe and in the United States. J Knee Surg, 10. https://doi.org/10.1055/s-0033-1364102
4. Romano CL, Scarponi S et al (2015) Antibacterial coating of implants in orthopaedics and trauma: a classification proposal in an evolving panorama. J Orthop Surg Res 10:157. https://doi.org/10.1186/s13018-015-0294-5
5. Zmistowski B, Karam JA, Durinka JB, Casper DS, Parvizi J (2013) Periprosthetic joint infection increases the risk of one-year mortality. J Bone Joint Surg Am 95:2177–2184
6. Kurtz SM, Lau E, Watson H, Schmier JK, Parvizi J (2012) Economic burden of periprosthetic joint infection in the United States. J Arthroplast 27:61–65
7. An YH, Friedman RJ (1996) Prevention of sepsis in total joint arthroplasty. J Hosp Infect 33:93–108
8. Barton AJ, Sagers RD, Pitt WG (1996) Bacterial adhesion to orthopedic implant polymers. J Biomed Mater Res 30:403–410
9. Beiko DT, Knudsen BE, Watterson JD, Denstedt JD (2003) Biomaterials in urology. Curr Urol Rep 4:51–55
10. Bergamini TM, McCurry TM, Bernard JD, Hoeg KL, Corpus RA, James BE, Peyton JC, Brittian KR, Cheadle WG (1996) Antibiotic efficacy against Staphylococcus epidermidis adherent to vascular grafts. J Surg Res 60:3–6
11. Bunt TJ (1983) Synthetic vascular graft infections. I. Graft infections. Surgery 93:733–746
12. Camiade C, Goldschmidt P, Koskas F, Ricco JB, Jarraya M, Gerota J, Kieffer E (2001) Optimization of the resistance of arterial allografts to infection: comparative study with synthetic prostheses. Ann Vasc Surg 15:186–196
13. Humphreys H (2012) Surgical site infection, ultraclean ventilated operating theatres and prosthetic joint surgery: where now? J Hosp Infect 81:71–72
14. Costerton JW, Montanaro L, Arciola CR (2005) Biofilm in implant infections: its production and regulation. Int J Artif Organs 28:1062–1068
15. Darouiche RO (2001) Device-associated infections: a macroproblem that starts with microadherence. Clin Infect Dis 33:1567–1572
16. Darouiche RO (2004) Treatment of infections associated with surgical implants. N Engl J Med 350:1422–1429
17. Deutschle T, Porkert U, Reiter R, Keck T, Riechelmann H (2006) In vitro genotoxicity and cytotoxicity of benzalkonium chloride. Toxicol in vitro 20:1472–1477
18. Dunne WM Jr, Mason EO Jr, Kaplan SL (1993) Diffusion of rifampin and vancomycin through a Staphylococcus epidermidis biofilm. Antimicrob Agents Chemother 37:2522–2526
19. Elek SD, Conen PE (1957) The virulence of Staphylococcus pyogenes for man; a study of the problems of wound infection. Br J Exp Pathol 38:573–586
20. Filloux A, Vallet I (2003) Biofilm: set-up and organization of a bacterial community. Med Sci (Paris) 19:77–83 (In French)

21. Sivakumar M, Rajeswari S, Thulasiraman V (1996) Metallographic investigation of a failed stainless steel orthopaedic implant device. J Mater Sci Lett 15:2192
22. Niinomi M (1998) Mechanical properties of biomedical titanium alloys. Mat Sci Eng A 243:231–236
23. Bruni S, Martinesi M, Stio M et al (2005) Effects of surface treatment of Ti–6Al–4V titanium alloy on biocompatibility in cultured human umbilical vein endothelial cells. Acta Biomater 1:223–234
24. Qiu Y, Thomas S, Gibson MA et al (2017) Corrosion of high entropy alloys. Npj Mater Degrad 1:1–15
25. Besra L, Liu M (2007) A review on fundamentals and applications of electrophoretic deposition (EPD). Prog Mater Sci 52:1–61
26. Ramli RA, Adnan R, Bakar MA et al (2011) Synthesis and characterization of pure nanoporous hydroxyapatite. J Phys Sci 22:25–37
27. Ozkurt Z, Kazazoglu E (2011) Zirconia dental implants: a literature review. J Oral Implantol 37:367–376
28. Zhang XQ, Yin LH, Tang T et al (2011) ZnO, $TiO_2$, $SiO_2$, and $Al_2O_3$ nanoparticles-induced toxic effects on human fetal lung fibroblasts. Biomed Environ Sci 24:661–669
29. Hench LL, Splinter RJ, Allen W et al (1971) Bonding mechanisms at the interface of ceramic prosthetic materials. J Biomed Mater Res 5:117–141
30. Kolodziejczak-Radzimska A, Jesionowski T (2014) Zinc oxide-from synthesis to application: a review. Materials (Basel) 7:2833–2881
31. Zhao Y, Zhang Z, Dai Q et al (2016) Microstructure and bond strength of HAP (+$ZrO_2$+$Y_2O_3$)/Ti–6Al–4V composite coatings fabricated by RF magnetron sputtering. Surf Coat Technol 200:5354–5363
32. Boccaccini A, Peters C, Roether J et al (2006) Electrophoretic deposition of polyetheretherketone (PEEK) and PEEK/Bioglass coatings on NiTi shape memory alloy wires. J Mater Sci 41:8152–8159
33. Callister WD (2000) Materials science and technology: an introduction, 5th edn. Wiley, New York, NY
34. Gibson I, Bonfield W (2002) Preparation and characterization of magnesium/carbonate co-substituted hydroxyapatites. J Mater Sci Mater Med 13:685–693
35. Du Z, Leng H, Guo L, Huang Y, Zheng T, Zhao Z, Liu X, Zhang X, Cai Q, Yang X (2020) Calcium silicate scaffolds promoting bone regeneration via the doping of Mg2+ or Mn2+ ion, Compos. B Eng 190:107937. https://doi.org/10.1016/j.compositesb.2020.107937
36. Chen K, Ustriyana P, Moore F, Sahai N (2019) Biological response of and blood plasma protein adsorption on silver-doped hydroxyapatite. ACS Biomater Sci Eng 5:561–571. https://doi.org/10.1021/acsbiomaterials.8b00996
37. Hui P, Dong Z, Wenkun P, Yao D, Huichang G, Tongxiang L (2020) Facile synthesis of copper doping hierarchical hollow porous hydroxyapatite beads by rapid gelling strategy. Mater Sci Eng C 109:110531. https://doi.org/10.1016/j.msec.2019.110531
38. Ge M, Ge K, Gao F, Yan W, Liu H, Xue L, Jin Y, Zhang J (2018) Biomimetic mineralized strontium-doped hydroxyapatite on porous poly (l-lactic acid) scaffolds for bone defect repair. Int J Nanomed 13:1707–1721
39. Yuan Y, Yuan Q, Wu C, Ding Z, Wang X, Li G, Gu Z, Li L, Xie H (2019) Enhanced osteo-conductivity and osseointegration in calcium polyphosphate bioceramic scaffold via lithium doping for bone regeneration. ACS Biomater Sci Eng 5:5872–5880. https://doi.org/10.1021/acsbiomaterials.9b00950
40. Morsi MA, Hezma AEM (2019) Effect of iron doped hydroxyapatite nanoparticles on the structural, morphological, mechanical and magnetic properties of polylactic acid polymer. J Mater Res Technol 8:2098–2106. https://doi.org/10.1016/j.jmrt.2019.01.017
41. Predoi D, Iconaru S, Predoi M, Buton N, Motelica-Heino M (2019) Zinc doped hydroxyapatite thin films prepared by sol–gel spin coating procedure. Coatings 9:156. https://doi.org/10.3390/coatings9030156

42. Panneerselvam R, Anandhan N, Gopu G, Ganesan KP, Marimuthu T (2020) Impact of different transition metal ions in the structural, mechanical, optical, chemico-physical and biological properties of nanohydroxyapatite. Appl Surf Sci 506:144802. https://doi.org/10.1016/j.apsusc.2019.144802

43. Lin WC, Yao C, Huang TY, Cheng SJ, Tang CM (2019) Long-term in vitro degradation behavior and biocompatibility of polycaprolactone/cobalt substituted hydroxyapatite composite for bone tissue engineering. Dent Mater 35:751–762. https://doi.org/10.1016/j.dental.2019.02.023

44. Zamani A, Omrani GR, Nasab MM (2009) Lithium's effect on bone mineral density. Bone 44(2):331–334. https://doi.org/10.1016/j.bone.2008.10.001

45. Priyadarshini B, Rama M, Chetan, Vijayalakshmi U (2019) Bioactive coating as a surface modification technique for biocompatible metallic implants: a review. J Asian Ceram Soc 7(4):397–406. https://doi.org/10.1080/21870764.2019.1669861

46. Instrumental methods and techniques for structural and physicochemical characterization of biomaterials and bone tissue: a review; Zarko Mitic., Faculty of Medicine, & Faculty of Mechanical Engineering RS-18000 Nis, Serbia; Article history: Received 27 March 2017 Received in revised form 16 May 2017 Accepted 17 May 2017 Available online 18 May 2017

47. Gristina AG (1994) Implant failure and the immuno-incompetent fibroinflammatory zone. Clin Orthop Relat Res 1994:106–118

48. Danielle Dresden and reviewed by the Debra Rose Wilson, PhD, on January 1, 2020. A newsletter in Medical News Today articles, best natural antibiotics; https://bit.ly/3iLvXMC

49. Harvey RA, Greco RS (1981) The noncovalent bonding of antibiotics to a polytetrafluoroethylene-benzalkonium graft. Ann Surg 194:642–647

50. Raju KAK, Biswas A (2023) Corrosion behavior of self-organized $TiO_2$ nanotubular arrays grown on $Ti_6Al_4V$ for biomedical applications. Mater Chem Phy 305:128011. https://doi.org/10.1016/j.matchemphys.2023.128011

51. Harvey RA, Tesoriero JV, Greco RS (1984) Noncovalent bonding of penicillin and cefazolin to dacron. Am J Surg 147:205–209

52. Instrumental methods and techniques for structural and physicochemical characterization of biomaterials and bone tissue: a review; Zarko Mitic, Faculty of Medicine, & Faculty of Mechanical Engineering RS-18000 Nis, Serbia; Article history: Received 27 March 2017 Received in revised form 16 May 2017 Accepted 17 May 2017 Available online 18 May 2017

53. Ashok Kumar Raju K et al (Nov 2015–Jan 2016) Analysis of femur bone during static condition by using Finite element Method; i-Manager's. J Futur Eng Technol 11(2)

54. Ashok Kumar Raju K et al (Mar 2015) Modeling and analysis of human liver by using finite element analysis. Int J Sci Res (IJSR) 4(3). ISSN (Online): 2319-7064

55. Mallikarjun S et al (Mar–Apr 2016) Antimicrobial efficacy of Tulsi leaf (Ocimum sanctum) extract on periodontal pathogens: an in vitro study. J Indian Soc Periodontol 20(2):145–150. PMID: 27143825; https://doi.org/10.4103/0972-124X.175177

56. Ignjatović N, Suljovrujić E, Stojanović Z, Uskoković D (2002) Structure and characteristics of the hot pressed hydroxyapatite/poly-L-lactide composite. Sci Sinter 34:79–93

57. Affatato S, Bracco P, Costa L, Villa T, Quaglini V, Ton A (2012) In vitro wear performance of standard, crosslinked, and vitamin-E-blended UHMWPE. J Biomed Mater Res A 100:554–560

58. Kandić L, Mitrić M, Ignjatović N, Uskoković DP (2006) XRD analysis of calcium phosphate and biocomposite calcium phosphate/bioresorbable polymer. Mater Sci Forum 518:507–512

59. Veselinović L, Karanović L, Stojanović Z, Bračko I, Marković S, Ignjatović N, Uskoković D (2010) Crystal structure of cobalt–substituted calcium hydroxyapatite nanopowders prepared by hydrothermal processing. J Appl Crystallogr 43:320–327

60. Smeets R, Kolk A, Gerressen M, Driemel O, Maciejewski O, HermannsSachweh B, Riediger D, Stein JM (2009) A new biphasic osteoinductive calcium composite material with a negative Zeta potential for bone augmentation. Head Face Med 5:13

61. Ginebra MP, Driessens FCM, Planell JA (2004) Effect of the particle size on the micro and nanostructural features of a calcium phosphate cement: a kinetic analysis. Biomaterials 25:3453–3462

62. Fratzl P, Schreiber S, Klaushofer K (1996) Bone mineralization as studied by small-angle x-ray scattering. Connect Tissue Res 34:247–254
63. Ignjatović N, Uskoković V, Ajduković Z, Uskoković D (2013) Multifunctional hydroxyapatite and poly(D, L-lactide-co-glycolide) nanoparticles for the local delivery of cholecalciferol. Mater Sci Eng C 33:943–950
64. Menzies KL, Jones L (2010) The impact of contact angle on the biocompatibility of biomaterials. Optom Vis Sci 87(6):387–399
65. Sabbatini L, Zambonin PG (1996) XPS and SIMS surface chemical analysis of some important classes of polymeric biomaterials. J Electron Spectrosc 81:285–301
66. Weinbruch S, Wentzel M, Kluckner M, Hoffman P, Ortner HM (1997) Characterization of individual atmospheric particles by element mapping in electron probe microanalysis. Mikrochim Acta 125:137–141
67. Ajduković Z, Ignjatović N, Petrović D, Uskoković D (2007) Substitution of osteoporotic alveolar bone by biphasic calcium phosphate/poly-DL-lactide-co-glycolide biomaterials. J Biomater Appl 21:317–328
68. Stojanović Z, Veselinović L, Marković S, Ignjatović N, Uskoković D (2009) Hydrothermal synthesis of nanosized pure and cobalt-exchanged hydroxyapatite. Mater Manuf Process 24:1096–1103
69. Mitić Ž, Najman S, Cakić M, Ajduković Z, Ignjatović N, Nikolić R, Nikolić G, Stojanović S, Vukelić M, Trajanović M (2014) Spectroscopic characterization of bone tissue of experimental animals after glucocorticoid treatment and recovery period. J Mol Struct 1074:315–320
70. Ignjatović N, Savić V, Najman S, Plavšić M, Uskoković D (2001) A study of HAp/PLLA composite as a substitute for bone powder, using FTIR spectroscopy. Biomaterials 22:571–575
71. Vukomanović M, Škapin SD, Poljanšek I, Žagar E, Kralj B, Ignjatović N, Uskoković D (2011) Poly(D,L-lactide-co-glycolide)/hydroxyapatite core-shell nanosphere. Part 2: simultaneous release of a drug and a prodrug clindamycin and clindamycin phosphate. Colloid Surf B 82:414–421
72. Miquel JL, Facchini L, Legrand AP (1990) Characterisation and conversion study into natural living bone of calcium phosphate bioceramics by solid state NMR spectroscopy. Clin Mater 5:115–125
73. Brown SP (2012) Applications of high-resolution 1 H solid-state NMR. Solid State Nucl Magn Reson 41:1–27
74. Hanna JV, Smith ME (2010) Recent technique developments and applications of solid state NMR in characterising inorganic materials. Solid State Nucl Magn Reson 38:1–18
75. Oliveira LC, Kinoshita A, Barreto AMF, Figueiredo AM, Silva JLL, Baffa O (2010) ESR dating of teeth from Brazilian megafauna. In: International conference on defects in insulating materials. Journal of physics: conference series, p 249
76. Lee MC, Yoshino F, Shoji H, Takahashi S, Todoki K, Shimada S, Kuse-Barouch K (2005) Characterization by electron spin resonance spectroscopy of reactive oxygen species generated by titanium dioxide and hydrogen peroxide. J Dent Res 84:178–182
77. Thamaraiselvi TV, Prabakaran K, Rajeswari S (2006) Synthesis of hydroxyapatite that mimic bone minerology. Trends Biomater Artif Organs 19:81–83
78. Ghadimi E, Eimar H, Marelli B, Nazhat SN, Asgharian M, Vali H, Tamimi F (2013) Trace elements can influence the physical properties of tooth enamel. Springer Plus 2(499):1–12
79. Ignjatović N, Delijić K, Vukčević M, Uskoković D (2001) Microstructure and mechanical properties of hot-pressed hidroxyapatite/poly-L-lactide biomaterials. Key Eng Mater 192–195:737–740
80. Chevaliera J, Taddeib P, Gremillarda L, Devillea S, Fantozzia G, Bartoloméc JF, Pecharromanc C, Moyac JS, Diazd LA, Torrecillasd R, Affatato S (2011) Reliability assessment in advanced nanocomposite materials for orthopedic applications. J Mech Behav Biomed Mater 4:303–314
81. Vukomanović M, Mitrić M, Škapin SD, Žagar E, Plavec J, Ignjatović N, Uskoković D (2010) Influence of ultrasonic processing on the macromolecular properties of poly (D, L-lactide-co-glycolide) alone and in its biocomposite with hydroxyapatite. Ultrason Sonochem 17:902–908

82. Hemmerlé J, Cuisinier FJG, Schultz P, Voegel JC (1997) HRTEM study of biological crystal growth mechanisms in the vicinity of implanted synthetic hydroxyapatite crystals. J Dent Res 76(2):682–687

83. Jun M, Jinli Q (2015) Graphene-like zinc substituted hydroxyapatite. Cryst Growth Des 15(3):1273–1279

84. Emch R, Clivaz X, Taylor-Denes C, Vaudaux P, Descouts P (1990) Scanning tunneling microscopy for studying the biomaterial-biological tissue interface. J Vac Sci Technol A 8:655–658

85. Ignjatović N, Ninkov P, Sabetrasekh R, Uskoković D (2010) A novel nano drug delivery system based on tigecycline-loaded calcium-phosphate coated with poly-DLlactide-co-glycolide. J Mater Sci Mater Med 21:231–239

86. Ignjatović N, Delijić K, Vukčević M, Uskoković D (2001) The designing of properties of hydroxyapatite/poly-L-lactide composite biomaterials by hot pressing. Z Metallkd 92:145–149

87. Sz-Chian L, San-Yuan C, Hsin-Yi L, Jong-Shing B (2004) Structural characterization of nanosized calcium deficient apatite powders. Biomaterials 25:189–196

88. Jantou-Morris V, Horton MA, McComb DW (2010) The nano-morphological relationships between apatite crystals and collagen fibrils in ivory dentine. Biomaterials 31:5275–5286

89. Gollwitzer H, Ibrahim K, Meyer H, Mittelmeier W, Busch R, Stemberger A (2003) Antibacterial poly (D, L-lactic acid) coating of medical implants using a biodegradable drug delivery technology. J Antimicrob Chemother 51:585–591

90. Gotz F (2002) Staphylococcus and biofilms. Mol Microbiol 43:1367–1378

91. Greco RS, Harvey RA, Smilow PC, Tesoriero JV (1982) Prevention of vascular prosthetic infection by a benzalkonium-oxacillin bonded polytetrafluoroethylene graft. Surg Gynecol Obstet 155:28–32

**Konduru Ashok Kumar Raju** Ph.D. research scholar currently working on Biomaterials and Tissue Engineering at the National Institute of Technology, Rourkela, Odisha. I hold a B.E, M.E in Mechanical Engineering and published 10 international journal papers [kingashok143@gmail.com].

**Dr. Amit Biswas** is an Assistant Professor of the National Institute of Technology, Rourkela in the Department of Biotechnology and Medical Engineering. He has produced and co-written several peer-reviewed scientific articles and has presented his work at several national and international conferences. His efforts have received appreciation from eminent topic specialists all across the world. He is an active member of several organizations and academies. Several prestigious prizes and funding have been bestowed upon him over his academic career [amitb79@gmail.com].

# Evaluation of Tensile Strength for 3D-Printed PLA Specimens

**Harsh Chokshi, Kautilya Patel, Dhaval Shah** ⦿**, and Kaushik Patel**⦿

**Abstract** Additive manufacturing (AM) technology plays a vital role in manufacturing components for the validation of designs. However, the strength of end-user functional components using fused deposition modeling (FDM) is yet a space of flow research. Polylactic acid (PLA) is a bio-degradable material regularly utilized in the FDM-based 3D printing process. This research paper focuses on process parameters such as layer thickness, infill geometry, and the number of perimeter on tensile strength of PLA samples. The finite element (FE) simulation has been performed on 3D printed parts to predict von-Mises stress and tensile strength. The simulation process involves the preparation of parts in SolidWorks and then subjected to tensile loads in ANSYS to calculate desired results. Three different simulation approaches have been employed and compared to obtain accurate results. The simulated results have also been compared with experimental tensile strength value for 3D printed parts fabricated using PLA material in Pursa MK3S FDM printer, exposed to tensile testing in the universal testing machine. The results revealed that the percentage variation of tensile strength for simulation and experimental results has been found in the range of almost 20%. The work proposed to simulate their behavior under tensile loads for future examination on the coupled effects of processing parameters.

**Keywords** 3D printing · Finite element analysis · Fused deposition modeling · Polylactic acid · Tensile strength

## 1 Introduction

In the present society, industries are anticipating costing reserve funds, further developed item life, a better caliber, and greater quality of the items. The developing interest in customized items in various fields like aviation, an automobile with complicated geometry, and various elements has prompted an ascent in the use of additive

H. Chokshi · K. Patel · D. Shah (✉) · K. Patel
Mechanical Engineering Department, Institute of Technology, Nirma University, S-G Highway, Ahmedabad 382481, India
e-mail: dbshah@nirmauni.ac.in

manufacturing (AM) innovation. Among a few AM technologies accessible in the current situation, fused deposition modeling (FDM) has been picked as the space of center as a result of its uncommon qualities, for example, the capacity to assemble complex constructions in a layer-by-layer technique beginning from a computer-aided design (CAD) document and ability to utilize various types of materials in the creation. AM could limit the creation cost and work on the productivity of the general assembling area. However, the strength of the part made is lower than the conventional technique [1].

Mazzanti et al. [2] reviewed that the different process parameters during the FDM process affect mechanical properties like tensile, flexural, compressive, and impact strength of various thermoplastic polymers filled with natural fibers. Torres et al. [3] considered temperature, perimeter, speed, infill density, layer thickness, infill direction for study of the effect of these parameters on ultimate tensile strength. Abeykoon et al. [4] studied the tensile strength, bending strength, and compression strength of PLA and ABS material with reinforcement of carbon fiber and carbon nanotube. The infill density, infill pattern, infill speed, and nozzle temperature were considered as process parameters to study the effect on the Young's modulus and flexural modulus of 3D printed specimens. Dey and Yodo [5] measured surface roughness, dimensional accuracy, build time, compressive strength, and tensile strength based on the input parameters. Xinhua et al. [6] observed the effect of layer thickness, filling speed, nozzle temperature, filling style, and raster width on the distortion of the thin plate of PLA. Kumar and Narayan [7] performed static structural analysis using ANSYS to measure tensile strength for the plastic material. Cattenone et al. [8] investigated the impact of mesh size, material model, and time step on mechanical properties by performing macroscopic simulations of the FDM process using ABAUS, and also results of simulations were validated with experimental. Alafaghani et al. [9] established a new FEA approach that utilizes apparent density of FDM parts to consider gaps and porosity present in the parts due to infill pattern. Farbman and McCoy [10] carried out FE analysis to study the effect of infill geometry on the strength to weight ratio using ANSYS. Lanzotti et al. [11] studied the effect of layer thickness, infill orientation, and a number of shell perimeters on tensile properties of specimens.

The vast majority of the examinations focused on one parameter or one material property at a time. Yet, in the genuine FDM manufacturing process, a few parameters become an integral factor during creation along with mechanical properties. Thus, it is important to consider the synchronous or interaction effect of crucial process parameters during the FDM process. In the present work, FEA analysis of 3D printed components has been performed by considering layer thickness, infill geometry, and the number of perimeter as process parameters to obtain tensile properties.
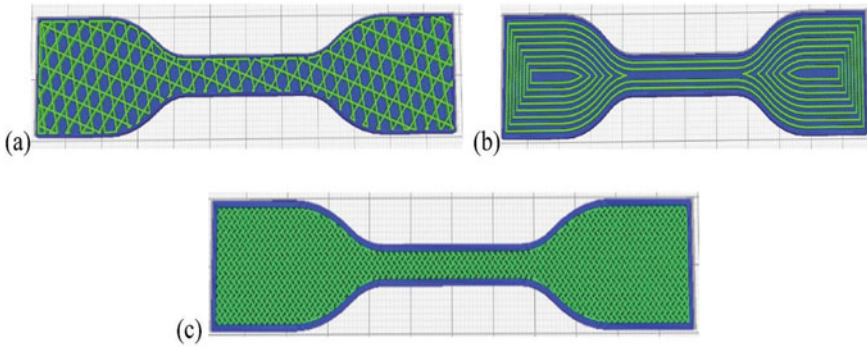
**Fig. 1** Different infill geometry, **a** tri-hexagonal, **b** concentric, **c** gyroid [5]

## 2 Materials and Methods

The PLA plastic material has been used in the 3D printing FDM process in the present study because of its printability, biodegradability and also derived from biomaterials. The material properties for PLA are as: melting temperature of 130–230 °C, shear modulus of 1287 MPa, elastic modulus of 3500 MPa, yield strength of 70 MPa, ultimate tensile strength of 73 MPa, flexural strength of 106 MPa, and Poisson's ratio of 0.36.

The layer thickness (height), infill geometry, and the number of perimeters have been considered for the present work. Three different layer heights of 0.06, 0.1, 0.15 mm, three number of perimeters of 2, 4, 6, and three different infill geometry is of tri-hexagonal, concentric, gyroid (Fig. 1) have been taken as process parameters. The printing time, required raw material in wire form, amount of void content, and strength depend on infill geometry. The selection of infill geometry during printing can be done based on the specification of selected 3D printer. In the present manuscript, three different infill geometry, namely, tri-hexagonal, concentric, gyroid have been considered. Some of the parameters have been kept constant like: 10 top and bottom layers, printing temperature 200 °C, build plate temperature 60 °C, print speed 60 mm/s, infill density 75%, and cooling 100%.

## 3 Implementation of Methods for FEA of Samples Fabricated Using FDM

The 3D model for the part specimen as per the dimensions taken from the ASTM standard has been prepared using the SolidWorks modeling software as shown in Fig. 2.
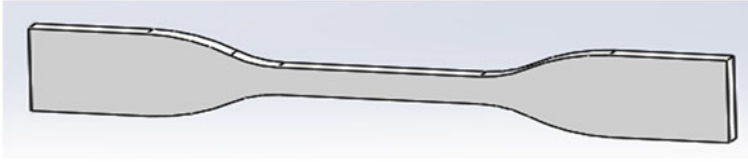
**Fig. 2** 3D model of PLA specimen as per ASTM standard

## 3.1    FE Simulation as per Kumar and Narayan [7] Approach

The stress analysis has been carried out on the tensile test specimen with maximum experimental loading condition. The gauge length has high-stress values when compared to the other regions of the specimen due to stress concentration and material plastic flow. The maximum von-Mises stress value of 66.68 MPa has been observed for PLA tensile specimens at 1000 N load as shown in Fig. 3. The experimental result for the same specimen has been obtained by the following procedure described in the next section is 35.72 MPa. The simulation approach given by Kumar and Narayan is not accurate enough to predict tensile stress result as 46.4% difference has been observed between simulation as per this approach and experimental results.



**Fig. 3** Von-Mises stress response of solid specimen to a 1000 N load

## 3.2 FE Simulation as per Farbman and McCoy's [10] Approach

The stress analysis has been performed on the tensile test specimen with maximum experimental loading condition as per this approach. The infill geometry has been modeled with dimension of 33 mm × 4 mm × 2 mm rectangular cuboid shape between gauge length portions in the specimens. The dimension of a line has been considered as 0.1 mm × 4 mm × 2 mm during 3D modeling. The infill geometry has been created in such a way that geometry should acquire 75% space of rectangular cuboid. The strength ratios for various infill patterns have been calculated using Eq. (1) [10].

$$\text{Stregth Ratio (SR)} = \frac{\frac{F_{\max}}{\text{mass}}}{\frac{F_{\max,\text{solid}}}{\text{mass}_{\text{solid}}}} \tag{1}$$

where, $F_{\max}$ is the maximum force applied during the test on the actual specimen, $F_{\max,\text{solid}}$ is the maximum force applied during the test on the specimen with 100% infill, i.e. completely solid.

The maximum von-Mises stress value of 83.87 MPa has been observed for PLA tensile specimens at 1000 N load as shown in Fig. 4a. The experimental result for the same specimen has been obtained by the following procedure described in the next section is 35.72 MPa. The high stress value has been observed at infill pattern location near gauge length portion as described in Fig. 4b. The simulation approach given by Farbman and McCoy is not accurate enough to predict tensile stress result as 57.4% difference has been observed between simulation as per this approach and experimental results.



**(a)**                    **(b)**

**Fig. 4** **a** Von-Mises stress response of specimen with 75% infill density and lines pattern as infill geometry to a 1000 N load, **b** higher stress near infill pattern at applied load side

### 3.3  FE Simulation as per Alafaghani et al. [9] Approach

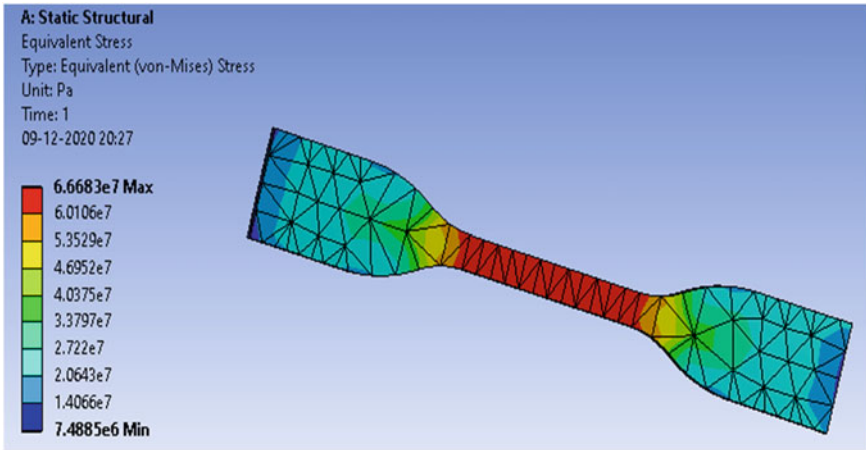The stress analysis has also been performed on the tensile test specimen with maximum experimental loading condition as per this approach. The 3D CAD model has been prepared with gaps and porosity as per the infill pattern by comparing density of CAD model with physical sample. The shape of gaps and porosity have been chosen as diamonds of dimensions 0.2 mm × 0.2 mm with 45° raster angle. Although in the actual FDM part the size of the discontinuities is much smaller, this size has been used to reduce the computation time and reduce the need for finer meshing. The number of holes per area (HPA) has been calculated according to Eq. (2) [9].

$$\rho_{\text{FDM}} = (V_{\text{CAD}} \times \rho_{\text{Filament}} - \rho_{\text{Filament}} \times l^2 \times T \times A_{\text{CAD}} \times \text{HPA})/V_{\text{CAD}} \quad (2)$$

where, $\rho_{\text{FDM}}$ is the apparent density of the FDM part, $V_{\text{CAD}}$ is the volume of the original CAD model, $\rho_{\text{Filament}}$ is the density of the filament, $T$ is the thickness of the specimen, $l$ is the length of the discontinuity, and $A_{\text{CAD}}$ is the area of the specimen in the X-Y plane.

Here, the shape of discontinuities has been considered as circular shape of diameter 0.2 mm with thickness of 4 mm. The density of filament and apparent density have been taken as 1240 kg/m$^3$ and 1191.2 kg/m$^3$, respectively. The required holes as per Eq. (2) has been calculated as 88. The maximum stress has been observed near the hole region due to stress concentration and plastic flow of material. The maximum von-Mises stress value of 55.76 MPa has been observed for PLA tensile specimens at 1000 N load as shown in Fig. 5. The experimental result for the same specimen has been obtained by the following procedure described in the next section is 35.72 MPa. The simulation approach given by Alafaghani is comparatively accurate to predict tensile stress result as 35.9% difference has been observed between simulation as per this approach and experimental results.



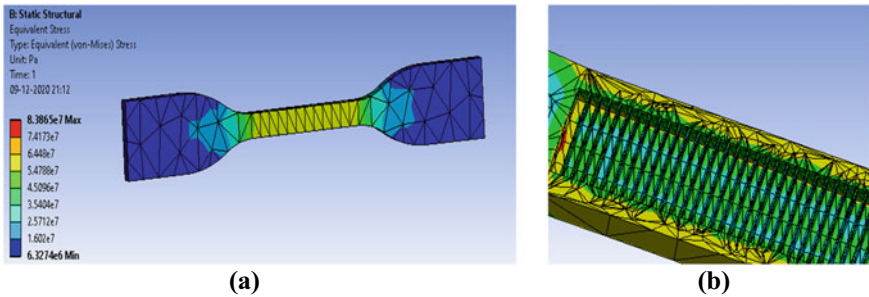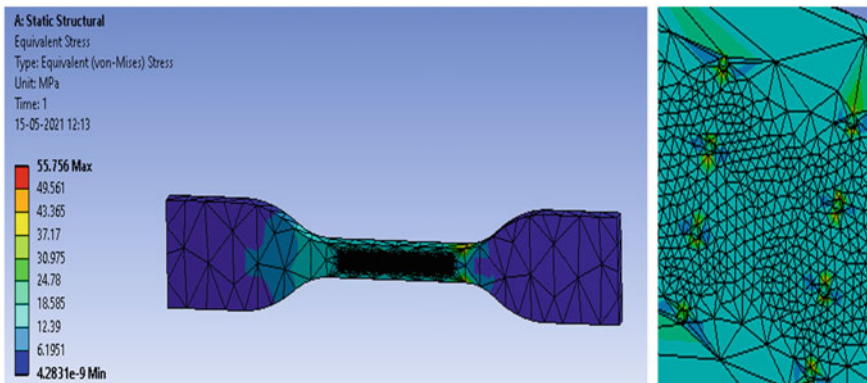**Fig. 5**  Von-Mises stress response of specimen with hole to a 1000 N load

The hole per area approach has been adopted for further FE simulation as this approach gives accurate results compared to other approaches. The simulation results have been further improved by increasing number of elements in discretization process.

## 3.4 Effect of Process Parameters on Tensile Strength Using Simulation Approach

The number of simulations has been performed by changing the process parameters—infill geometry, layer thickness, and number of perimeter. Three different layer heights, i.e. 0.06, 0.1, and 0.15 mm; three different infill geometry, i.e. tri-hexagonal, gyroid, and concentric; three number of perimeters, i.e. 2, 4, and 6 have been considered as process parameters. A total of nine simulations with the combination of each process parameter have been performed using hole per area approach. The tensile strength has been evaluated from simulations with the combination of each process parameter as per design of experiment. The density of each combination of process parameters has been calculated from mass and volume of the specimens as given in Table 1. The number of holes as well as simulation results of tensile strength for combination of each process parameter are shown in Table 1. The layer height is affecting the tensile strength of the parts. Thicker layers create more gaps and therefore print less dense and lesser strength components. So, the medium layer height gives the highest strength compared to very low or high layer height. The tri-hexagonal infill geometry gives lesser strength compared to concentric and gyroid infill geometry. This is due to a large number of void content present during printing with tri-hexagonal infill geometry. The number of perimeters is directly proportional to tensile strength because of part orientation and anisotropy in the material.

**Table 1** Density, number of holes for specimen, and simulation result of tensile strength

| Runs | Layer height (mm) | Infill geometry | Number of perimeter | Density (kg/m³) | Number of holes | Tensile strength (MPa)–simulation results |
|------|-------------------|-----------------|---------------------|-----------------|-----------------|-------------------------------------------|
| 1 | 0.06 | Tri-hexagonal | 2 | 931.7793376 | 1231 | 43.501 |
| 2 | 0.06 | Gyroid | 4 | 1158.019566 | 146 | 57.297 |
| 3 | 0.06 | Concentric | 6 | 1180.762823 | 106 | 67.563 |
| 4 | 0.100 | Tri-hexagonal | 4 | 1183.550706 | 101 | 55.62 |
| 5 | 0.100 | Gyroid | 6 | 1162.735909 | 138 | 61.986 |
| 6 | 0.100 | Concentric | 2 | 1179.990241 | 107 | 57.71 |
| 7 | 0.150 | Tri-hexagonal | 6 | 1230.686769 | 17 | 41.964 |
| 8 | 0.150 | Gyroid | 2 | 1162.084334 | 139 | 52.206 |
| 9 | 0.150 | Concentric | 4 | 1191.19268 | 87 | 55.756 |

## 4   Experimental Validations

In this study, FDM has been used for the fabrication of PLA specimens. The specimens as per desired dimensions have been fabricated using the Prusa MK3S FDM printer with combination of different process parameters. This 3D printer is capable of using a wide range of materials such as PLA, ABS, polycarbonate, flex, co-polyester, nylon, and composite materials. The build volume of $250 \times 210 \times 210$ mm, the layer height of 0.05–0.35 mm, and the filament diameter of 1.75 mm are specifications for the selected 3D printer. The PLA material has been loaded onto the machine in form of a spool. The material has been heated above its melting temperature and then extruded onto the build platform using the nozzles. The FDM machine uses two nozzles, which work alternatively, one for depositing the build material and the other for depositing the support material [12]. The contour has been first laid to form the boundary and then the interior portion filled as raster filling for each layer [13]. The raster filling for each consecutive layer varies by 90° to obtain adequate interlayer bonding between the layers. The longer dimension of specimen during printing has been kept parallel to build platform to minimize requirement of support structures and printing time. The thickness of specimen has been kept in Z direction, i.e. layer thickness direction to improve the quality of printed samples. In the present experimentation, PLA material has been used for support material, which is same as the main material. The extrusion head moves in the X-Y direction whereas the bed moves in the Z direction. The tensile strength has been measured for each fabricated sample. The comparison for the tensile strength obtained using simulation approach and experimental approach has been shown in Fig. 6. The runs mentioned in Fig. 6 are the same as Table 1 based on the combination of various process parameters. At least three specimens for each run have been tested for tensile strength to check the accuracy and consistency of the results. The percentage difference between simulation and experimental results is in the range of average 15–25%. The tensile strength obtained through experimentation is lesser than the tensile strength observed during simulation. The reason for the same is the finite element model used during simulation is not accurate in terms of discretization and boundary conditions. Also, the void present in the fabricated samples during the printing process is not perfectly exhibited during the simulation approach. But, the same trend for tensile strength has been observed for simulation and experimental results.

## 5   Conclusions

The finite element analysis of 3D printed PLA samples fabricated using the FDM method of additive manufacturing has been performed. The infill geometry and density have direct effects on the surface quality and mechanical properties of 3D printed products. Three patterns, namely, tri-hexagonal, gyroid, and concentric have been selected and the CAD model is designed with different densities. Three-layer
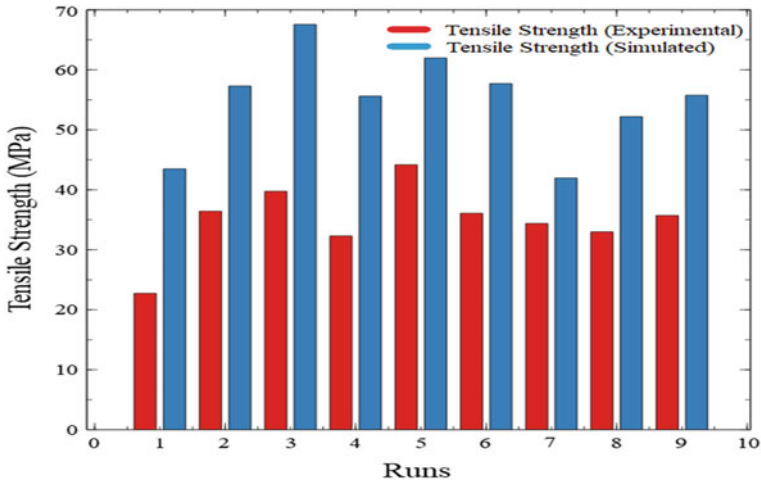
**Fig. 6** Comparison of tensile strength obtained by experiment and simulation approach

thicknesses and three number of perimeters have been considered during experimental work. Three different simulation approaches have been utilized to perform stress analysis. The von-Mises stress values obtained from each approach have been compared with experimental results. Further simulations have been performed based on a more accurate approach with the combination of process parameters. The results of tensile strength have been compared for simulation and experimental methods and observed the same trend. The average percentage difference between simulation and experimental results is in the range of average 15–25%.

# References

1. Carew RM, David E (2020) An overview of 3D printing in forensic science: the tangible third-dimension. J Forensic Sci 65(5):1752–1760
2. Mazzanti V, Lorenzo M, Francesco M (2019) FDM 3D printing of polymers containing natural fillers: a review of their mechanical properties. Polymers 11(7):1094
3. Torres J, Cole M, Owji A, DeMastry Z, Gordon AP (2016) An approach for mechanical property optimization of fused deposition modeling with polylactic acid via design of experiments. Rapid Prototyp J 22(2):387–404
4. Abeykoon C, Sri-Amphorn P, Fernando A (2020) Optimization of fused deposition modeling parameters for improved PLA and ABS 3D printed structures. Int J Light Mater Manuf 3(3):284–297
5. Dey, Yodo N (2019) A systematic survey of FDM process parameter optimization and their influence on part characteristics. J Manuf Mater Process 3(64)
6. Xinhua L, Shengpeng L, Zhou L, Xianhua Z, Xiaohu C, Zhongbin W (2015) An investigation on distortion of PLA thin-plate part in the FDM process. Int J Adv Manuf Technol 79(5):1117–1126
7. Kumar SA, Narayan YS (2018) Innovative design, analysis and development practices in aerospace and automotive engineering. Springer, Singapore (I-DAD 2018)

8. Cattenone A, Morganti S, Alaimo G, Auricchio F (2019) Finite element analysis of additive manufacturing based on fused deposition modeling: distortions prediction and comparison with experimental data. J Manuf Sci Eng 141(1):011010

9. Alafaghani A, Qattawi A, Alrawi B, Guzman A (2017) Experimental optimization of fused deposition modelling processing parameters: a design-for-manufacturing approach. Procedia Manuf 791–803

10. Farbman D, McCoy C (2016) Materials testing of 3D printed ABS and PLA samples to guide mechanical design. In: International manufacturing science and engineering conference, vol 49903. American Society of Mechanical Engineers

11. Lanzotti M, Grasso G, Staiano G, Martorelli M (2015) The impact of process parameters on mechanical properties of parts fabricated in PLA with an open-source 3-D printer. Rapid Prototype J 21(5):604–617

12. Chokshi H, Shah D, Patel K, Joshi S (2021) Experimental investigations of process parameters on mechanical properties for PLA during processing in FDM. Adv Mater Process Technol 1–14

13. Luzanin O, Movrin D, Plancak M (2017) Effect of layer thickness, deposition angle, and infill on maximum flexural force in FDM-built specimens

# Osteogenicity and Antibacterial Property of Polarized HA-UHMWPE Composites as Orthopedic Implant Biomaterial

**Subhasmita Swain, Itishree Priyadarshini, and Tapash Ranjan Rautray**

**Abstract** For developing a biomedical implant as a bone substitute material, the implant has to be developed in a way to accepts the surrounding tissues anatomically and physiologically. Because of its enhanced wear and impact resistance and low coefficient of friction, ultra-high molecular weight polyethylene (UHMWPE) can be used as a biomaterial. Its bioinert property can be compensated by using this material in combination with hydroxyapatite (HA). Since natural bone is a piezoelectric material, mimicking this property was achieved by polarizing this synthesized composite at high voltage. The electrical polarization of the prepared composites was carried out and osteoblast and bacterial cells were seeded on these surfaces. The cell viability on the polarized composites was found to be elevated after 7 and 14 days of culture as compared to the unpolarized composites. The osteogenic gene expression of RUNX2, COL1 and OCN on the polarized composites was increased by 35%, 21%, and 30% respectively as compared to the unpolarized specimens on day 14 of culture. It was observed that there was a significant decrease in *S. aureus* during all periods for the polarized HA+UHMWPE specimens. Because of the absence of electric polarization, the unpolarized specimen did not show sufficient antibacterial properties. It can be inferred from the present investigation that the negatively polarized HA+UHMWPE composites may be used as a preferred implant material as compared to the unpolarized HA+UHMWPE composites.

**Keywords** Hydroxyapatite · UHMWPE · Polarization · Osteogenicity · Antibacterial

S. Swain · I. Priyadarshini · T. R. Rautray (✉)
Biomaterials and Tissue Regeneration Laboratory, ITER, Siksha 'O' Anusandhan (Deemed to be University), Bhubaneswar 751030, Odisha, India
e-mail: tapashrautray@soa.ac.in

# 1 Introduction

Over the last few years, different kinds of advanced materials engineered to replace the natural bone have been used in orthopedic surgical procedures such as bone grafting and total hip replacement, etc. Besides the engineering and mechanical aspects, the biocompatibility factor is the foremost requisite for the selection of implant material that may prevent any adverse reaction in the body [1–3]. Biocomposites pose to be the most suitable orthopedic implant material since their mechanical as well as biological properties can be tailored to a specific environment. Yet, the commercial successes of these materials are limited on account of the difficulty associated with their fabrication, design, and testing procedures [4]. The rising demand for getting optimum quality and stability of implant material necessitates the development of novel materials as well as improvement of the existing materials used. The bone can be regarded as a natural biocomposite [5]. A structural hierarchy can be seen in bone from the nano to micro level. The structure of bone on the nano-scale consists of organic collagen fibrils with reinforced nano-crystals of hydroxyapatite (HA, $(Ca_{10} (PO_4)_6(OH)_2)$) mineral. The collagen fibrils in the bone are aligned periodically with HA nano-crystals embedded in them. This arrangement provides structural and mechanical rigidity to the bone [6, 7]. To achieve similar mechanical properties, the synthetic biocomposites should have a microstructure similar to that of bone.

Apart from biocompatibility, HA shows bioactive properties [8, 9] by which it stimulates bone growth, thus aiding in speedy recovery from bone damage. It also acts as a resource of phosphorous and calcium required for bone tissue development. At present, the mechanical property, biocompatibility, and osteointegration of biopolymer composites are enhanced by incorporating HA as filler material [10].

Ultra-high molecular weight polyethylene (UHMWPE) bears excellent mechanical properties such as higher impact resistance, wear resistance, and low coefficient of friction. Mirsalehi et al. in 2016 reported that the biocompatibility property of UHMWPE makes it a worthy material to be used as an orthopedic implant. Nevertheless, the UHMWPE being bioinert cannot provide bone adherence and promote cell growth. Subsequently, its combination with a biocompatible material can be used for biomedical applications [11].

Bonfield et al. [12] were the first to introduce the composite of high-density polyethylene (HDPE) with HA reinforcement. Following their work, researchers have proposed many biocomposites involving polymer matrices. The major drawback of these composites is their inferior mechanical strength, which does not permit their use in applications where load-bearing capacity is needed. It has been observed that dried bone when subjected to mechanical stress generates an electric charge. They could also illustrate the converse effect where electric field when applied to bone produces strain. Hence, it was proposed that biomaterials can imitate this piezoelectric behavior of bone and the development of biocompatible materials could be an important tool for orthopedic therapeutic purposes.

Numerous studies demonstrated that cell behavior changes when the surface of the implant is electrically charged. It has been seen that different types of cells grow under the influence of electric stimulation while some studies suggested the regeneration of nerve cells. The charged surface-induced cell adhesion influenced the morphology. All the aforementioned studies were executed on surface coatings and two-dimensional polymer films. Hence, various tissue engineering applications like bone and nerve regeneration may benefit from the use of an electrically charged fibrous scaffold [13].

Recent studies revealed that when sintered bioceramic is polarized, a permanent residual charge is created on the backside. Due to this charge, the cells attached to it get stimulated and the cell activity and response are enhanced. Moreover, HA sintered in water vapor is more conductive than that sintered in air. The water vapor present through the sintering process prevents $OH^-$ ions to dehydrate. As a consequence $OH^-$ ions move through the sub-lattice channels and the proton conductivity is enhanced due to this rotation of $OH^-$ ions. In air medium, vacancies are created because $OH^-$ ions encounter partial dehydration and the movement of these vacancies within the structure governs the conductivity [14].

In the present work, HA in combination with UHMWPE bioactive composites was prepared by a twin-screw extrusion method and are polarized by using a corona polling unit and their osteoconductivity and antibacterial activity were studied. The goal of this study is to demonstrate that it can potentially be used as a tissue engineering material.

## 2　Materials and Methods

### 2.1　Specimen Preparation and Polarization

The UHMWPE (Goodfellow Co., London, UK) used in the present study has an average particle size of 2 $\mu$m with an average molecular weight of $6 \times 10^6$ g/mol. The wet synthesized HA powder used has a similar size of 2 $\mu$m.

The synthesized HA was mixed with UHMWPE powder (in a 7:3 ratio) with a volume fraction of 0.5 (i.e. VHA = 0.5). The mixture was then compounded using a co-rotating Haake Record 90 (Bersdorff, Germany) twin-screw extrusion method at 5 rpm with pharmaceutical-grade paraffin oil as a swelling agent and the mold was obtained by hot pressing. Rectangular strips of dimension 3 mm × 30 mm × 5 mm were obtained by cutting the mold. The composite processing details were presented as described [15].

Before poling, the specimens were coated with silver on both upper and lower surfaces and negatively polarized at a polarization voltage of 2 kV/mm at 480 °C. As soon as the polling was done, the silver coating attached to both the surfaces was removed and polished using 400 grit-sized sandpaper. Particle-induced X-ray emission PIXE technique was employed to ensure no trace of silver was left on

both the surfaces of the specimen [16]. Hereafter negative polarized HA+UHMWPE composite will be referred to as 'N poled composite'.

ASTM D638 Type I procedure was adopted for tensile test measurements and it was performed using a universal testing machine (H100KS, Hounsfield Co., England) with a 100 kN load. The results of the test were the mean of three measurements.

## 2.2 In Vitro Analyzes

### 2.2.1 Cell Culture

MG63 osteoblast-like cells (ATCC, CRL-1427, homo sapiens) were cultured in Dulbecco's modified eagle medium (DMEM) loaded with 10% fetal bovine serum (FBS), 100 units $mL^{-1}$ of penicillin, and 100 mg $mL^{-1}$ of streptomycin and the solution was incubated at 37 °C with 5% $CO_2$ atmosphere.

### 2.2.2 Cell Viability Test

To evaluate viable cell density, MTT [3-(4,5-dimethylthiazol-2-yl)-2,5-diphenyltetrazolium bromide] assay was employed. Composite pellets were placed in 96 multiwell-plates, and MG-63 cells were maintained at a density of $3 \times 10^4$ cells/well and incubated for 24 h, followed by incubation for 1, 7, and 14 days. Subsequently, the substrates were cleaned by DMSO to extract the nonadherent cells and placed on a new 96 multiwell plate at predetermined time points. The same process was repeated for different time points for different pellets. The absorbance of the MTT solutions was recorded and the cell viability was estimated by employing a spectrophotometer microplate reader ($\lambda = 490$ nm).

## 2.3 Real-Time Polymerase Chain Reaction (RT-PCR) Analysis

The gene expression for establishing osteogenicity for type 1 collagen (COL1), osteocalcin (OCN), and RUNX2 were measured by using an RT-PCR (Bio-Rad Laboratories, USA). Composite pellets with a diameter of 3 mm placed in a 96-multiwell plate were seeded with $3 \times 10^4$ cells/well and were cultured for 1, 7, and 14 days. Trizol Reagent (Invitrogen, USA) was used for cell lysing and the lysates were collected by centrifugation. The cells on each disk were lysed and the lysates were collected by pipetting and centrifugation and the total cellular RNA was extracted as per the user manual and quantified using a UV spectrophotometer (Beckman DU-600) [17]. Table 1 shows the forward and reverse primers for the target genes.

**Table 1** Forward and reverse primer sequence

| Gene | Forward primer sequence (5′–3′) | Reverse primer sequence (5′–3′) |
| --- | --- | --- |
| COL 1 | CCCCAGCCACAAAGAGTCTA | GGATCATCCACGTCTCGTTT |
| OCN | CTGAGAGGAGGAAGCACCAT | CCATCCTCATACCTGCACCT |
| RUNX2 | CACCGAGACCAACAGAGTCA | TGCTTGCAGCCTTAAACTGA |

## 2.4 Bacterial Viability Test

The in vitro bacterial viability of the N poled HA+UHMWPE and unpoled HA+UHMWPE composite surfaces were studied on Gram-positive Staphylococcus aureus (*S. aureus*) by MTT assay. The microbes were cultured in a Mueller–Hinton Broth (MHB) medium at 37 ℃ for 6 h, and their concentration was set at $1 \times 10^6$ CFU/mL. Then the composite pellets were placed in the center of a 24-multiwell plate and each pellet was placed in a $CO_2$ incubator in 1 mL of bacteria cell suspension at 37 ℃. The bacterial cell culture was performed for 10, 20, and 30 h after which evaluation of adherent cells was conducted for bacterial viability by adding 150 µL of microbe suspension with 150 µL of MTT solution (5 mg mL$^{-1}$). Each test was performed in triplicate. The bacterial viability was monitored by taking OD readings of the substrate solution [18, 19].

## 2.5 Antibacterial Rate Test

The antibacterial rate test was conducted for estimating the potential of bacterial cells on the specimens as per our previous study [18].

## 2.6 Statistical Analysis

In the present study, the quantitative results are expressed as mean ± SD value and examined using SPSS software 24.0, and a student's t-test was performed to test the significance of the results. $P < 0.05$ was considered to be statistically significant.

## 3 Results

### 3.1 MTT assay

Figure 1 depicts the osteoblast cell viability of MG63 cells cultured on N poled and unpoled HA-UHMWPE composites for 1, 7, and 14 days. While no change was observed in the viability of cells on day 1, a significant increase in osteoblast cells on polarized specimens was observed on day 7 and day 14 ($p < 0.05$).

### 3.2 Gene Expression

The relative expressions of COL1 (Fig. 2), OCN (Fig. 3), and RUNX2 (Fig. 4) with SD were carried out on the poled and unpoled composites of HA+UHMWPE for 1, 7, and 14 days. While the progressive increase in the relative expression of RUNX2 was observed on the polarized specimens on days 1 and 7 ($p < 0.05$), there was a significant increase on the polarized specimen on day 14 ($p < 0.05$). Insignificant gene expression of extracellular bone matrix OCN and COL1 was observed on both the polarized and unpolarized specimens on days 1 and 7 but there was a significant increase in gene expression of OCN and COL1 on the polarized specimen on day 14 ($p < 0.05$) thus showing the osteogenicity of the polarized specimen. The increase in gene expressions may be attributed to the polarization mechanism inducing higher osteogenicity.

### 3.3 Bacterial Viability Test

The bacterial cell viability of *S. aureus* was conducted on the polarized and unpolarized specimens of HA+UHMWPE for 10, 20, and 30 h (Fig. 5). It was observed that there was a significant decrease in *S. aureus* during the all-time point for the

**Fig. 2** Osteogenic expression of COL 1
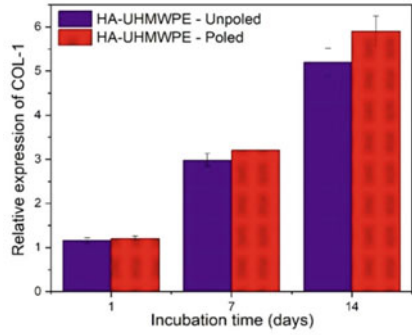


**Fig. 3** Osteogenic expression of OCN
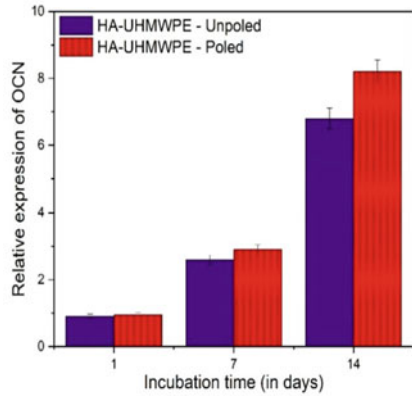


**Fig. 4** Osteogenic expression of RUNX2
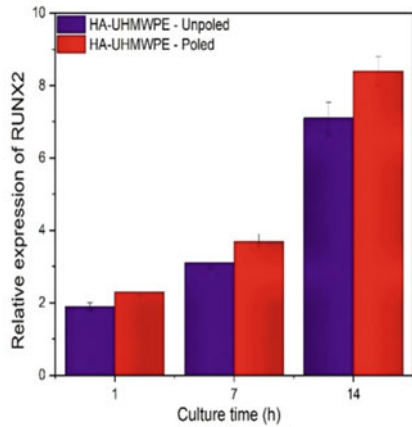
**Fig. 5** Bacteria viability of the composites
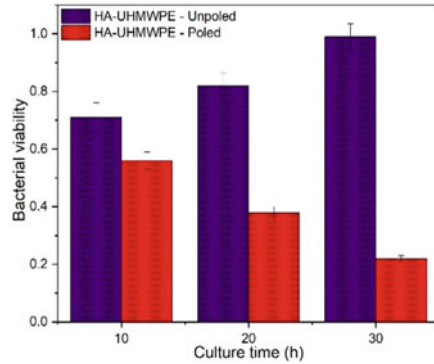


polarized specimen. While bacteria viability progressively increased for the unpolarized samples for 10, 20, and 30 h, there were progressive decreases in *S. aureus* on the polarized specimens. At 30 h, there was a significant reduction in several viable bacteria on the polarized specimens exhibiting the induction of antibacterial activities due to the polarization of the specimens.

## 3.4 Antibacterial Rate Test

The antibacterial rate percentage reduction test of *S. aureus* was carried out for 10, 20, and 30 h (Fig. 6). It was observed that the polarized HA+UHMWPE specimen showed higher efficacy in reducing the number of bacterial cells. Because of the absence of electric polarization, the unpolarized specimen did not show sufficient antibacterial properties.

**Fig. 6** Antibacterial rate percent reduction on the composites
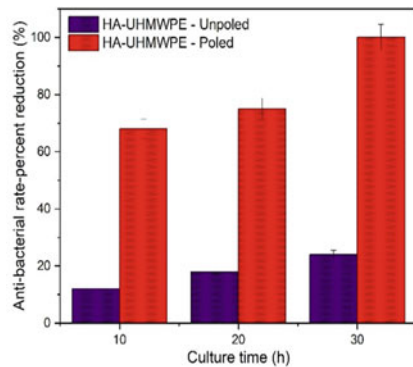
## 4 Discussion

The composites of polymer matrix have high design flexibility such that their elastic modulus can be tailored to match that of bone. This attributes to the widespread use of these materials in orthopedic implants [20]. The reinforcement of secondary particles [metals, ceramics, polymers) into the composites of UHMWPE has shown to increase the mechanical properties significantly [21, 22]. Among all, HA has the highest bonding efficiency to the surrounding tissue. The stability against bone resorption comes from its firm chemical composition. Other than its outstanding biocompatibility, HA shows reasonably good surface activity making it a noble bioactive material for bone implants. Moreover, the structural and chemical similarity of HA to the bone matrix makes the implant fixation durable [8]. The natural bone matrix contains nano-sized HA crystals attached with the collagen. The non-collagenous proteins like osteocalcin and osteopontin which makes up around 3–5% of the bone are responsible for the binding of HA with collagen. These proteins act as active sites for the attachment of cells as well as for the biomineralization process [23].

No studies to date can explain the mechanism of HA polarization properly. Earlier reports suggest that the polarization in HA results in the transformation phenomenon of monoclinic to hexagonal at high temperatures. However, the presence of a large amount of stored charge in a polarized HA contradicts the explanations in those reports. Recently, a relatively justifiable poling mechanism was proposed by Ueshima et al. [24]. According to this model, at a lower temperature (below 400 °C) the polarization in HA occurs due to the movement of protons inside the columnar $OH^-$ channels of the hexagonal unit cell whereas at a high temperature (above 500 °C), dehydration of HA starts which leads to oxygen diffusion with proton migration giving rise to polarization [24]. Since the poling temperature in the present study is below 500 °C, the former model where proton migration takes place along the columnar $OH^-$ channels forms the mechanism for HA polarization. The HA samples used for polarization treatment have a relative sintered density of 90–91%. It is evident from various studies that, different parameters like poling temperature, porosity, applied electric field, and phase purity greatly influence the polarizability of HA [25, 26].

Our experiment on N poled HA+UHMWPE resulted in higher surface occupancy by osteoblast cells. The cell attachment and growth are more profound when the surface energy of the material is high whereas the contact angle with the cell is low. On N surfaces, within 7 days cells assumed flattened and spread morphology, indicating a final stage of cell attachment. In the case of N poled surface, $Ca^{2+}$ ion, as well as some cell adhesive proteins (vitronectin, fibronectin, etc.), gets absorbed making space for more sites on HA surface for osteoblast cell adhesion. Despite having the same surface energies, the negatively poled surface shows better cell adhesion than the positively poled surface. It is because some anti-adhesive substances like $HCO^{3-}$ are selectively attracted towards the positively poled surface, thus reducing the cell attachment. The MTT assay results are consistent with these facts. In the case of the N poled surface, the cell growth rate was rapid for the first 7 days and then declined

after that. However, in the case of P poled surface, the growth was slow for the first 7 days and then increased for 7–14 days since the surface charge effect subsided by that time.

In the present study, negatively polarized HA+UHMWPE specimen significantly enhanced the expression of osteogenic expression of RUNX2, OCN, and COL1.COL1 is termed as the early marker of the bone mineralization process that forms an extracellular matrix, but on the other hand, RUNX2 is expressed in the later phase of bone mineralization. The polarized specimen significantly induced promotive expression of osteogenic related genes thus demonstrating outstanding bioactivity produced due to the presence of polarization. To validate its mechanism further experiments will be conducted to understand the detailed signal pathway.

*S. aureus* was cultured on both polarized and unpolarized HA+UHMWPE composites and its behavior on these surfaces was assessed. The negatively polarized composite was found to exhibit higher antibacterial activity which was congruent to our earlier study [18] depicting the antibacterial effect of polarization. Bacterial infection has been frequently found to have deleterious effects on biomedical implant sites causing implant failures and revision surgery. So many methods have previously been adopted to prevent the bacteria developed on implant sites either targeting the disruption of cell respiration or their division or metabolism or cell membrane. But the current approach to bacterial death or prevention due to implant surface polarization would solve many problems relating to localized antibacterial effects simultaneously enhancing the biocompatibility of the implant. In the present study, the biocompatibility of the specimen was envisaged to increase after polarization. Previous studies have shown that bacterial inhibition occurs in the presence of an external electric field [27]. The principle behind the killing of bacteria may be ascribed to the electrolysis of molecules on bacterial membrane producing $H_2O_2$, $Cl^-$ molecule, and oxidizing radicals thus breaking the bacterial membrane. So it can be concluded that a negatively polarized surface can effectively act to disrupt bacterial membrane producing strong antibacterial activity. In one of our earlier studies, a 42.1% reduction in *S. aureus* cells on a positively charged HA surface and a 28% reduction in *S. aureus* cells on a negatively charged HA surface were observed [26].

## 5   Conclusion

The MTT assay exhibited considerable enhancement in osteoblast cell numbers on polarized specimens on day 7 and day 14. The relative expression of RUNX2 showed a significant increase on the polarized specimen on day 14. There was a significant increase in gene expression of OCN and COL1 on the polarized specimen on day 14 thus showing the osteogenicity of the polarized specimen. The bacterial cell viability of *S. aureus* conducted on the polarized and unpolarized specimens showed a significant decrease in *S. aureus* for the polarized specimen. It was observed that the polarized HA+UHMWPE specimen showed higher efficacy in reducing the number of bacterial cells.

# References

1. Rautray TR, Narayanan R, Kim KH (2011) Prog Mater Sci 56:1137–1177
2. Swain S, Rautray TR, Narayanan R (2016) Adv Sci Lett 22:482–487
3. Swain S, Misra RDK, You CK, Rautray TR (2021) Mater Technol 36:393–399
4. Evans SL, Gregson PJ (1998) Biomaterials 19:1329–1342
5. Swain S, Rautray (2021) In: Swain BP (ed) Nanostructured materials and their applications Singapore. Springer, pp 55–80
6. Rho JY, Spearing LK, Zioupos P (1998) Med Eng Phys 20:92–102
7. Kim KH, Rautray TR, Narayanan (2010) Nova Science Publishers, R Korea
8. Kokubo T, Kim HM, Kawashita M (2003) Biomaterials 24:2161–2175
9. Behera DR, Nayak P, Rautray TR (2020) J King Saud Univ Sci 32:848–852
10. Zuo Y, Li Y, Li J, Zhang X, Liao H, Wang Y, Yang W (2007) Mater Sci Eng A 452–453:512–517
11. Mirsalehi SA, Sattari M, Khavandi A, Mirdamadi S, Naimi-Jamal MR (2016) J Compos Mater 50:1725–1737
12. Bonfield W, Grynpas M, Tully AE, Bowman J, Abram J (1981) Biomaterials 2:185–186
13. Weber N, Lee YS, Shanmugasundaram S, Jaffe M, Arinzeh TL (2010) Acta Biomater 6:3550–3556
14. Kumar D, Gittings JP, Turner IG, Bowen CR, Bastida-Hidalgo A, Cartmell SH (2010) Acta Biomater 6:1549–1554
15. Fang L, Leng Y, Gao P (2006) Biomaterials 27:3701–3707
16. Swain S, Padhy RN, Rautray TR (2020) J Korean Ceram Soc 57:495–502
17. Swain S, Ong JL, Narayanan R, Rautray TRT (2021) J Biomed Mater Res Part B Appl Biomater 109:2154–2161
18. Swain S, Padhy RN, Rautray TR (2020) Mater Chem Phys 239:122002
19. Swain S, Rautray TR (2020) Biol Trace Elem Res 199:1185–1193
20. Tourani H, Molazemhosseini A, Khavandi A, Mirdamadi S, Shokrgozar MA, Mehrjo M (2013) Polym Compos 34:1961–1969
21. Hashimoto M, Takadama H, Mizuno M, Yasutomi Y (2002) Key Eng Mater 240:415–418
22. Zhou J, Yan F (2005) J Appl Polym Sci 96:2336–2343
23. Ramakrishna SR, Mayer J, Wintermantel E, Leong KW (2001) Compos Sci Technol 61:1189–1224
24. Ueshima M, Nakamura S, Yamashita K (2002) Adv Mater 14:591
25. Nakamura S, Takeda H, Yamashita K (2001) J Appl Phys 89:5386–5392
26. Swain S, Bowen C, Rautray TR (2021) J Biomed Mater Res A 109:2027–2035
27. Van der Borden AJ, Van der Mei HC, Busscher HJ (2005) Biomaterials 26:6731–6735

# Applications of Ionic Liquids in Solvent Extraction of Optically Active Metals Gallium and Indium-An Overview

**Laxmipriya Sahu** and **Sujata Mishra**

**Abstract** In this sustainable thriving, material starved world, the importance of technologically important metals like gallium and indium is desperate. Gallium and indium having excellent optical properties, have vast uses in solar cells, semiconductors liquid crystals, etc. These are seldom found as individual ores in the earth's crust and usually are seen as by products of aluminum and zinc ores. Resources of metals are quickly exhausting which led to the necessity of extracting metals values from low grade ores and other secondary resources where the contents of these are very low. Ionic liquids as solvent extractants are environmental friendly and used in the separation of various metal ions. These eco-friendly solvents have got immense applications in the fields of hydro metallurgy ascribable to their specific characteristics like non-volatility, inflammability, less toxicity and appreciable ionic conductivity. Solvent extraction being a low energy feeding technique, it has capably contributed to the careful separation and recovery of these metal ions. With most of the conventional extractants, the separation of Ga and In becomes difficult as reported in the literature. Therefore, use of the green extractants such as ionic liquids could be a response to the problem faced for the separation of these metal ions. There is an urgent need for the development of novel and low carbon recycling paths which may contribute to ensure to meet the upcoming demand of gallium and indium. In this present review, solvent extraction of Ga and In using these ionic liquids with reference to process optimization, selectivity and regeneration studies are looked upon in detail.

**Keywords** Ionic liquids · Gallium · Indium · Solvent extraction · Process optimization

L. Sahu · S. Mishra (✉)
Department of Chemistry, Institute of Technical Education and Research (FET), Siksha 'O' Anusandhan Deemed to be University, Bhubaneswar, Odisha 751030, India
e-mail: sujatamishra@soa.ac.in

## Abbreviations

| | |
|---|---|
| $[C_{1mim}][NTf_2]$ | 1,3-Dimethylimidazoliumbis(trifluoromethylsulfonyl)imide |
| $[C_{2mim}][PF_6]$ | 1-Ethyl-3-methylimidazoliumhexafluorophosphate |
| $[C_{2mim}][NTf_2]$ | 1-Ethyl-3-methylimidazolium bis(trifluoromethylsulfonyl)imide |
| $[C_{2mim}][Beti]$ | 1-Ethyl-3-methylimidazolium |
| $[C_{3mim}][PF_6]$ | 1-Propyl-3-methylimidazolium hexafluorophosphate |
| $[C_{2eim}][NTf_2]$ | 1,3-Diethylimidazolium bis(trifluoromethylsulfonyl)imide |
| $[C_{2mim}][SCN]$ | 1-Ethyl-3-methylimidazolium thiocyanate |
| $[C_{4mim}][SCN]$ | 1-Butyl-3-methylimidazolium thiocyanate |
| $[C_{5mim}][NTf_2]$ | 1-Pentyl-3-methylimidazolium bis(trifluoromethylsulfonyl)imide |
| $[C_{8mim}][NTf_2]$ | 1-Octyl-3-methylimidazolium bis(trifluoromethylsulfonyl)imide |
| $[A324H^+][Cl^-]$ | Triisooctylamminonium chloride |
| $A327H^+Cl^-$ | Mixture of tri-octyl and tri-decyl ammonium chloride |
| ALi-CY | Aliquat 336 and Cyanex 272 |
| ALi-PC | Aliquat 336 and PC 88A |
| ALi-D2 | Aliquat 336 and D2EHPA |
| $[Hbet][Tf_2N]$ | Betainium bis(trifluoromethyl sulfonyl) imide |
| $[N1116][TFSA]$ | *n*-Hexyl-trimethyl ammonium bis(trifluoromethyl-sulfonyl)amide |
| $H[TFSA]$ | 1,1,1-Trifluoro-*N*-[(trifluoromethyl)sulfonyl]methane sulfon-amide |
| $[MTOA][NTf_2]$ | Bis (trifluoromethanesulfonyl) imide |
| $[B_{MIm}][NTf_2]$ | 1 Butyl 3 methylimidazolium bis(trifluoromethylsulfonyl)imide |
| $[TOAH][NTf_2]$ | Trioctylammonium bis (trifluoromethanesulfonly)amide) |
| $[TOAH][NO_3]$ | Trioctylammonium nitrate |
| Aliquat 336 | Tricaprylylmethylammonium chloride |
| Cyphos 101 | Trihexyl(tetradecyl)phosphonium chloride |
| $[MTOA][I]$ | Methyltrioctylammonium iodide |
| Kelex100 | 7-(4-Ethyl-1-methyloctyl)- 8-hydroxyquinoline |
| $[HHT_{12}][Tf_2N]$ | 4-Ethyl-5-methyl-1,3-dihexyl-1,2,3-triazolium bis(trifluoromethylsulfonyl)imide |
| $[Hbet][Tf_2N]$ | Bis(trifluoromethylsulfonyl)imide |
| $[EhEhT_{23}]_2[SO_4]$ | 4-Ethyl-1,3-bis(2-ethylhexyl)-5-propyl-1,2,3-triazolium sulfate |
| $[P_{44410}][Br_3]$ | Trihalide ionic liquid tributyldecylphosphonium tribromide |

# 1   Introduction

Traditional organic solvents often give off volatile organic compounds when they are being used, which can be harmful for the environment and also for those who are working near the site. Ionic liquids (ILs) can make the separation process simpler

**Table 1** Melting temperatures of some imidazolium based RTILs

| Ionic liquids | Melting point (°C) | References |
|---|---|---|
| $[C_{1mim}][NTf_2]$ | 22 | [3] |
| $[C_{2mim}][PF_6]$ | 62 | [4] |
| $[C_{2mim}][NTf_2]$ | −15 | [4] |
| $[C_{2mim}][Beti]$ | −1 | [4] |
| $[C_{3mim}][PF_6]$ | 40 | [5] |

**Table 2** Critical temperatures of some imidazolium based RTILs [6]

| Ionic liquids | Critical temperature (K) |
|---|---|
| $[C_{2eim}][NTf_2]$ | 1254.7 |
| $[C_{2mim}][SCN]$ | 1013.6 |
| $[C_{4mim}][SCN]$ | 1047.4 |
| $[C_{5mim}][NTf_2]$ | 1281.1 |
| $[C_{8mim}][NTf_2]$ | 1317.8 |

and more efficient [1]. These are emerging as promising green solvents to substitute conventional organic solvents in recent years. ILs possess exceptional characteristics like non-volatility, low toxicity, easy handling, non-flammability and more ionic conductivity and hence have gained attention in the green extraction process. ILs are broadly appropriate for use in organic reactions and can also improve the regulation of product distribution, higher reactivity, product recovery and recycling. ILs are proved to be environmentally friendly and green solvents [2]. These are usually described as composites of ionic components having melting point less than 100 °C. ILs have extensive ranges of properties which make them fit for different applications. IL has low melting temperature. Those that remain liquid at or below room temperature are mentioned as room temperature ionic liquids (RTILs). They have generally very low vapor pressures, and hence are very unlikely to evaporate. Melting points and critical temperature data of few RTILs are displayed in Tables 1 and 2.

The metal gallium is not found naturally in its primary form or in a clean form and is formed largely in bauxite treatment or as the remaining form of zinc processing deposits. It can also be seen in germanite and copper sulphide ore. The concentration of Ga found in bauxite and zinc ores is 50 ppm. The mechanism of extraction is very slow, and needs more time. The ion exchange is the main pathway for gallium extraction, using Bayer's liquor applied in the manufacturing of steel [7]. Indium is obtained mostly from residues resulted during zinc ore processing. It is also extracted from iron, lead and copper ores [8]. Solvent extraction is an effective process for the extraction and separation of Ga and In which is schematically represented in Fig. 1. In this review, the solvent extraction of two optically active metals such as gallium and indium using different types of ionic liquids has been presented in order to draw conclusions regarding the future scope for using these environmentally benign extractants for quantitative recovery of these optically active metals from various resources.

**Fig. 1** Schematic representation of solvent extraction process using ILs
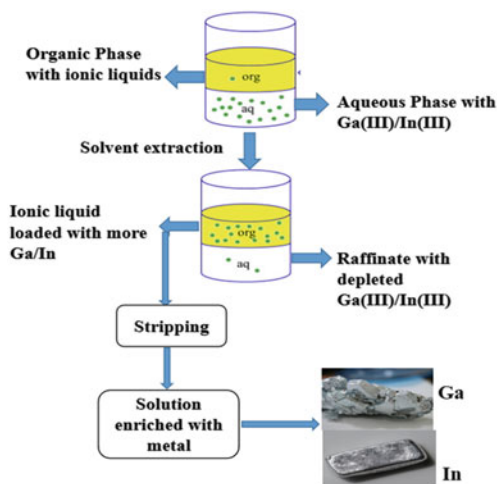


## 2 Extraction Overview

### 2.1 Using Ammonium Ionic Liquid

Alugacil and Escudero [9] have carried out the extraction of In(III) from 0.1 to 6 M HCl using the IL, [A324H$^+$][Cl$^-$]. They synthesized the IL from triisooctyl amine (A324) diluted in Solvesso 100 and 1 M HCl. They reported that In(III) extraction was routed through anion exchange mechanism which occurred between the Cl$^-$ of the IL and the tetrachloro indium species present in the aqueous phase. They found that In(III) could be back extracted from the loaded organic extract using dilute HCl as a stripping agent and subsequent precipitation with the use of NaBH$_4$. The extraction of In(III) from HCl medium through the membrane was investigated by Alugacil [10] by using the ammonium IL, A327H$^+$Cl$^-$ diluted with solvesso 100. Indium extraction was reported as 94% with 1.25% (v/v) A327H$^+$Cl$^-$ from 7 M hydrochloric acid. From temperature variation study he found that extraction of In(III) was decreased with rise in temperature indicating exothermic extraction process.

There are some ionic liquids which can extract metal ion as well as hydrogen ions [11]. The pH value affects the metal and the hydrogen ion transfer process during the extraction of metal ions with ionic liquid. Separation of Ga(III) from In(III) was examined using ALi-CY, ALi-PC and ALi-D2 from HCl medium by Song et al. [12]. As scrutinized by them, at an initial pH of 4.2, percentages of extraction of Ga(III) and In(III) using ionic liquid Ali-D2 were less than those with Ali-CY and Ali-PC and equilibrium pH was increased in the order, ALi-CY > ALi-PC > ALi-D2. They concluded that ALi-PC could not completely separate the metal ions.

The generalized mechanistic pathways for the extraction of trivalent metal ion (Ga/In) and hydrogen ion using ionic liquid (R$_4$NA) are described as follows:

$$M^{3+}_{aq} + 3Cl^-_{aq} + 3R_4NA_{org} \leftrightarrow MA_{3_{org}} + 3R_4NCl_{org} \qquad (1)$$

$$R_4NA_{org} + H^+_{aq} + Cl^-_{aq} \leftrightarrow R_4NCl \cdot HA_{org} \qquad (2)$$

Here, 'A' and 'R' represent the anionic part of organophosphorus acids and alkyl group of Aliquat 336, respectively. From the loaded IL organic phase stripping was done using HCl and $H_2SO_4$, which followed the mechanism proposed in the reported work:

$$MA_{3_{org}} + 3H^+_{aq} \leftrightarrow M^{3+}_{aq} + 3HA_{org} \qquad (3)$$
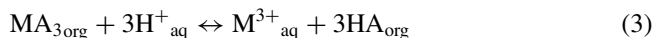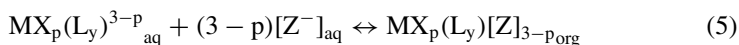
The quaternary ammonium iodide salt, [MTOA][I], behaves as a reducing agent as well as an extracting agent which selectively separates Ga(III) from Fe(III) in one stage from HCl (1–4 M) by transferring tetrachlorogallate, $[GaCl_4]^-$ through ion pair formation as reported by Kinsman et al. [13]. Stripping of Ga(III) from organic extract was efficiently achieved by using water. They also carried out regeneration of extractant successfully with the help of aqueous KI and mild reducing agent, $Na_2S_2O_3$.

## 2.2 Using Functionalized Ionic Liquids

Volia and group [14] have investigated the extraction profile of indium and thallium from the aqueous HCl medium using the [Hbet][$Tf_2N$] ionic liquid. The cationic part of the above ionic liquid contains functionalized carboxylic group having the capacity of forming bonds with the metal ion. They reported that accumulation of the extractant (zwitter ionic betaine) accelerates the extraction efficiency of the metal ions. In(III) extraction was found to rise with an increase in [$Tf_2N^-$] concentration. Based on the experimental observations, Volia et al. proposed that ion pair formation followed by ion exchange mechanisms are responsible for metal extraction. At higher concentration of HCl, addition of betaine to the aqueous phase, led to the extraction of indium as positively charged dichloride complexes ($InCl_2^+$). The mechanism involving functionalized ionic liquids can be expressed as follows:

$$MX_p^{3-p}{}_{aq} + y[HL^+]_{aq} \leftrightarrow MX_p(L_y)^{3-p}{}_{aq} + y(H^+)_{aq} \qquad (4)$$

$$MX_p(L_y)^{3-p}{}_{aq} + (3-p)[Z^-]_{aq} \leftrightarrow MX_p(L_y)[Z]_{3-p_{org}} \qquad (5)$$
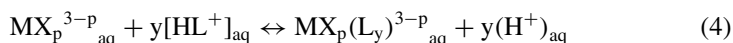
where M is the trivalent metal, $HL^+Z^-$ is the functionalized ionic liquid.

The extraction of In(III) from H[TFSA] aqueous solution using 1 M TBP diluted with [N1116][TFSA] has been undertaken by Matsumiya et al. [15]. Extraction followed solvation and cation exchange profile. The extracted complex was proposed

as [In(TBP)$_3$$^{3+}$(TFSA$^-$)$_3$] based on slope analysis results. Low pH value favors the extraction percentage of In(III). Indium was recovered by electrodeposition from the organic extract.

## 2.3   With Diverse ILs

Katsuta et al. [16] have studied the extraction of Al(III), Ga(III) and In(III) from HCl medium employing a combination of [TOAH][NTf$_2$] and [TOAH][NO$_3$], two protic ionic liquids. The extraction of Ga(III) increases following the order: [TOAH][NTf$_2$] = [B$_{MIm}$][NTf$_2$] < [MTOA][NTf$_2$] (Fig. 2). Ga(III) extraction was not sufficient when [TOAH][NTf$_2$] was extractant whereas adding [TOAH][NO$_3$] to the organic phase enhances the percentage of extraction which may be due to anion exchange between [GaCl$_4$]$^-$ and nitrate ion. The hydrophobic nature of [NTf$_2$]$^-$ could not make the anion exchange process easier. The authors also reported the separation of Ga(III) and In(III) as displayed in Fig. 3.

Deferm et al. [17] have studied the separation of indium(III) and zinc(II) from non aqueous ethylene glycol phase was investigated by using phosphonium based



**Fig. 2** Plot of % E versus types of ILs for Ga(III) extraction [16]
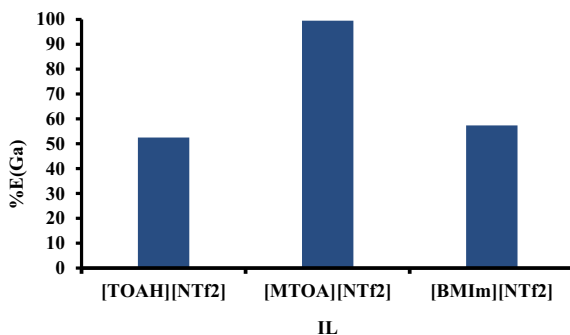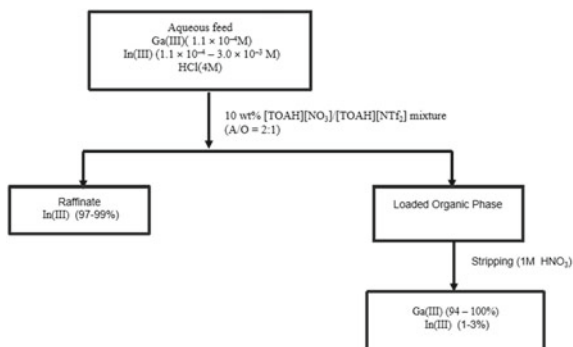


**Fig. 3** Process flow sheet for separation of Ga(III) and In(III) using ionic liquid mixture [16]

IL Cyphos IL 101 and ammonium ionic liquid Aliquat 336 in p-cymene. Bridging $(InCl_3)_2(EG)_3$ or mononuclear $(InCl_3)(EG)_2$ complexes have been suggested at low LiCl concentrations while at higher LiCl molarity, $[In(EG)Cl_4]$ was formed. The percentage of extraction of In(III) and Zn(II) increased with enhancing Cyphos IL 101 concentration. About 99% of indium(III) and 90% of zinc(II) have been extracted. Maximum separation factor of 6 was achieved using 2.56 vol.% Cyphos IL 101. Extraction isotherm showed that quantitative extraction of In(III) was achieved using four counter-current stages. Effective stripping of 98.5% was obtained with NaOH solution. Deferm et al. [18] have scrutinized the extraction of indium from a chloride solution with the use of ionic liquids Cyphos 101 and Aliquat 336. Extraction efficiency of 95% was obtained with 0.5–12 M HCl in the feed phase. Indium was recovered as hydroxide in precipitate form. The separation of In(III) from associated metal ions like Cd(II), Cu(II), Fe(III), Mn(II), Ni(II), Sn(IV) and Zn(II) which occur in the industrial waste has also been carried out by the group. Nayak and Devi [19] have reported the solvent extraction of Ga(III) from acidic chloride medium using Cyphos IL 101 in kerosene. The extraction was maximum with 2 M HCl. They proposed that $GaCl_4^-$ is the extracted metal ion species. Stripping was above 90% with 0.1 M HCl.

There are few reports on the extraction of gallium and indium from different resources using ionic liquids which have been summarized in Table 3.

**Table 3** Tabular representation of extraction studies of Ga and In from various resources using ILs

| Source | Organic phase | Extraction results | References |
|---|---|---|---|
| Gallium, indium and arsenic in semiconductors | $[P_{44410}][Br_3]$ in n-dodecane | As(95%), Ga(96%), In(99%) | [20] |
| Indium from iron-rich solutions | [A336][Cl] | Separation factor of 5400 was obtained for In/Fe | [21] |
| Indium from waste LCDs | [Hbet][Tf$_2$N] | Leaching rate = 99.75% and indium extraction rate = 98.63% | [22] |
| Gallium from spent Bayer process liquor | Kelex100 dissolved in $[EhEhT_{23}]_2[SO_4]$/ $[HHT_{12}][Tf_2N]$ | Separation factor of Ga/Al = 1000 with $[HHT_{12}][Tf_2N]$ Separation factor of Ga/Al = 20 with $[EhEhT_{23}]_2[SO_4]$ | [23] |
| Gallium and iron in chloride medium | [MTOA][I] | Selectively separation of Ga(III) from Fe(III) in a single step from 1 to 4 M HCl | [24] |

# 3 Conclusions

Solvent extraction is a simpler, chemically stable and reliable technique commonly adopted to recover Ga and In from various potential resources. Ionic liquids are the future extractants that substantially can be used for the quantitative retrieval as well as separation of Ga and In. The process optimization, selectivity and regeneration studies are the parameters to be looked upon in detail to make the best use of these designer solvents. Use of ammonium based ionic liquids for the separation of Ga(III) and In(III) have been reported in more detail as compared to other ionic liquids. The extraction of gallium and indium from industrial wastes requires more investigation using these green extractants. The recovery of these metals from post-consumer products is not very easy. The reason for this is that the contents of these valuables are very low in the post-consumer products. There is an urgent need for the development of novel and low carbon recycling path which may ensure to meet the upcoming demand of gallium and indium.

# References

1. Horváth IT, Anastas PT (2007) Introduction: green chemistry. Chem Rev 107(6):2167–2168
2. McDaniel JG, Yethiraj A (2019) Understanding the properties of ionic liquids: electrostatics, structure factors, and their sum rules. J Phys Chem B 123(16):3499–3512
3. Bonhôte P, Dias A-P, Papageorgiou N, Kalyanasundaram K, Grätzel M (1996) Hydrophobic, highly conductive ambient-temperature molten salts. Inorg Chem 35:1168–1178
4. Ngo HL, LeCompte K, Hargens L, McEwen AB (2000) Thermal properties of imidazolium ionic liquids. Thermochim Acta 357–358:97–102
5. McEwen AB, Ngo HL, LeCompte K, Goldman JL (1999) Electrochemical properties of imidazolium salt electrolytes for electrochemical capacitor applications. J Electrochem Soc 146(5):1687
6. Sharafi Z, Hosseini SM, Jahromi LD (2012) Modified equation of state extended to imidazolium-, phosphonium-, pyridinium-, pyrrolidinium-and ammonium-based ionic liquids. Ionics 18(9):829–835
7. Derhnavi PY (2013) Global cycle of gallium production, use and potential recycling. Land Water Resour Eng
8. Gunn G (2014) Critical metals handbook, 1st edn. Wiley, Chichester, UK
9. Alguacil FJ, Escudero E (2019) Solvent extraction of Indium(III) from HCl solutions by the ionic liquid (A324H$^+$)(Cl$^-$) dissolved in Solvesso 100. Hydrometallurgy 189:105104
10. Alguacil FJ (2020) Liquid-liquid extraction of Indium(III) from the HCl medium by ionic liquid A327H$^+$Cl$^-$ and its use in a supported liquid membrane system. Molecules 25(22):5238
11. Le MN, Son SH, Lee MS (2019) Extraction behavior of hydrogen ion by an ionic liquid mixture of Aliquat 336 and Cyanex 272 in chloride solution. Korean J Metals Mater 57(3):162–169
12. Song SJ, Le MN, Lee MS (2020) Separation of Gallium(III) and Indium(III) by solvent extraction with ionic liquids from hydrochloric acid solution. Processes 8(11):1347

13. Kinsman LMM, Morrison CA, Ngwenya BT, Love JB (2020) Reducing the competition: a dual purpose ionic liquid for the extraction of gallium from iron chloride solutions. Molecules 25(18):4047
14. Volia MF, Tereshatov EE, Boltoeva M, Folden CM (2020) Indium and thallium extraction into betainium bis (trifluoromethylsulfonyl) imide ionic liquid from aqueous hydrochloric acid media. New J Chem 44:2527–2537
15. Matsumiya M, Sumi M, Uchino Y, Yanagi I (2018) Recovery of indium based on the combined methods of ionic liquid extraction and electrodeposition. Sep Purif Technol 201:25–29
16. Katsuta S, Okai M, Yoshimoto Y, Kudo Y (2012) Extraction of gallium(III) from hydrochloric acid solutions by trioctylammonium-based mixed ionic liquids. Anal Sci 28(10):1009–1012
17. Deferm C, Onghena B, Tu Nguyen V, Banerjee D, Fransaer J, Binnemans K (2020) Non-aqueous solvent extraction of indium from an ethylene glycol feed solution by the ionic liquid Cyphos IL 101: speciation study and continuous counter-current process in mixer–settlers. RSC Adv 10:24595
18. Deferm C, Van de Voorde M, Luyten J, Oosterhof H, Fransaer J, Binnemans K (2016) Purification of indium by solvent extraction with undiluted ionic liquids. Green Chem 18(14):4116–4127
19. Nayak S, Devi N (2017) Separation and recovery of gallium (III) ions from aqueous phase by liquid–liquid extraction using a novel extractant, Cyphos IL 101. Turk J Chem 41(6):892–903
20. Van den Bossche A, Vereycken W, Vander Hoogerstraete T, Dehaen W, Binnemans K (2019) Recovery of gallium, indium, and arsenic from semiconductors using tribromide ionic liquids. ACS Sustain Chem Eng 7(17):14451–14459
21. Van Roosendael S, Regadío M, Roosen J, Binnemans K (2019) Selective recovery of indium from iron-rich solutions using an Aliquat 336 iodide supported ionic liquid phase (SILP). Sep Purif Technol 212:843–853
22. Luo D, Zhu N, Li Y, Cui J, Wu P, Wang J (2019) Simultaneous leaching and extraction of indium from waste LCDs with acidic ionic liquids. Hydrometallurgy 189:105146
23. Raiguel S, Dehaen W, Binnemans K (2020) Extraction of gallium from simulated Bayer process liquor by Kelex 100 dissolved in ionic liquids. Dalton Trans 49(11):3532–3544
24. Kinsman MML, Morrison AC, Ngwenya TB, Love BJ (2020) Reducing the competition: a dual-purpose ionic liquid for the extraction of gallium from iron chloride solutions. Molecules (Basel, Switzerland) 25(18):4047. https://doi.org/10.3390/molecules25184047

# Multi Parametric Investigation for Improvement in Machining Characteristics on Aluminium Boron Carbide Composite in WEDM

**Nitin Kumar Sahu** [ID]**, Mukesh Kumar Singh** [ID]**, Atul Kumar Sahu** [ID]**, and Anoop Kumar Sahu** [ID]

**Abstract** In current manufacturing scenario, highly complex and specific objects are to be manufactured from advanced materials for various important fields of engineering like missile, space research, nuclear industry, etc. These advanced innovative materials such as super alloys, ceramics and composites are difficult to be processed by conventional machining operations. Wire Electric Discharge Machining (WEDM) has been accepted as a standard process for conductive metals from the viewpoint of economic production and is capable to generate complex geometrical shapes in hard materials/components. In the present study, investigation of machinability on Aluminium boron carbide (Al–$B_4C$) composite is performed which is having outstanding mechanical and thermal properties at eminent temperatures and also having broad application in imperative engineering fields. The authors considered various important WEDM input parameters i.e. Wire Tension ($W_t$), Wire Diameter ($W_d$), Wire Material ($W_m$), and Peak current ($I_p$) with Taguchi $L_9$ orthogonal array for optimizing output responses i.e. Material Removal Rate (MRR) and Surface Roughness (SR) in multi objective optimization realm. The authors have robustly applied computational Taguchi based TOPSIS (T-TOPSIS) in order to model the multi dimensional machinability. Validation tests were carried out and showa closer relationship with the experimental results. It is found that optimal process parameters setting is $W_{t3}W_{d1}W_{m1}I_{p1}$ for simultaneously maximizing MRR and minimizing SR.

**Keywords** Wire electrical discharge machining (WEDM) · Taguchi · Orthogonal array · Multi criteria decision making (MCDM) · Technique for order preference by similarity to ideal solution (TOPSIS)

N. K. Sahu (✉) · M. K. Singh · A. K. Sahu
Department of Industrial and Production Engineering, Guru Ghasidas (Central) Vishwavidyalaya, 495009, Bilaspur, Chhattisgarh, India
e-mail: nitin83sahu@gmail.com

A. K. Sahu
Department of Mechanical Engineering, Guru Ghasidas (Central) Vishwavidyalaya, 495009, Bilaspur, Chhattisgarh, India

81

# 1 Introduction

Now a days, every manufacturing organization is trying to implement sustainable practices in manufacturing their product, which can provide significant impacts in attaining manufacturing outputs in the long run [1, 2]. The current manufacturing scenario of producing high precision mechanical engineering components plays a key role for gaining competitive advantage. Recent developments in the field of advanced composite materials and alloys have created the necessity to develop efficient cutting processes which can carefully and easily machine those materials. Manufacturing organizations are seeking influential practices that may assist them to shift from traditional manufacturing to modern manufacturing for gaining competitive advantage in regards to product quality, productivity, economy etc. [3, 4]. For sustainable growth, non-conventional machining is gaining importance for machining hard, brittle and tough materials which are difficult to machine by conventional machining process as it uses directly applied force for metal removal from work piece. Non-conventional machining operations are employed when the shape of the job is too complex and difficult to machine by conventional machine. WEDM is a non-conventional machining process and is able to generate complex shapes and cuts extremely hard, exigent and unusual materials to very close tolerances. WEDM process provides high accuracy and is applicable for any conductive material. The fundamental principle in WEDM is the transformation of electrical energy into thermal energy through a series of discrete electrical spark which can be used for erosion of unwanted material in order to produce the desired shape. WEDM operation utilizes high voltage across the narrow gap between the electrode and the work piece in which dielectric is continuously circulated. As there is no direct contact between the tool and work piece, the hardness of the material is no longer a dominating factor for WEDM process. Moreover, it is keenly necessary to identify effective working conditions for machining components to result in less energy consumption, enhance productivity, reduce machining time etc. it is found that proper selection of process parametric setting enables the WEDM to produce components with better operational efficiency, proper utilization of resources and reduction in wastes [5, 6]. Thus, there is a prime requirement to carry out research work to provide strategic solution to the industrial engineers & managers for sustainable development and societal growth.

# 2 State of Art

In past decades, various researches have been carried out in investigating the different domains of WEDM. Eckman & Williams [7] derived an algorithm in a low-current electrical discharge which was begun by low-voltage spark over between plane electrodes immersed in a liquid dielectric for analyzing their physical conditions. Jeswani [8], Ming and He [9] investigated the impact of variation made in dielectric and found that the addition of fine graphite powder in kerosene significantly affects the metal

removal rate and the tool wear rate. Dielectric plays an important role between the gaps as it flushes the unwanted metal. Wong et al. [10] studied the effect of addition of fine powder into dielectric fluid as a suspension between the gap of tool and work piece during machining for investigating the behavior of mirror finish on work piece. Type of dielectric that flows between the job and tool should be of prime importance as it has a great relationship with the characteristics of the recast layer. The spark that generates during machining causes the erosion in form of molten metal from the work piece and if flushing pressure is not adequate, this molten metal tends to re-solidifies speedily and forms the recast layer at the machined surface of the work piece [11]. WEDM has become a potentially important process with the demands of minimization of surface roughness, high precision and accurate geometric dimensions [12]. In recent years, many researchers are frequently utilizing intelligent approaches such as gray relational analysis, genetic algorithm and artificial neural network for process modeling and to determine the optimal process parameters [13–17].

Manufacturing plays a very significant role in effectually satisfying the dynamic needs of the customers [18, 19]. Jena and Das [20] considered the input parameters such as discharge current, pulse duration and duty cycle and has tried to predict material removal rate through back-propagation neural network (BPN) and radial basis function neural network (RBFN) for AISI D2 steel work piece. Singh et al. [21] selected discharge current, pulse on time, duty cycle, electrode rotation and discharge gas pressure as process factors and proposed mathematical models for the prediction of material removal rate and surface roughness of helium-assisted electrical discharge machining of D3 die steel based on artificial neural network with back-propagation algorithm, adaptive neuro fuzzy inference system (ANFIS) and response surface methodology. Lin et al. [22] utilized gray neural network for reflecting the process characteristics of the machine. Prakash et al. [23] investigated the Hybrid Composites (Al-Si12/B4C/Fly Ash) in WEDM to identify the effect of WEDM process parameters on the material removal rate (MRR) & surface roughness (SR) responses and found that the MRR can be increased by increase in pulse on time & reinforcement. It is also found that an increase in gap voltage, pulse on time, pulse off time, wire feed and reinforcement, increases the SR. Perumal et al. [24] examined the effect of pulse on duration, wire tension, and wire feed on MRR and SR while performing machining of Ti-6Al-2Sn-4Zr-2Mo (α-β) Alloy using Gray Relational Approach in WEDM, where significant thrust has been received by the authors to review the process parameters for sustainable outcomes. Nixon and Ravindra [25] investigated the parametric influence and optimum process parameters of Wire-EDM using Taguchi's technique with Taguchi's $L_{16}$ Orthogonal Array (OA) and a Genetic algorithm in Wire-cut Electro Discharge Machining (WEDM).

The manufacturing, machine tools and its related domain should be optimized for receiving elevated results [26–28]. WEDM output responses performance characteristics are highly influenced by the input parameters [29, 30]. Hence, it is extremely significant to attain better performance characteristics by finding the optimum values of process parameters and contribution of each parameter [31]. Taguchi method is a powerful tool that can be utilized to judge the optimal conditions in several manufacturing fields [32, 33]. Multiple response characteristics Optimization is more

complicated as compared to single performance characteristics optimization [34]. Here, combined effect of input parameters on Experimental results for measuring responses makes this study as a multiple response characteristics Optimization [35, 36]. Decision analysis is apprehensive and depends on the condition in which a decision maker has to select the best among several substitutes keeping in view the target output [37]. The aim of the study is to provide decision making provisions to the current manufacturing organization, which helps and supports them in identifying efficient working conditions to enhance profitability and productivity during machining. The selection of proper machining condition against desired output is prominent to meet the demand of current fast growing markets that demand high quality product in less lead time. Proper selection of process parametric setting enables sustainable performance marks to the work piece machined on the WEDM. The present study can be used by the manufacturing organization to decide significant levels of process parameters in order to take advantage of better operational efficiencies. The presented study fused Multi criteria decision making technique with Taguchi design methodologies to evaluate multiple response parameters in WEDM. In the present study, TOPSIS Methodology is fruitfully applied to investigate the experimental objectives in order to optimize the combined performance of output responses.

## 3 Material and Methodology

Technologically developed industries such as aeronautics, missiles, automobiles, nuclear reactors, armed turbines etc. requires rigorous materials which will provide high strength to wear ratio, good stiffness, low weight, high wear resistance, superior electrical and thermal properties, corrosion resistance, toughness, and other diverse properties. In this regard, development and utilization of various advanced materials are continuously increasing in place of existing used materials to attain competitive advantages. Also, such materials are also difficult to machines due to their intricate shape and complex geometries by conventional machining methods. In this study, Aluminium boron carbide composite is considered as a work piece material in Wire Cut Electrical Discharge Machining. Taguchi's design methodology is fruitfully utilized due to its simplicity in optimizing the process variables. Here, Taguchi $L_9$ orthogonal array is applied to provide the desired information within minimum number of trials with different number of levels in evaluating output response. In the present study, Multi objective optimization is carried out simultaneously under multiple independent process parameters using Taguchi based TOPSIS methodology. The efficacy and accuracy of TOPSIS methodology have been confirmed by various authors in converting the multi objective optimizations into single objective optimization [38, 39]. The following are the procedural steps:

*Step 1*: Normalization and formulation of decision matrix; $X = (x_{ij})_{mn}$ by using Eq. 1:

$$r_{ij} = \frac{X_{ij}}{\sqrt{\sum_{j=1}^{n} X_{ij}^2}}, i = 1, 2, 3, \ldots \ldots \ldots m; j = 1, 2, 3, \ldots \ldots \ldots n \quad (1)$$

Here $r_{ij}$ is the normalized criterion rating.

*Step 2*: Formulation of the weighted normalized decision matrix $v = (v_{ij})_{mn}$ by incorporating respective weight; $w_j$ of the $j^{th}$ measure such that $\sum_{j=1}^{n} w_j = 1$.

*Step 3*: Identification of Positive Ideal Solution (PIS) and Negative Ideal Solution (NIS) from the weighted normalized decision matrix by exploring Eqs. 2 and 3.

$$A^* = \{v_1^*, \ldots \ldots \ldots \ldots, v_n^*\} = \{\max v_{ij}(j \in \Omega_b), \min v_{ij}(j \in \Omega_c)\} \quad (2)$$

$$A^- = \{v_1^-, \ldots \ldots \ldots \ldots, v_n^-\} = \{\min v_{ij}(j \in \Omega_b), \max v_{ij}(j \in \Omega_c)\} \quad (3)$$

where; $\Omega_b$ and $\Omega_c$ reacts towards the sets of beneficial measures and cost measures, respectively.

*Step 4*: Determine the Euclidean distances for each alternative from PIS and NIS by adopting Eqs. 4 and 5 respectively.

$$D_i^* = \sqrt{\sum_{j=1}^{n} (v_{ij} - v^*)_{ij}^2}, i = 1, 2, 3, \ldots \ldots m \quad (4)$$

$$D_i^* = \sqrt{\sum_{j=1}^{n} (v_{ij} - v^*)_{ij}^2}, i = 1, 2, 3, \ldots \ldots m \quad (5)$$

*Step 5*: Estimation of relative closeness coefficient for each alternative by adopting Eq. 6, where the best alternative responded towards the utmost relative closeness coefficient from the ideal solution.

$$RC_i = \frac{D_i^-}{D_i^* + D_i^-}, i = 1, 2, 3, \ldots \ldots \ldots m \quad (6)$$

## 4 Experimentation, Results and Discussion

Currently, the world is moving towards sustainable manufacturing as it leads in imparting efficiency, quality, profitability etc. Today, novel materials are continuously evolving and utilizing in critical engineering applications. Today, it is required to focus on advanced manufacturing practices that may process critical material with enhanced machinability. The efficient machining of these materials is indeed

necessary and should be properly analyzed as a wide parametric range is indulged in the machining process. It is found that improper selection of process parameters results in reduced MRR, productivity and increase SR, cost, etc. Thus, it is required to analyze input process parametric setting for maintaining excellency in manufacturing and for reinforcing manufacturing companies with innovativeness and competitiveness. Hence, the present study focuses in identifying the WEDM process parametric setting, which can be utilized to optimize the MRR and SR. The study provides the guidance to the industrial engineers in regard to machining management, quality, productivity, economic analysis etc. In the present study, Modeling has been carried out by utilizing various independent process parameters i.e. Wire Tension, Wire Diameter, Wire Material and Peak current up to three different levels to optimize the performance of WEDM outputs as shown in Table 1. WEDM machine (Electronica-High-precision 5 axes CNC Ultima Series Flush) is utilized for experimentation purpose. Moreover, Taguchi L$_9$ orthogonal array is then applied to attain the desired information within minimum number of trials for evaluating output response. Material removal rate and surface roughness data is experimentally obtained by varying the inputs factors at three distinct levels as depicted in Table 2. Moreover, obtained experimental data is having different dimensional components and is required to transform into a comparable platform. Hence, normalization process is carried out using Eq. 1 to convert the various dimensions of data into dimensionless data as shown in Table 3.

Afterwards, the PIS and NIS are estimated by using Eqs. 2 and 3 for Multi objective responses by assessing the normalized values of MRR and SR. The PIS and NIS specify the best and worst attainable values of MRR and SR for the alternatives. The PIS facilitates in determining the ideal value for the experimental run that assists in maximization of MRR and minimization of SR. Moreover, NIS facilitates in determining the ideal value for the experimental run that assists in minimization of MRR and maximization of SR. The PIS and NIS data for each of the output responses assisted in evaluating the Multi Parameter Performance Indicator (MPPI). Equations 4–6 is employed for estimating the MPPI as depicted in Table 4. MPPI assists in modeling the Multi Objective Optimization into single Objective Optimization. SR of the machined surface was measured by SJ−210 surface roughness Tester (Make: Mitutoyo, Model: 178–561−02A). Material removal rate of the EDMed work material is estimated based on the weight of material removed per unit time. If, $W_i$ and $W_f$ are the initial and final weight of work piece and $M_t$ is the machining time,

**Table 1** Bounded process parameters

| Parameters | Notations | Units | Level of variations | | |
|---|---|---|---|---|---|
| | | | 1 | 2 | 3 |
| Wire tension | (W$_t$) | Kgf | 4 | 7 | 10 |
| Wire diameter | (W$_d$) | mm | 0.2 | 0.25 | 0.3 |
| Wire material | (W$_m$) | – | Copper | Brass | Molybdenum |
| Peak current | (Ip) | amp | 100 | 150 | 200 |

**Table 2** Response experimental data

| Taguchi L₉ orthogonal array | | | | | Response experimental data | |
|---|---|---|---|---|---|---|
| Exp no | Wire tension (Wt) | Wire diameter (Wd) | Wire material (Wm) | Peak current (Ip) | Material removal rate (MRR) (mg/min) | Surface roughness (SR) (mm) |
| $\delta_1$ | 1 | 1 | 1 | 1 | 64.235 | 3.275 |
| $\delta_2$ | 1 | 2 | 2 | 2 | 57.248 | 2.846 |
| $\delta_3$ | 1 | 3 | 3 | 3 | 60.254 | 2.658 |
| $\delta_4$ | 2 | 1 | 2 | 3 | 90.235 | 3.548 |
| $\delta_5$ | 2 | 2 | 3 | 1 | 85.949 | 2.564 |
| $\delta_6$ | 2 | 3 | 1 | 2 | 82.364 | 3.832 |
| $\delta_7$ | 3 | 1 | 3 | 2 | 88.257 | 2.978 |
| $\delta_8$ | 3 | 2 | 1 | 3 | 107.354 | 3.654 |
| $\delta_9$ | 3 | 3 | 2 | 1 | 93.875 | 2.456 |

**Table 3** Normalized tool wear rate, material removal rate and overall SCD of the responses for TOPSIS

| Exp no | Material removal rate (MRR) | Surface roughness (SR) |
|---|---|---|
| | Max | Min |
| $\delta_1$ | 16.642 | 1.143 |
| $\delta_2$ | 13.218 | 0.863 |
| $\delta_3$ | 14.643 | 0.753 |
| $\delta_4$ | 32.840 | 1.342 |
| $\delta_5$ | 29.794 | 0.701 |
| $\delta_6$ | 27.361 | 1.565 |
| $\delta_7$ | 31.416 | 0.945 |
| $\delta_8$ | 46.483 | 1.423 |
| $\delta_9$ | 35.543 | 0.643 |

then, MRR can be calculated from Eq. 7.

$$MRR(mg/min) = \left( \frac{W_i - W_f}{M_t} \right) \tag{7}$$

It is found that the most preferable process condition for optimizing output responses is $W_{t3} W_{d1} W_{m1} I_{p1}$ as shown in Fig. 1. Residual plot for MPPI is observed in order to assess the efficacy of the model as shown in Fig. 2, where the histogram does

**Table 4** Distance from PIS & NIS, signal to noise ratios (S/N ratios) and multi parameter performance indicator $T_{MPPI}^{TOPSIS}$ for each of the responses

| Exp no | PIS | NIS | $T_{MPPI}^{TOPSIS}$ | S/N ratio (higher-the-better) |
|---|---|---|---|---|
| $\delta_1$ | 29.845 | 3.449 | 0.1036 | −19.69273 |
| $\delta_2$ | 33.265 | 0.702 | 0.0207 | −33.69497 |
| $\delta_3$ | 31.840 | 1.640 | 0.0490 | −26.19940 |
| $\delta_4$ | 13.660 | 19.623 | 0.5896 | −4.58924 |
| $\delta_5$ | 16.688 | 16.599 | 0.4987 | −6.04399 |
| $\delta_6$ | 19.144 | 14.143 | 0.4249 | −7.43484 |
| $\delta_7$ | 15.070 | 18.208 | 0.5472 | −5.23769 |
| $\delta_8$ | 0.780 | 33.265 | 0.9771 | −0.20141 |
| $\delta_9$ | 10.940 | 22.344 | 0.6713 | −3.46142 |

not show any outliers, but it is somewhat very little skewed over the right. However, the normal probability plot clearly indicates that the experimental data is following the normal distribution curve and showing an approximately linear pattern consistent with a normal distribution. In Fig. 2, it can be further analyzed that the Residual versus the fitted value plot is showing a random pattern, which suggests that the residual has a constant variance. Also, Residual versus order plot value clearly shows that the order in which data was collected has no random error of the time related effects. Moreover, Interaction plot for MPPI is also observed in order to identify the effect of individual independent process variables over another as shown in Fig. 3. Figure 3 is used to disclose pair wise comparison of the input process parameters and to highlight the strength of the relationship between machining parameters i.e. Wt, Wd, Wm and Ip, for optimizing MPPI. Afterwards, the mean response table for Multi Parametric Performance Indicator is analyzed as shown in Table 5. It reveals the most influential condition of process parameters that have the largest impact on the output response. Afterwards, ANOVA analysis is carried to identify the most significant process parameters that have the greatest influence on the output response as depicted in Table 6. It is found that the most significant process parameters is wire tension and second most significant process parameters is wire material. It is also observed that the impact of wire diameter in simultaneously optimizing MRR and SR is insignificant.
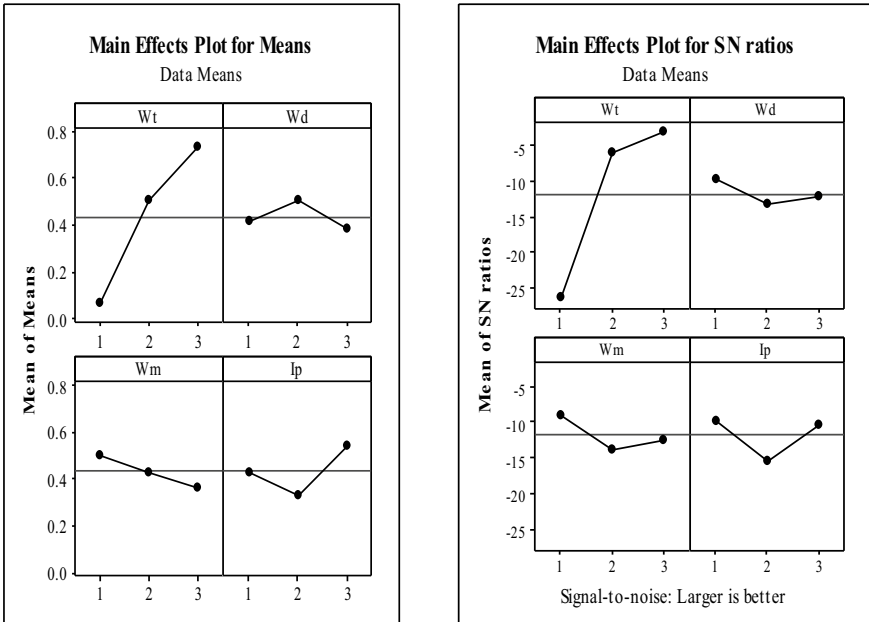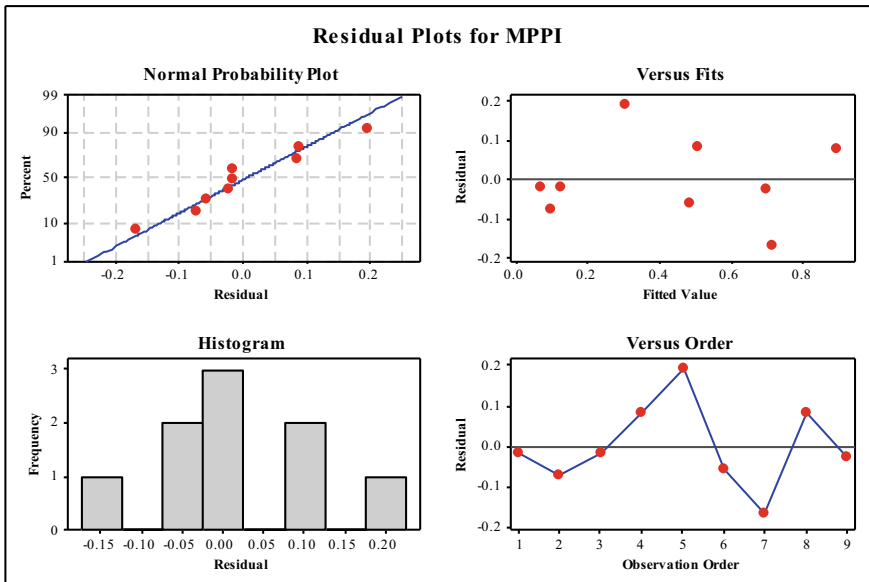
**Fig. 1**  Main effect plot and S/N ratios plot for MPPI
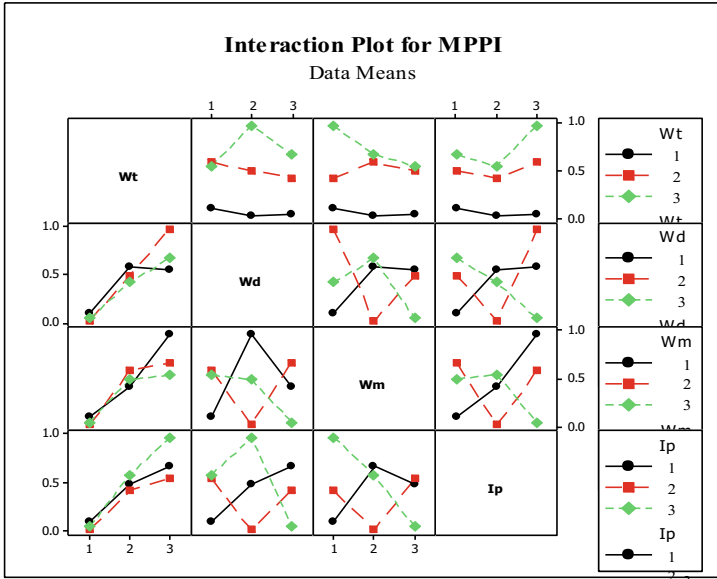


**Fig. 2**  Residual plot for MPPI

**Fig. 3** Interaction plot for MPPI

**Table 5** Response table (mean) for multi parametric performance indicator of $T^{TOPSIS}_{MPPI}$

| Factor | $T^{TOPSIS}_{MPPI}$ | | | |
|---|---|---|---|---|
| | Level 1 | Level 2 | Level 3 | Delta |
| Wire tension (Wt) | 0.05775 | 0.50437 | 0.73185 | 0.67410 |
| Wire diameter (Wd) | 0.41345 | 0.49880 | 0.38172 | 0.11708 |
| Wire material (Wm) | 0.50185 | 0.42719 | 0.36493 | 0.13692 |
| Peak current (Ip) | 0.42453 | 0.33090 | 0.53854 | 0.20764 |
| Total mean of $T^{TOPSIS}_{MPPI}$ = 0.4312 | | | | |
| Delta = Range i.e. Maximum–Minimum | | | | |

**Table 6** ANOVA for $T^{TOPSIS}_{MPPI}$ using adjusted SS for tests

| Source | DF | Sequential SS | Adj SS | Adj MS | F | P |
|---|---|---|---|---|---|---|
| Wire tension (Wt) | 1 | 0.68162 | 0.68162 | 0.68162 | 30.31 | 0.005 |
| Wire diameter (Wd) | 1 | 0.00151 | 0.00151 | 0.00151 | 0.07 | 0.808 |
| Wire material (Wm) | 1 | 0.02812 | 0.02812 | 0.02812 | 1.25 | 0.326 |
| Peak current (Ip) | 1 | 0.01950 | 0.01950 | 0.01950 | 0.87 | 0.404 |
| Error | 4 | 0.08996 | 0.08996 | 0.02249 | | |
| Total | 8 | 0.82071 | | | | |

## 5   Conclusion

In the presented research work, Aluminium boron carbide composite is considered as a work piece material in Wire Cut Electrical Discharge Machining to evaluate the optimal setting between considered input parameters i.e. Wire Tension ($W_t$), Wire Diameter ($W_d$), Wire Material ($W_m$), and Peak current (Ip) for achieving optimal output responses i.e. material removal rate (MRR) and surface roughness (SR). Taguchi $L_9$ orthogonal array design accompanied with TOPSIS Methodology has been fruitfully applied to convert multi-response optimization problem into an equivalent single objective optimization problem. It is found that optimal process parameters setting is $W_{t3}W_{d1}W_{m1}I_{p1}$ for simultaneously maximizing MRR and minimizing SR. The results clearly depict that the combination of independent process parameters i.e. $W_t$, $W_d$, $W_m$ and $I_p$ is found as 10, 0.2, copper and 100 for optimizing MRR and SR. It is also found that the Wire Tension (Wt) is the most significant parameter having p value as 0.05. The proposed Taguchi based TOPSIS Methodology is easy, uncomplicated and efficient in developing a strong, flexible and adaptable process in Wire Cut Electrical Discharge Machining to evaluate the optimal setting.

## References

1. Nas E, Özbek O, Bayraktar F, Kara F (2021) Experimental and statistical investigation of machinability of AISI D2 steel using electroerosion machining method in different machining parameters. Adv Mater Sci Eng 2021:1–17
2. Abed FN, Ramesh V, Jwaid MF, Agarwal N, Koundal D, Ibrahim AM (2022) Enhancement modelling based on electrical discharge machining successive discharges. Adv Mater Sci Eng 2022:1–7
3. Yunus M, Alsoufi MS (2021) Multiresponse particle swarm optimization of wire-electro-discharge machining parameters of nitinol alloys. Math Probl Eng 2021:1–12
4. Guo C, Sun S, Di S, Wei D (2020) Study of working medium performance by acoustic emission in EDM machining of Ti6Al4V. Adv Mater Sci Eng 2020:1–10
5. Jampana VNR, Rao PSVR, Sampathkumar A (2021) Experimental and thermal investigation on powder mixed EDM using FEM and artificial neural networks. Adv Mater Sci Eng 2021:1–12
6. Muni RN, Singh J, Kumar V, Sharma S, Sudhakara P, Aggarwal V, Rajkumar S (2022) Multiobjective optimization of EDM parameters for rice husk Ash/Cu/Mg-reinforced hybrid Al-0.7Fe-0.6Si-0.375Cr-0.25Zn metal matrix nanocomposites for engineering applications: fabrication and morphological analysis. J Nanomater 1–15
7. Eckman PK, Williams EM (1960) Plasma dynamics in an arc formed by low-voltage sparkover of a liquid dielectric. Appl Sci Res Sect B 8(1):299–320
8. Jeswani ML (1981) Effect of the addition of graphite powder to kerosene used as the dielectric fluid in electrical discharge machining. Wear 70(2):133–139
9. Ming QY, He LY (1995) Powder-suspension dielectric fluid for EDM. J Mater Process Technol 52(1):44–54
10. Wong YS, Lim LC, Rahuman I, Tee WM (1998) Near-mirror-finish phenomenon in EDM using powder-mixed dielectric. J Mater Process Technol 79(1–3):30–40
11. Klocke F, Lung D, Antonoglou G, Thomaidis D (2004) The effects of powder suspended dielectrics on the thermal influenced zone by electrodischarge machining with small discharge energies. J Mater Process Technol 149(1–3):191–197

12. Yan MT, Huang CW, Fang CC, Chang CX (2004) Development of a prototype micro-wire-EDM machine. J Mater Process Technol 149(1–3):99–105

13. Wang K, Gelgele HL, Wang Y, Yuan Q, Fang M (2003) A hybrid intelligent method for modeling the EDM process. Int J Mach Tools Manuf 43(10):995–999

14. Cao F, Zhang Q (2004) Neural network modelling and parameters optimization of increased explosive electrical discharge grinding (IEEDG) process for large area polycrystalline diamond. J Mater Process Technol 149(1–3):106–111

15. Joshi SN, Pande SS (2011) Intelligent process modeling and optimization of die-sinking electric discharge machining. Appl Soft Comput 11(2):2743–2755

16. Panda DK, Bhoi RK (2005) Artificial neural network prediction of material removal rate in electro discharge machining. Mater Manuf Processes 20(4):645–672

17. Jung JH, Kwon WT (2010) Optimization of EDM process for multiple performance characteristics using Taguchi method and grey relational analysis. J Mech Sci Technol 24(5):1083–1090

18. Sahu NK, Sahu AK, Sahu AK (2017) Optimization of weld bead geometry of MS plate (Grade: IS 2062) in the context of welding: a comparative analysis of GRA and PCA–Taguchi approaches. Indian Acad Sci 8(3):234–259

19. Sahu AK, Sahu NK, Sahu AK, Rajput MS, Narang HK (2019) T-SAW methodology for parametric evaluation of surface integrity aspects in AlMg3 (AA5754) alloy: comparison with T-TOPSIS methodology. Measurement 132:309–323

20. Jena AR, Das R (2017) A comparison of neural network architectures for the prediction of MRR in EDM. IOP Conf Ser: Mater Sci Eng 263(4):1–7

21. Singh NK, Singh Y, Kumar S, Sharma A (2019) Comparative study of statistical and soft computing-based predictive models for material removal rate and surface roughness during helium-assisted EDM of D3 die steel. SN Appl Sci 1(6):1–12

22. Lin Z, Liu Y, Zhang L (2012) Research of EDM (electrical discharge machining) process simulation based on grey neural network. Lect Notes Electr Eng (LNEE) 177:373–379

23. Prakash JU, Sivaprakasam P, Garip I, Juliyana SJ, Elias G, Kalusuraman G, Colak I (2021) Wire electrical discharge machining (WEDM) of hybrid composites (Al-Si12/B4C/Fly Ash). J Nanomater 2021:1–10

24. Perumal A, Kailasanathan C, Stalin B, Kumar SS, Rajkumar PR, Gangadharan T, Venkatesan G, Nagaprasad N, Dhinakaran V, Krishnaraj R (2022) Multiresponse optimization of wire electrical discharge machining parameters for Ti-6Al-2Sn-4Zr-2Mo (α-β) alloy using Taguchi-grey relational approach. Adv Mater Sci Eng 2022:1–13

25. Nixon K, Ravindra HV (2011) Arametric influence and optimization of wire EDM of hot die steel. Mach Sci Technol 15(1):47–75

26. Sahu AK, Sahu NK, Sahu AK (2014) Appraisal of CNC machine tool by integrated MULTI MOORA-IGVN circumstances: an empirical study. Int J Grey Syst: Theory Appl 4(1):104–123

27. Sahu AK, Sahu NK, Sahu AK (2016) Application of modified MULTI-MOORA for CNC machine tool evaluation in IVGTFNS environment: an empirical study. Int J Comput Aided Eng Technol 8(3):234–259

28. Sahu AK, Narang HK, Rajput MS, Sahu NK, Sahu AK (2018) Performance modeling and benchmarking of green supply chain management: an integrated fuzzy approach. Benchmarking: Int J 25(7):2248–2271

29. Muthuramalingam T, Babu LG, Sridharan K, Geethapriyan T, Srinivasan KP (2020) Multi-response optimization of WEDM process parameters of inconel 718 alloy using TGRA method. Lect Notes Netw Syst (LNNS) 104:487–492

30. Minh ND, Tai BT (2019) Study of the effects of process parameters on tool wear rate in electrical discharge machining by Taguchi method. Int J Trend Sci Res Dev 3(6):934–936

31. Lin YC, Yan BH, Huang FY (2001) Surface improvement using a combination of electrical discharge machining with ball burnish machining based on the Taguchi method. Intertnational J Adv Manuf Technol 18:673–682

32. Tzeng FY, Chen FU (2003) A simple approach for robust design of high speed electrical-discharge machining technology. Intertnational J Mach Tools Manuf 43(3):217–227

33. Nourbakhsh F, Rajurkar KP, Malshe AP, Cao J (2013) Wire electro-discharge machining of titanium alloy. Procedia CIRP 5(1):13–18

34. Singh PN, Raghukandan K, Pai BC (2004) Optimization by grey relational analysis of EDM parameters on machining Al-10%SiCP composites. J Mater Process Technol 155–156(1–3):1658–1661

35. Pattnaik SK, Priyadarshini M, Mahapatra KD, Mishra D, Panda S (2015) Multi objective optimization of EDM process parameters using fuzzy TOPSIS method. In: International conference on innovations in information, embedded and communication systems (ICIIECS). IEEE, Coimbatore, pp 1–5

36. Rao KM, Kumar DV, Shekar KC, Singaravel B (2021) Optimization of EDM process parameters using TOPSIS for machining AISI D2 steel material. Mater Today Proc 46:701–706

37. Kumar A, Rai RN (2020) Grey-Taguchi and TOPSIS-Taguchi-based optimisation of performance parameters of Spark EDM on heat-treated AA7050/5 B4C composite. J Inst Eng (India): Ser D 101:71–79

38. Raj SON, Prabhu S (2017) Analysis of multi objective optimisation using TOPSIS method in EDM process with CNT infused copper electrode. Int J Mach Mach Mater 19:76–94

39. Habib S (2009) Study of the parameters in electrical discharge machining through response surface methodology approach. Appl Math Model 33:4397–4407

# The Effect of Reinforcement Composition and Sintering Temperature on Microstructure and Properties of Al-SiC-Fly Ash Composite

**Priti Shikha Nanda, A. P. Samal, Renu Prava Dalai, and Dinesh Kumar Mishra**

**Abstract** Aluminium and its alloys are gaining more importance in different sectors such as aerospace, automobile, and construction industries due to their superior corrosion resistance, high strength to weight ratio, and high compressive strength. Despite this, it failed to achieve the required properties under high loading and temperature conditions. On the other hand, the reinforcement of different ceramic phases such as SiC, $Al_2O_3$, $SiO_2$, $TiO_2$, and CaO in the Al metal matrix can effectively improve the durability under the above-mentioned harsh conditions. Moreover, fly ash (FA) is well-known hugely available industrial waste material. So, the present objective of the study is to reinforce the SiC and FA in the Al metal matrix to prepare Al-SiC-FA hybrid composite followed by their microstructural evolution and mechanical properties evaluation under the variation in reinforcement composition and sintering temperature. The scanning electron micrographs confirm the significant advancement in interfacial bonding between the matrix and reinforcement phases with the increase in sintering temperature. Further, the micrographs also confirm that the reinforcement particles (FA and SiC) are uniformly dispersed in the Al matrix phase. The compressive strength, hardness, and density of the composite pellets are progressively increased with the increase in sintering temperature. However, the increase in FA content above 5% is accompanied by the decrease in compressive strength and hardness due to the significant rise in porosity level.

**Keywords** Composite · Reinforcement · FA · Compressive strength · Sintering temperature

P. S. Nanda · A. P. Samal · R. P. Dalai · D. K. Mishra (✉)
Department of Metallurgical and Materials Engineering, Veer Surendra Sai University of Technology, Burla 768018, India
e-mail: dkmishra_mme@vssut.ac.in; dinesh.vssut@gmail.com

# 1   Introduction

The reinforcement of SiC and fly ash (FA) in Al metal matrix composites (AMMCs) has been predominantly used in aerospace, military and automotive industries due to their enriched physical and mechanical properties such as high specific strength, low density, enhanced wear resistance along with low fabrication cost [1, 2]. However, due to the poor compressive strength (CS), wear resistance, hardness, and low tensile strength of Al, it has faced challenges in different sectors. These challenges have been overcome with the addition of secondary reinforcement [3, 4]. As per the reported literatures, there are various types of reinforcements such as SiC [5–8], $Al_2O_3$ [5–9], FA [10], TiC [11, 12], $B_4C$ [8, 12–14], graphite [13, 14], carbon nanotube [15], graphene [15, 16] and $TiB_2$ [17] have been incorporated earlier in Al matrix. The AMMCs reinforced with SiC show high hardness, superior wear resistance, excellent elastic modulus, high tensile strength, and exceptional thermal and chemical stability [18–21]. Boopathi et al. [22] have observed a significant reduction in the density of SiC, FA, and SiC-FA reinforced AMMCs as compared to unreinforced Al. A similar type of observation has been reported by Gnjidic et al. [23] for SiC reinforcement; Rao et al. [24] for FA reinforced composites. On the other hand, FA being an industrial waste material reduces the processing cost of AMMCs. Further, the addition of FA in the composite enhances the physical and mechanical properties for a wide range of applications in automotive and other industrial sectors [10, 22, 25, 26]. As per the authors' knowledge, few studies [10, 22, 27, 28] have been reported on the fabrication and characterisation of Al-SiC-FA composite so far using different processing routes. So, the objective of this paper is to synthesise Al-SiC-FA hybrid composite samples via powder metallurgy route by varying the sintering temperature and reinforcement composition. Further characterisation of Al-SiC-FA composite samples is carried out to explore the effect of reinforcement composition and sintering temperature on microstructure and mechanical properties.

# 2   Experimental Methodology

Fine Al powder particles are reinforced with SiC and FA powder particles of average particle size of 400 mesh to prepare AMMC mixtures of different reinforcement compositions. As received FA, has an average composition of 61% $SiO_2$, 27.5% $Al_2O_3$, 2.2% CaO, and other trace elements. For uniform distribution of reinforcement (SiC and FA) particles across the Al metal matrix, the AMMC powder mixtures are milled in planetary ball mill (Retsch PM 200) with a constant speed of 200 rpm for 1 h. During milling, the weight ratio of grinding media (WC balls) to powder has been taken as 3:1 in the presence of ethanol as a process controlling agent. With the help of a uniaxial hydraulic KBr press, the milled powder has been compacted at 1000 psi compaction pressure to prepare the composite pellets. Zinc stearate of around 3 gm is mixed with ~25 ml acetone to prepare the slurry out of it. Then the

slurry is uniformly applied to lubricate the die walls after each compaction so that the powder particles do not stick to the wall of the die and can be easily removed. After the formation of green compact, sintering is carried out inside the muffle furnace atmosphere at various temperatures varying from (470–540) °C for 1 h soaking. The microstructural observations and analysis have been done by using scanning electron microscope (SU3500, Hitachi High-Technologies Corporation). With the help of a universal hardness tester (251 VRSA, AFFRI), the Vickers hardness test has been conducted under 500 gm load with 10 s dwell time. The bulk density of the AMMCs has been computed by taking their corresponding weight and volume into consideration. The compression test of the AMMCs is performed using a universal testing machine (UTM) (UTE 20 HGFL) under a strain rate of $10^{-3}$ s$^{-1}$. For the compression test, the sample dimension is a diameter (D) of 13 mm and a height (h) of 10 mm.

## 3　Results and Discussions

### 3.1　Microstructural Analysis

The incorporation of SiC and FA as reinforcement in the aluminium matrix greatly imparts the microstructure and properties of the matrix phase. Further optimum addition of FA can optimise the properties with the reduction in production cost. On the other hand, an increase in sintering temperature significantly reduces the pores that lead to advancement in interfacial bonding between the reinforcement particles with the matrix phase. Figure 1 has depicted the scanning electron microscopy (SEM) micrographs of Al-15SiC-5FA and Al-12.5SiC-7.5FA composite pellets sintered at different temperatures varying from (470–540) °C. The SEM micrographs of the sintered AMMC pellets confirm the uniform distribution of reinforced particles in the Al metal matrix phase. Further, the improvement in interfacial bonding between the reinforcement (SiC and FA) particles and the Al matrix phase is also observed with an increase in sintering temperature. Figure 2 has represented the quantitative energy dispersive spectroscopy (EDS) elemental analysis of matrix (Al) and reinforcement (SiC and FA) phases. The presence of aluminium can be observed (refer to Fig. 2a) with 99.07 weight%. The presence of different oxides such as $SiO_2$, $Al_2O_3$, and CaO, can be observed as received FA from the EDS spectrum (refer to Fig. 2c).

　Figure 3 has shown the EDS analysis of sintered Al-15SiC-5FA composite specimens at different sintering temperatures varying from (470–540) °C. The EDS analysis confirmed the presence of SiC, $SiO_2$, $Al_2O_3$, and CaO along with pores. Further, the EDS analysis has confirmed that with an increase in sintering temperature, there is a significant reduction in pores and oxides. These findings are well supported by the results found in Fig. 1. Moreover, the porosity present in the composite specimens is mainly due to the formation of clusters and FA addition. The morphological study on aluminium, SiC, and FA suggests the shape of aluminium particles usually appears as cylindrical droplet-like shapes, whereas SiC particles appear as ellipsoidal
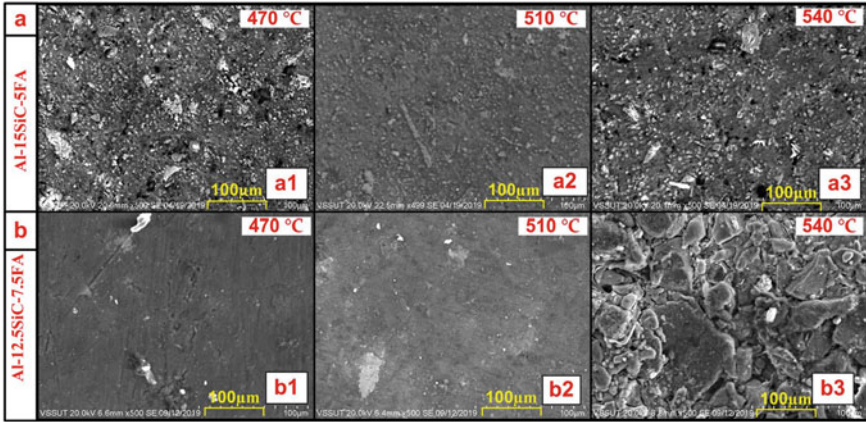
**Fig. 1** SEM micrographs of **a** Al-15SiC-5FA composite sintered at (a1) 470 °C, (a2) 510 °C (a3) 540 °C; **b** Al-12.5SiC-7.5FA composite sintered at (b1) 470 °C, (b2) 510 °C, (b3) 540 °C
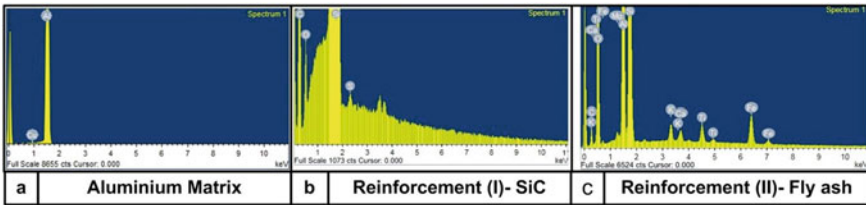


**Fig. 2** Quantitative EDS elemental analysis of **a** aluminium matrix, **b** reinforcement (I)—SiC, **c** reinforcement (II)—FA

geometry with pointed ends, and FA is observed with irregular hollow spherical solid particles. A similar type of observation is earlier reported by Shaikh et al. [28].

## 3.2 Hardness

Figure 4 has shown the computed Vickers hardness values of AMMC specimens with the variation in reinforcement composition at different sintering temperatures varying from (470–540) °C. The maximum hardness is found in the case of 80Al-20SiC AMMC specimen sintered at 540 °C, whereas the minimum for unsintered 80Al-12.5SiC-7.5FA composite specimen. The increase in hardness values of AMMCs with the increase in sintering temperature is primarily attributed to the development of interfacial bonding between the reinforcement (SiC and FA) phase and matrix (Al) phase, as discussed earlier in Figs. 1 and 3. The progressive increase in porosity level and cluster formation with the subsequent rise in FA content is mainly responsible for the declining trend of hardness values.
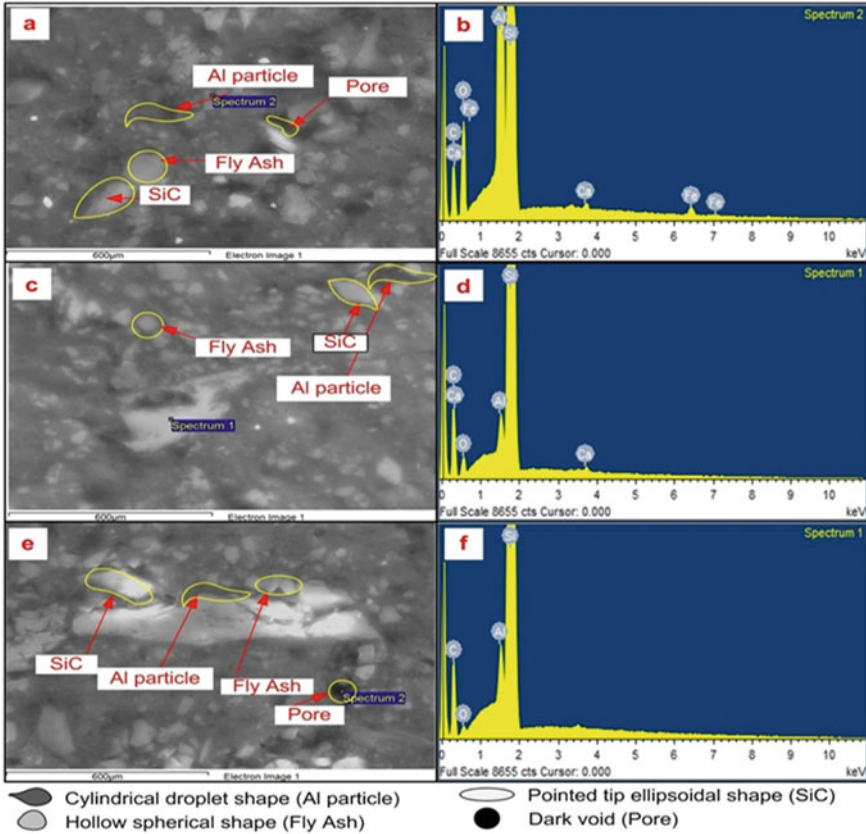
Fig. 3 EDS analysis of Al-15SiC-5FA composite specimens sintered at different sintering temperatures **a**, **b** 470 °C, **c**, **d** 510 °C, **e**, **f** 540 °C

Fig. 4 Hardness values of AMMC specimens with the variation in reinforcement composition at different sintering temperatures
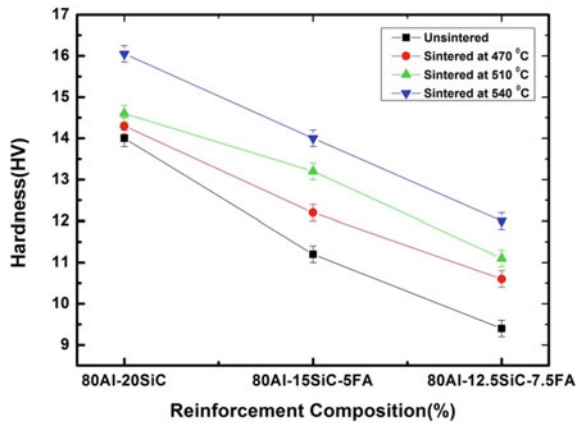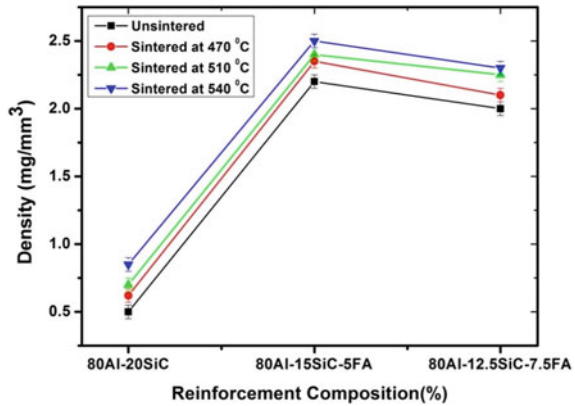
**Fig. 5** Density values of AMMC specimens with the variation in reinforcement composition at different sintering temperatures

## 3.3 Density

The bulk density (ρ) of the Al-SiC-FA composite pellets can be calculated as

$$\rho = 4M/\pi d^2 h \tag{1}$$

where M represents the weight of the pellet, $d$ and $h$ are the diameter and height of the cylindrical pellet respectively. Before sintering, the height and diameter of the pellets are approximately found to be 6 mm and 13 mm respectively, whose value further changes after sintering. Figure 5 shows the calculated bulk density values of AMMC specimens with the variation in reinforcement composition at different sintering temperatures varying from (470–540) °C. Density values have shown a similar trend for both sintered and unsintered samples. Initially, the density is increased by up to 5% of FA content. But, further, an increase in FA% causes a decrease in density of about (2–5) % due to the enormous FA content. Similar types of observation also have been reported earlier [29–32]. On the other hand, the bulk density has consistently increased with a significant rise in sintering temperature for all AMMCs (refer to Fig. 5) due to the considerable decline in porosity level.

## 3.4 Compressive Strength

Figure 6 has presented the CS plots of AMMC specimens with the variation in reinforcement composition at different sintering temperatures. The CS value has increased with the significant rise in sintering temperature due to the remarkable increase in green strength. However, the CS plots decreased gradually with the increase in FA content up to 5%. But, the further increase in FA content leads to cluster formation [33] that eventually causes a significant reduction in CS values.

**Fig. 6** CS values of AMMC specimens with the variation in reinforcement composition at different sintering temperatures
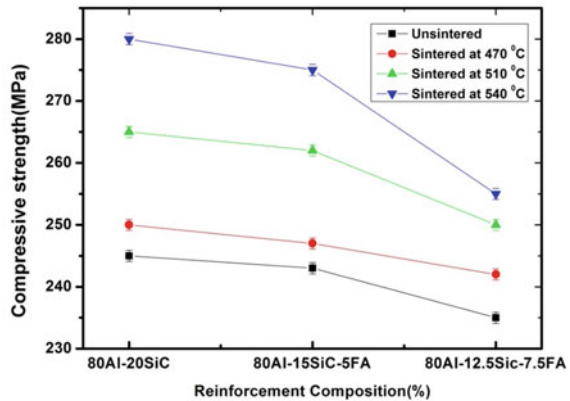


## 4 Conclusion

In the present study, the Al-SiC-FA hybrid composite samples have been fabricated by varying both the sintering temperature and reinforcement composition. Thereafter, the characterisation has been done to interpret the effect of reinforcement composition and sintering temperature variation over the advancement in microstructure and mechanical properties. The concluding remarks can be summarised, as the SEM and EDS analysis confirmed the significant reduction in porosity and oxide level with an increase in sintering temperature that subsequently enhanced the interfacial bonding between matrix (Al) and reinforcement phase (SiC and FA). Besides, the analysis also confirmed the uniform distribution of SiC and FA particles in the Al matrix. The Vickers hardness, bulk density, and CS values are progressively increased with an increment in sintering temperature. However, a prominent rise in porosity and cluster with the increase in FA content attributes to the progressively declining trend in hardness, and the CS values.

## References

1. Torralba JM, Da Costa CE, Velasco F (2003) P/M aluminium matrix composites: an overview. J Mater Process Technol 133(1–2):203–206
2. Dobrzanski LA, Wlodarczyk A, Adamiak M (2006) The structure and properties of PM composite materials based on EN AW-2124 aluminum alloy reinforced with the BN or $Al_2O_3$ ceramic particles. J Mater Process Technol 175(1–3):186–191
3. Anilkumar HC, Hebbar HS, Ravishankar KS (2011) Mechanical properties of fly ash reinforced aluminium alloy (Al6061) composites. Int J Mech Mater Eng 6(1):41–45
4. Sahin Y, Murphy S (1996) The effect of fibre orientation of the dry sliding wear of borsic-reinforced 2014 aluminium alloy. J Mater Sci 31(20):5399–5407
5. Unlu BS (2008) Investigation of tribological and mechanical properties $Al_2O_3$–SiC reinforced Al composites manufactured by casting or P/M method. Mater Des 29(10):2002–2008

6. Behera B, Dalai R, Mishra DK, Badjena SK (2020) Development and characterisation of $Al_2O_3$ and SiC reinforced Al-Cu metal matrix hybrid composites. Mater Sci Forum 978:202–208

7. Demir A, Altinkok N (2004) Effect of gas pressure infiltration on microstructure and bending strength of porous $Al_2O_3$/SiC-reinforced aluminium matrix composites. Compos Sci Technol 64(13–14):2067–2074

8. Shorowordi KM, Laoui T, Haseeb AA, Celis JP, Froyen L (2003) Microstructure and interface characteristics of B4C, SiC and $Al_2O_3$ reinforced Al matrix composites: a comparative study. J Mater Process Technol 142(3):738–743

9. Dalai R, Nath S, Mishra DK, Behera G (2020) Fabrication of an Al matrix hybrid composite reinforced with Cu, $Al_2O_3$ and TiC by mechanical alloying. Mater Today: Proceed 26:1841–1844

10. Ravesh SK, Garg TK (2012) Preparation & analysis for some mechanical property of aluminium based metal matrix composite reinforced with SiC & fly ash. Int J Eng Res Appl 2(6):727–731

11. Kennedy AR, Wyatt SM (2001) Characterising particle–matrix interfacial bonding in particulate Al–TiC MMCs produced by different methods. Compos A 32(3–4):555–559

12. Mazaheri Y, Meratian M, Emadi R, Najarian AR (2013) Comparison of microstructural and mechanical properties of Al–TiC, Al–B4C and Al–TiC–B4C composites prepared by casting techniques. Mater Sci Eng A 560:278–287

13. Baradeswaran A, Vettivel SC, Perumal AE, Selvakumar N, Issac RF (2014) Experimental investigation on mechanical behaviour, modelling and optimization of wear parameters of B4C and graphite reinforced aluminium hybrid composites. Mater Des 63:620–632

14. Thirumalai T, Subramanian R, Kumaran S, Dharmalingam S, Ramakrishnan SS (2014) Production and characterization of hybrid aluminum matrix composites reinforced with boron carbide ($B_4C$) and graphite. J Sci Ind Res 73:667–670

15. Li Z, Fan G, Guo Q, Li Z, Su Y, Zhang D (2015) Synergistic strengthening effect of graphene-carbon nanotube hybrid structure in aluminum matrix composites. Carbon 95:419–427

16. Wang J, Li Z, Fan G, Pan H, Chen Z, Zhang D (2012) Reinforcement with graphene nanosheets in aluminum matrix composites. Scr Mater 66(8):594–597

17. Lakshmi S, Lu L, Gupta M (1998) In situ preparation of $TiB_2$ reinforced Al based composites. J Mater Process Technol 73(1–3):160–166

18. Baker TN, Gorton AJ, Song Y, Ni X, Carvalho MH, Marcelo TM, Carvalhinhos H (1996) Powder processing of AA 6061 aluminium metal matrix composites using hot forging as means of consolidation. Powder Metall 39(3):223–229

19. Sagar R, Madan PK, Kumar M, Sachdeva S, Jain A (1992) Isostatic compaction of silicon carbide reinforced aluminum. Adv Powder Metall Part Mater 9:45–45

20. Umasankar V, Xavior MA, Karthikeyan S (2014) Experimental evaluation of the influence of processing parameters on the mechanical properties of SiC particle reinforced AA6061 aluminium alloy matrix composite by powder processing. J Alloys Compd 582:380–386

21. de Araujo ER, Alves SJF, Filho FA, Filho SLU, de Araujo Filho OO (2012) Processing and manufacturing of metal matrix aluminum alloys composites reinforced by silicon carbide and alumina through powder metallurgy techniques. Mater Sci Forum 727:254–258

22. Boopathi MM, Arulshri KP, Iyandurai N (2013) Evaluation of mechanical properties of aluminium alloy 2024 reinforced with silicon carbide and fly ash hybrid metal matrix composites. Am J Appl Sci 10(3):219–229

23. Gnjidic Z, Bozic D, Mitkov M (2001) The influence of SiC particles on the compressive properties of metal matrix composites. Mater Char 47(2):129–138

24. Rao JB, Rao DV, Bhargava NRMR (2010) Development of light weight ALFA composites. Int J Eng Sci Technol 2(11):50–59

25. Rohatgi PK, Murali N, Shetty HR, Chandrashekhar R (1976) Improved damping capacity and machinability of graphite particle-aluminum alloy composites. Mater Sci Eng 26(1):115–122

26. Kulkarni SG, Meghnani JV, Lal A (2014) Effect of fly ash hybrid reinforcement on mechanical property and density of aluminium 356 alloy. Procedia Mater Sci 5:746–754

27. Selvam JDR, Smart DR, Dinaharan I (2013) Synthesis and characterization of Al6061-Fly Ashp-SiCp composites by stir casting and compocasting methods. Energy Procedia. 34:637–646

28. Shaikh MBN, Arif S, Siddiqui MA (2018) Fabrication and characterization of aluminium hybrid composites reinforced with fly ash and silicon carbide through powder metallurgy. Mater Res Express 5(4):046506
29. Guo RQ, Rohatgi PK, Nath D (1997) Preparation of aluminium–fly ash particulate composite by powder metallurgy technique. J Mater Sci 32(15):3971–3974
30. Rohatgi PK (1994) Low-cost, fly-ash-containing aluminum-matrix composites. Jom 46(11):55–59
31. Rohatgi PK, Guo RQ, Iksan H, Borchelt EJ, Asthana R (1998) Pressure infiltration technique for synthesis of aluminum–fly ash particulate composite. Mater Sci Eng A 244(1):22–30
32. Guo RQ, Rohatgi PK, Nath D (1996) Compacting characteristics of aluminium-fly ash powder mixtures. J Mater Sci 31(20):5513–5519
33. Kamrani S, Riedel R, Seyed Reihani SM, Kleebe HJ (2010) Effect of reinforcement volume fraction on the mechanical properties of Al-SiC nanocomposites produced by mechanical alloying and consolidation. J Compos Mater 44(3):313–326

# The Application of Microwave and Infrared Drying in Agglomeration Plants of Iron Ore Briquette

**Rishi Sharma and D. S. Nimaje**

**Abstract** In today's era of modernization, where the need for steel is increasing exponentially for almost every country. The utilization of iron ore fines and metallurgical waste for the production of steel is very significant, as the rapid depletion of iron ore reserves continues for many past decades. The process of agglomeration was developed for the proper utilization of iron ore fines produced in the mines. The iron ore mines produce lots of fines as metals are generally formed in the form of narrow veins with a lot of impurities surrounding them. In the process of mining iron ore from beneath the surface of the earth, the conventional method of drilling and blasting is most commonly used in the industry. The metal ore which is present in the form of narrow strips not as a continuous coal bed seam, upon blasting creates lots of iron ore fines mixed with a lot of rock impurities. The agglomeration process is developed for the utilization of such wastes and metallurgical wastes produced from the blast furnace. In this process, iron ore fines and metallurgical wastes such as flue dust and LD sludge are agglomerated in the form of cylindrical briquettes. The cement and bentonite are predominantly used as binders for agglomeration in the iron ore briquette industry. The drying of the iron ore briquette is required to provide initial strength so it can be moved to the storage site as well to the customer with less wear and tear. Generally, in the agglomeration sunlight is used for the drying and initial strength of the briquette. But in rainy seasons and winters, this process takes time and the briquette produced also suffers lots of wear and tear due to less initial strength. There is an immediate need of integrating an initial drying process such as microwave or infrared in the agglomeration plants. The use of drying processes eliminates the bottlenecks related to the unreliable availability of sunlight in the winter and rainy seasons.

**Keywords** Microwave · Infrared · Drying · Briquette · Green strength

R. Sharma (✉) · D. S. Nimaje
National Institute of Technology, Rourkela 769008, India
e-mail: rishi32122@gmail.com

# 1  Introduction

The steel industry provides the raw material for various industries like infrastructure, automobiles, weapons, and space. Iron ore which is depleting rapidly at a fast pace is the major raw material in steel production. The agglomeration of iron ore was started to utilize the iron ore fines which were produced in large quantities in the mines. The agglomeration process or pelletizing is very significant in iron or steel production and also add to the productivity of blast furnace. This process mainly involves balling or agglomeration of the material which takes place in the presence of binder and water capillary formed within the iron ore grains [1]. The iron ore briquette is heated using different techniques to increase its strength. This strength prevents premature disintegration of the briquette in high-temperature conditions of a blast furnace which increases the contact time of CO with the iron ore briquette surface [2]. The different types of metallurgical wastes can also be utilized in iron ore briquette to extract the remaining traces of iron ore in the material [3]. The iron ore agglomeration plant faces great difficulty in functioning during the winter and rainy seasons due to a lack of natural sunlight. The agglomerates produced must be treated with a heat induration process to achieve different mechanical and metallurgical properties for greater efficiency of the blast furnace [4]. So, there is a dire need for the development of drying techniques like microwave and infrared drying to provide initial green strength to the freshly prepared briquettes. The drying process of the agglomerate should be hot enough to remove the required amount of moisture so that it does not break due to saturation or excessive moisture conditions [4]. The microwaves for the drying of iron ore briquettes have been brought to use very recently and it was observed that it is efficient and superior as compared to other conventional methods [5]. The main benefits of this process are good heating control, no direct contact with the material, size of equipment, and flexibility in switching [6, 7]. This initial strength contributes to less wear and tear in the briquette during transportation from one place to another. The briquette's wet strength or initial strength also helps in achieving good reduction characteristics in the blast furnace. The rise in contact time of CO gas with briquette surface helps in the efficient reduction process in the blast furnace. The microwave drying of the briquette starts from inside when waves penetrate the briquette surface and converts the moisture inside into water vapors pushing those outwards through the briquette surface. The infrared drying of the briquette takes place from the outside surface towards the inside when the iron ore briquette is kept under a short wave infrared lamp. The infrared waves start the drying process from the surface towards the internal capillaries or veins of moisture in the briquette. The infrared waves take more time in drying the briquette than microwave drying but in infrared, there are fewer chances of creation of microcracks on the briquette surface. This problem of surface crack generation of microwave drying can be avoided by sucking the moisture from the drying chamber by using a vacuum pump. The iron ore briquette can also be kept on some moisture-absorbent surface to simultaneously absorb the moisture coming out of the briquette surface during the drying process. This also helps in the high rate of drying without compromising the strength of the

briquette. There is also the problem of the economic viability of microwave and infrared drying techniques. The cost of drying can be brought down by drying a large number of briquettes in each batch of drying. The conditions like wattage, power intensity, and time of exposure in these techniques have to be optimized to produce economically viable good quality briquettes for the blast furnaces. The use of different innovative drying techniques for iron ore briquette is the need of the hour for the improvement in the initial strength of the briquette by heat induration. In the case of open-air drying, the initial strength of the iron ore briquettes largely depends upon the weather conditions. It can delay the drying process of the iron ore briquette in winter and the rainy season which affects the initial strength of the briquette in open-air drying. The heat induration using microwave and infrared drying techniques increases the initial strength of the briquettes. The good initial strength contributes to the reduction in breakage of the briquettes during storage and transportation. In this paper, microwave and infrared drying processes are used in industries to determine the effect of both of these methods on the quality and strength of the briquettes. The briquettes with higher strength provide better reduction efficiency in the blast furnace. The selection of these drying methods after reviewing the merits and demerits is based on the most economical and effective method for the iron ore briquette industry.

## 2 Material and Methods

The iron ore fines and different metallurgical wastes were agglomerated in the form of cylindrical iron ore briquette. These briquettes were then dried with the assistance of microwave and infrared drying. This drying gives initial strength to the briquette, which will further increase the productivity of the blast furnace.

## 3 Drying Methods

The different types of drying techniques which can be used for heat induration of iron ore briquettes are microwave drying and infrared drying to provide green strength to freshly prepared briquettes. This process increases the strength of the iron ore briquette which helps in the storage and transportation of the briquette.

### 3.1 Microwave Drying

Earlier microwave drying was used only for pasteurizing, curing, thawing and tempering, etc. But recently, the microwave drying of iron ore briquette and concentrates was used which helps in improving the reduction properties of the briquette upon interaction with CO gas in the blast furnace. The iron ore concentrates were

oxidized for 6 min at a power level of 1300W [1]. Microwave drying when used on iron ore briquettes also creates some pores on the already porous surface and helps in the efficient reduction of iron ore briquettes in furnaces. The porous nature of iron ore briquette helps in creating effective solid–gas contact and in turn, contributes to the reduction process. The grind-ability of iron ore in mineral processing plants for preparing raw material for the agglomeration industry can also be improved by pre-treatment of iron ore lumps in microwaves. These microwaves cause thermal stress cracks in iron ore lumps and help in the comfortable sizing or crushing of iron ore lumps [2]. The loss of weight in iron ore briquette, as well as iron ore concentrates, was mainly due to the removal of moisture during the drying process. The magnetite iron ore was absorbing the microwave heating at 400°C at a faster rate when it reaches 700°C cracks start appearing in the iron ore. At 700°C it was converted to goethite which proves that magnetite ore is a good absorber of heat as compared to magnetite iron ore [1]. The microwave treatment of the iron ore pellets or briquette can also be a good alternative to the sintering process.

The materials behave in three different manners in microwave radiations, not having any effect such as in the case of silica, a reflection of the waves in metals, and absorption of radiation in water or iron-bearing materials [8]. When such absorption of energy takes place in dielectric heating or a rise in temperature of the material occurs due to spinning of dipoles or migration of ionic components [9, 10]. The extent to which a material will absorb the microwave energy mainly depends on the conductivity of the materials.

The materials with low conductivity as shown in Fig. 1 such as insulators are almost transparent to the microwaves. The insulator material absorbs microwaves to store energy in the form of heat and is used as support for the material to be heated in the microwave oven. The metals usually reflect the microwave which contributes towards no significant heating effect and can be used as waveguides for microwaves. The materials with medium conductivity such as semiconductors are very efficient in storing microwave energy in the form of heat as depicted in Fig. 1. Microwave is electromagnetic radiation that is non-ionizing and includes three bands: ultra-high frequency (300 MHz-3 GHz), super high frequency (3−30 GHz), and extremely high frequency (30−300 GHz) [11]. The electromagnetic spectrum is shown in Fig. 2 above and 2450 MHz is the most commonly used frequency in homes was invented by P. L. Spencer almost 60 years ago.

## 3.2   Advantages of Microwave Drying

The usual methods of drying involve convection, conduction, and radiation of the heat from the material surface. But in microwave drying energy is directly transferred through molecular interactions with an electromagnetic field. In conventional drying, heating of the material takes place due to a thermal gradient in contrast to microwaves which penetrate the material to deposit energy and heat can be generated throughout the volume of material [12].
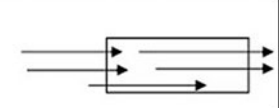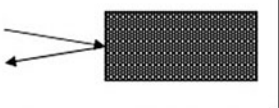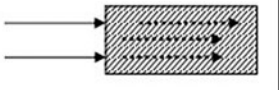
| | Material Type | Penetration |
|---|---|---|
|  | TRANSPARENT (no heat) | Total transmission |
|  | CONDUCTOR (no heat) | None |
|  | ABSORBER (materials are heated) | Partial to total absorption |

**Fig. 1** The behavior of different materials under microwave [12]
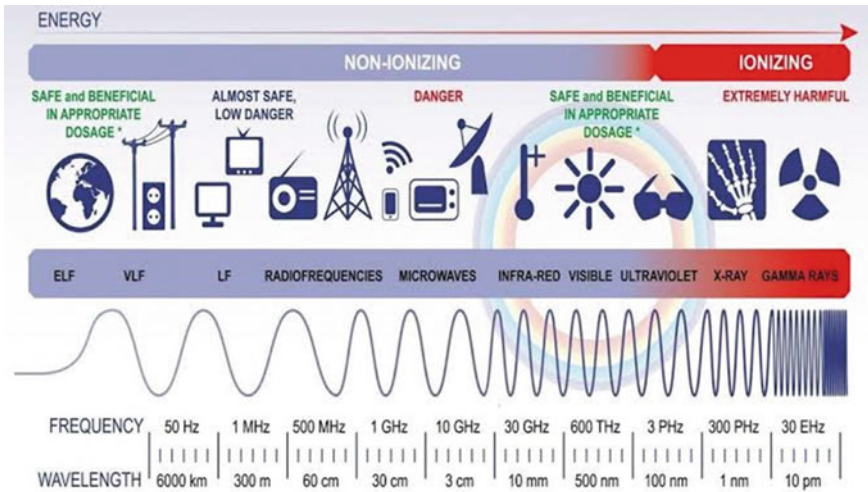


**Fig. 2** Electromagnetic spectra- invented by P.L. Spencer. *Source* https://www.secretsofuniverse.in/the-em-spectrum/

Merits of microwave drying.

- Rapid heat generation.
- Power saving (Automatic control).
- The flexibility of equipment for adjustments.
- Material selective heating.
- Environmental friendly.

## 3.3 Infrared Drying

The use of infrared drying for the initial green strength of iron ore briquette is quite new in the agglomeration industry and it's not been studied properly for its advantages and disadvantages yet. But, whatever small work has been done in this regard shows that this technique heats the material from the outside towards the inside and the process is slow as compared to microwaves.

In some cases, iron ore sinter feed after being sintered in the furnace is monitored using an Infrared camera as shown in Fig. 3. The surface temperature of the sinter feed was studied using of emissivity of the sinter feed material. Emissivity calibrations have to be considered in the case of materials with low emissivity values but sinter feed material has already high emissivity values required for measuring temperatures using infrared cameras. The temperature of the iron ore sinter feed can be measured by infrared imaging and then other quality parameters of the sinter were taken into consideration for different surface temperatures. In this way, the heating temperature of the sinter feed can be optimized for better quality products [13].

When sinter feed is heated in a laboratory-scale furnace with the help of external fuel injection in the form of gas. In this arrangement surface of the sinter, feed bed was monitored with the help of an infrared device for temperature measurements as shown in Fig. 4. The constant monitoring of bed surface temperature helps in optimizing the heating of sinter feed by adjusting the supply of injection gas [14].

The sintering process of iron ore feed can also be performed by replacing fine iron ores with coarse iron ore and heating them in a small-scale infrared furnace. The infrared furnace Model E4-10 Chamber-IR was used for the sintering process, which consists of four aluminum reflectors and four infrared lamps as shown in Fig. 5. Each infrared lamp is made up of a quartz tube with a tungsten filament, which emits a lot of radiant energy after being reflected from the aluminum surface and is focused on the center zone [15].
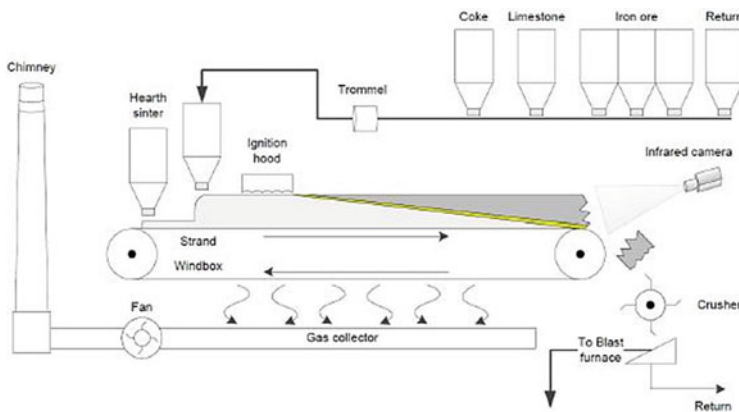


**Fig. 3** Sintering process using dwight-lloyd machine [13]

**Fig. 4** Lab-scale sinter test with secondary fuel injection [14]
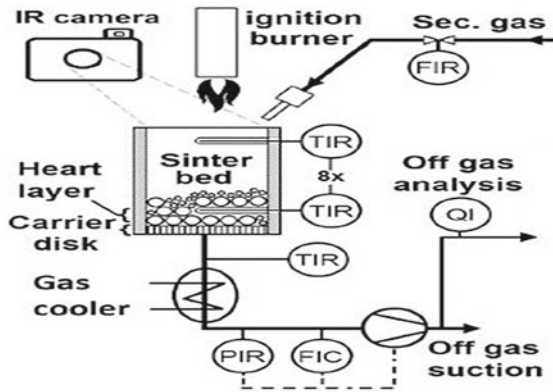


**Fig. 5** Radial heating configuration in the infrared furnace [15]
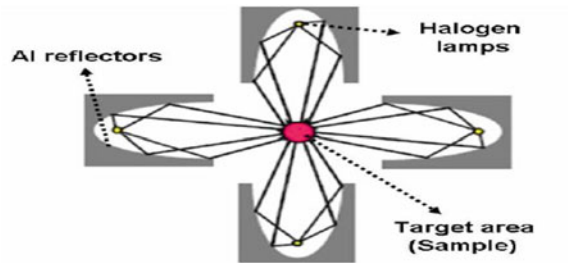


The infrared furnace (see Fig. 6) uses infrared radiation as the source of energy for heating. The furnace reaches a very high-temperature (1700°C) in a short interval of time as compared to conventional sintering techniques [16]. There are less chances of development of cracks in this technique as compared to microwaves where the formation of various major and minor cracks was observed on the briquette surface. The economic viability of infrared drying can be brought down by using this technique on large after calculating the optimum value of different parameters such as power intensity and time of exposure. This optimum value depends upon the conditions in which good quality mechanical and reduction properties can achieve in the blast furnace.

## *3.4 Comparative Analysis*

See (Table 1).

**Fig. 6** Infrared furnace [16]



**Table 1** Comparative analysis of microwave and infrared drying

| Parameters | Open-air drying | Microwave drying | Infrared drying |
|---|---|---|---|
| Porosity | No major impact of open-air drying on porosity | Microwaves create a lot of pores as they penetrate the samples and start heating from inside to outside | Infrared waves do not create pores in the sample as the heating takes place from the surface towards the inside of the sample |
| Compressive strength | The strength is 0.476 Mpa after one day drying | The strength is 1.78 Mpa one day after drying | The strength of the sample is 1.62 Mpa one day after drying |
| Drying mechanism | The direction of heating from the surface towards inside | The direction of heating from the inside towards the outside creates a lot of cracks | The heating occurs from the outside towards the inside and avoids the formation of cracks |
| Frequency of electromagnetic waves | N/A | 300 GHz to 430 THz | 300 MHz to 300 GHz |
| Power capacity | N/A | It requires less power compared to infrared | It requires more power compared to microwave |
| Reduction characteristics | No major impact on reduction characteristics of iron ore briquette | High reduction due to higher porosity as compared to infrared drying but premature disintegration could occur due to less strength | Low reduction due to higher porosity as compared to infrared drying but less chance of premature disintegration could occur due to high strength |
| Sample deterioration | It has no major effect on quality but takes a longer duration | High deterioration of the sample due to the formation of cracks | Less deterioration of the sample as no cracks were formed in drying |

# 4  Conclusion

The iron ore fines can be agglomerated with the help of binders such as bentonite in conjunction with metallurgical waste like flue dust and sludge. The iron ore briquette should be strong during storage, transportation, and high-temperature conditions of blast furnaces. The premature disintegration of briquettes in the furnace can lower the reduction of iron ore. The microwave drying techniques can be readily adopted in the agglomeration industry as compared to infrared drying as long as it does not affect the strength of the iron ore briquette. The infrared takes more time for drying but the physical structure of the briquette remains intact, and no crack formation is observed as in the case of microwaves. It reflects the selection of the best drying techniques in iron ore briquette industries. The continuous microwave and infrared drying setup in the form of a tunnel may be used in iron ore briquette industries to enhance the production and ensure the quality of the briquettes. To develop the cost-effective drying of iron ore briquettes, the optimization of microwave and infrared dryers would be required in the current scenario of briquette industries, and also increases the efficiency of the dryer.

# References

1. Forsmo SPE, Samskog PO, Björkman BMT (2008) A study on plasticity and compression strength in wet iron ore green pellets related to real process variations in raw material fineness. Powder Technol 181(3):321–330
2. Walkiewicz JW, McGill SL, Moyer LA (1988) Microwave processing of materials. In: Materials research society symposium proceedings, vol 124
3. Standish N, Pramusanto P (1991) Reduction of microwave irradiated iron ore particles in CO. ISIJ Int 31(1):11–16
4. Carvalho MMO, Faria DG, Pérez MG, Cardoso M, Vakkilainen EK (2017) Review on mathematical models for traveling-grate iron oxide pellet induration furnaces. Energy Procedia 120:588–595
5. Guo S, Li W, Peng J, Niu H, Huang M, Zhang L (2009) Microwave-absorbing characteristics of mixtures of different carbonaceous reducing agents and oxidized ilmenite. Int J Miner Process 93(3–4):289–293
6. Pereira ROS, Seshadri V (1985) Secagem de pelotas de minério deferro. Metalurgia 328:141–144
7. Huang Z, Yi L, Jiang T, Zhang Y (2012) Hot airflow ignition with microwave heating for iron ore sintering. ISIJ Int 52(10):1750–1756
8. Khaled DE, Novas N, Gazquez JA, Manzano-Agugliaro F (2018) Microwave dielectric heating: applications on metals processing. Renew Sustain Energy Rev 82:2880–2892
9. Shaohua J, Singh P, Jinhui P, Nikoloski AN, Chao L, Shenghui G (2018) Recent developments in the application of microwave energy in process metallurgy at KUST. Miner Process Extr Metall Rev 39:181–190
10. Ogunniran O, Binner ER, Sklavounos AH, Robinson JP (2017) Enhancing evaporative mass transfer and steam stripping using microwave heating. Chem Eng Sci 165:147–153
11. Haque KE (1999) Microwave energy for mineral treatment processes, a brief review. Int J Miner Process 57:1–24
12. Çırpar Ç (2005) Heat treatment of iron ore agglomerates with microwave energy. Master's thesis, Middle East Technical University

13. Legemza J, Fröhlichová M, Findorák R (2014) The thermovision measurement of temperature in the iron-ore sintering process with the biomass. In: Acta metallurgica slovaca-conference, vol 4. pp 56–65
14. Tsioutsios N, Weiss C, Rieger J, Schuster E, Geier B (2020) Flame front progress in gas assisted iron ore sintering. Appl Therm Eng 165:114554
15. Nyembwe MA (2012) Study of sinter reactions when fine iron ore is replaced with coarse ore, using an infrared furnace and sinter pot tests. Doctoral dissertation, University of Pretoria
16. De Alencar JPSG, Pimenta FV, Botelho MEE, Vieira MB, Pimenta HP (2012) Understanding the behavior of sinter feeds at high temperatures. In: 6th international congress on the science and technology of ironmaking–ICSTI Rio de Janeiro, RJ, Brazil

# The Effect of Thermal Aging on the Wear Behavior of Glass Fiber-Epoxy Matrix Composite with SiC as Filler Material

**S. S. Sahoo, D. K. Mishra, and R. P. Dalai**

**Abstract** Adding fillers in glass fiber-epoxy matrix composite enhances the thermal, physical, and mechanical properties due to a strong bonding (interfacial) between the matrix and reinforcement material. These composite materials are mainly applicable to the aerospace and automotive industries. This work investigates the effect of thermal aging on the wear behavior of glass fiber-epoxy matrix composite with SiC as filler material fabricated by the hand lay-up method. A wear testing machine (pin-on-disk) measures the amount of wear loss of the composite samples after thermal aging. The thermal aging conditions are heating in an oven at 90 °C for 3, 6, 9, and 12 h. The amount of water absorption increases with the thermal aging time from 3 to 12 h. The wear rate or wear loss increases linearly as the load increases. The wear rate or wear loss increases when the speed increases for a constant load. Thermal aging reduces the wear loss due to enhancement in hardness. This reduction is due to higher cross-linking for an aging time of up to 12 h.

**Keywords** SiC filler · Interfacial bonding · Thermal aging · Wear rate

## 1 Introduction

The glass fiber reinforced polymer matrix composites (GFRPMCs) provide better mechanical, thermal, and tribological properties [1–3]. Due to these properties, GFRPMCs are generally applicable for construction, aerospace, automobiles, and electrical insulation industries [4–6]. Epoxy polymer resin (EPR) as a matrix in GFRPMCs offers excellent adhesive properties, flexibility, low shrinkage upon cure, high hardness, good heat resistance, high electrical resistance, superior temperature stability, and good tribological properties to these composites [7–12]. The addition of filler materials into the GFRPMCs enhances the mechanical, thermal, and tribological properties of GFRPMCs [2, 13–15]. The presence of SiC particles in the GFRPMCs

S. S. Sahoo · D. K. Mishra · R. P. Dalai (✉)
Department of Metallurgical and Materials Engineering, Veer Surendra Sai University of Technology, Burla 768018, India
e-mail: rpdalai_mme@vssut.ac.in

enhances its flexibility and strength by forming strong covalent bonds between the polymer and the reinforced fiber. It transforms the load from the polymer to the ceramic particles and provides much higher strength and stiffness [1, 16, 17]. Hence, the addition of small amounts of SiC particles as fillers enhance the mechanical properties and wear resistance of GFRPMCs [10, 18, 19]. Vaggar et al. observe that with the increase in SiC filler amount, the thermal conductivity of composite increases, and above 15% filler, it increases to a greater extent [20]. According to Rana et al., the flexural strength increases by increasing the SiC quantity in the polymer matrix composites [21]. Akash et al. observe that the 6% filler content shows better hardness, tensile, and flexural properties than the 0, 2, and 4% fillers [22]. Chethan et al. suggest that the ideal SiC content for impact, tension, and flexural strength is 3.5 wt% [23]. The dry sliding wear mechanism for GFRPMCs is a failure in the matrix, breaking of fiber or fracture of fiber, and fiber-matrix debonding. The addition of SiC particles as filler material enhances the wear resistance of the GFRPMCs. Hence, this work aims to investigate the effect of thermal aging in artificial seawater (3.5wt% NaCl solution) on the hardness and sliding wear properties of GFRPMCs with SiC as the filler material.

## 2   Experimental Methodology

Figure 1 represents the flowchart for the fabrication, thermal aging, and property evaluation of the developed GFRPMCs with SiC as the filler material. The main ingredients to fabricate the GFRPMCs are epoxy resin (LY-556) as the matrix, E-glass fibers as the reinforcement, hardener HY 951 (aliphatic primary amine), and SiC particles (37 µm) as a filler material. Magnetic stirring of the SiC powder particles with acetone for an hour at 100 rpm at room temperature lowers the chance of the formation of agglomerates. Then the addition of epoxy and hardener in a ratio of 10:1 with stirring again at 120 °C evaporates the acetone. The GFRPMC laminate, with 30wt% fiber, 60wt% epoxy with hardener as the matrix, and 10wt% SiC as filler material, is fabricated by the hand lay-up method. The thermal aging conditions are heating in an oven at 90 °C for 3, 6, 9, and 12 h in 3.5% NaCl solution. A universal Vickers hardness tester (AFFRI, 251 VRSA) measures the hardness of the thermally aged composite samples with 15 s dwell time at 1000gm load. A wear testing machine (pin-on-disk, Ducom TR-201) helps to measure the wear properties of the thermally aged composite samples. During this process, the specimen pin is sliding against a silicon carbide abrasive paper attached to a hardened steel disk.

**Fig. 1** Flow chart for the fabrication and properties of GFRPMCs
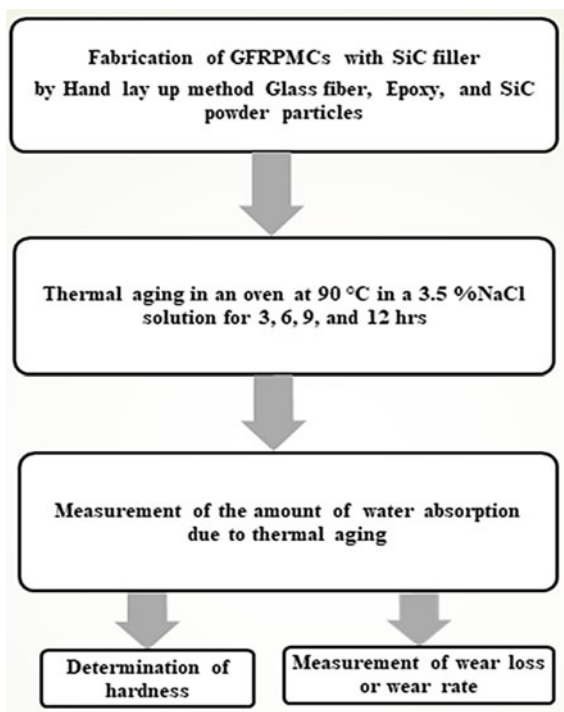
## 3  Results and Discussions

### 3.1  Effect of Thermal Aging on Water Absorption

Figure 2 shows the weight gain versus thermal aging time for the GFRPMCs with SiC as the filler material in a 3.5wt% NaCl solution. The result depicts that the amount of water absorption represents the weight gain of the composite sample with the aging time. Thermal aging for 3 h composite shows less weight gain. But with increasing aging time, from 3 to 12 h, the water absorption amount increases. In this work, thermal aging is carried out in an oven at 90 °C in a 3.5wt% NaCl solution (artificial seawater). During aging, the composite sample picks up water from the NaCl solution. The composite samples absorb some amount of water during thermal aging and the mechanism of this water absorption is diffusion.

### 3.2  Effect of Thermal Aging on Hardness

Figure 3 depicts the effect of thermal aging in 3.5% NaCl solution on the Vickers hardness of GFRPMCs with SiC as the filler material. Thermal aging improves the

**Fig. 2** Wt. gain versus
thermal aging time for the
GFRPMCs with SiC as the
filler material
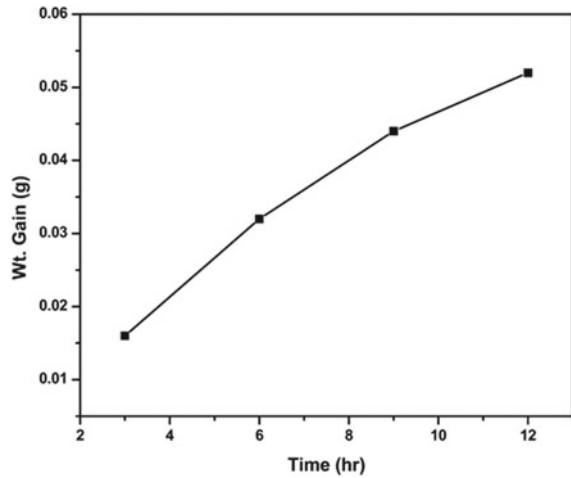


hardness of the composite by increasing the aging time from 3 to 9 h. This increase in
hardness is due to post-curing (which enhances the interfacial bond strength between
the glass fiber, matrix, and the SiC filler) and an increase in cross-linking between
the hydrogen bonds present in water and epoxy [24, 25]. However, there is no signif-
icant enhancement in the hardness value from 9 to 12 h. This minor improvement
in hardness is due to the increase in cross-linking of the epoxy matrix. However,
with increasing aging time, hydrogen bonds get weak and easily broken, leading to
deterioration in the hardness values [26].

**Fig. 3** Hardness versus
thermal aging time for the
GFRPMCs with SiC as the
filler material
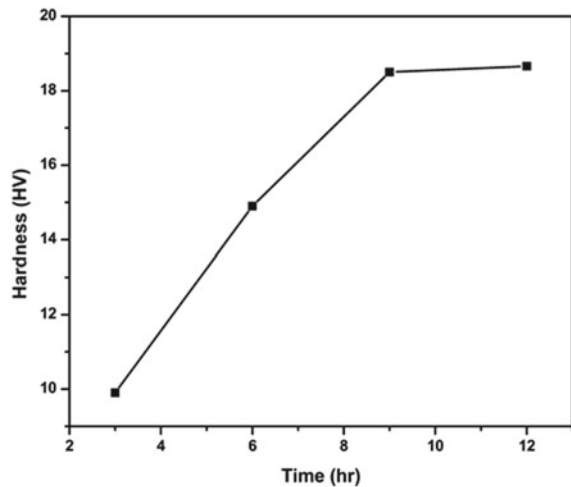
## 3.3 Effect of Sliding Velocity on Wear Loss

Figure 4 represents the weight loss or wear loss versus sliding velocity curves for different weight percentages of glass fiber and SiC particles. Equation (1) helps to calculate the sliding velocity. Equation (2) helps to determine the number of revolutions used for the wear process. During the sliding wear process, due to the friction between the composite sample surface and silicon carbide abrasive paper, some amount of material is lost from the composite surface. Equation (3) determines the wt. loss or wear loss of the developed GFRPMCs composite with SiC as the filler material.

$$\text{Sliding velocity } V = D/t \tag{1}$$

where D is the distance traveled in m and t is the testing time duration in sec

$$V = \pi dN/60 \tag{2}$$

where d is the track diameter and N is the number of revolution

$$W_L = W_I - W_F \tag{3}$$

where $W_L$ is the wt. loss of the composite due to wear, $W_I =$ Initial wt. of the composite, and $W_F =$ Final wt. of the composite.

The wear testing parameters are a constant sliding distance of 2000 m and a constant load of 49N with different sliding velocities such as 2, 4, and 6 m/s. Figure 3 depicts that the weight loss of the composite samples increases as the sliding velocity increase from 2 to 6 m/s. Figure 3 also confirms that thermal aging for a 3 h composite sample provides less wear resistance capacity than the other composite samples.

**Fig. 4** Weight loss versus sliding distance of the GFRPMCs with SiC filler
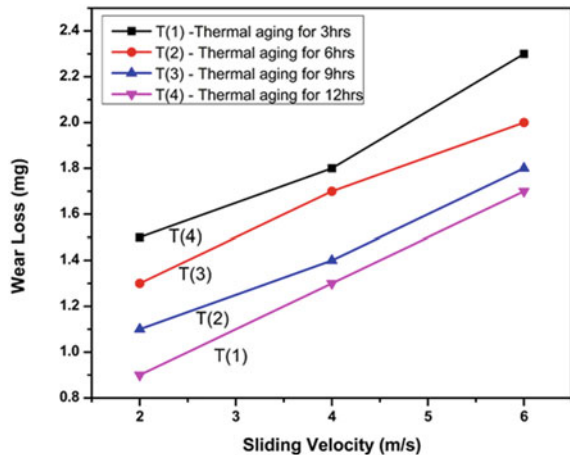
Thermal aging improves the wear resistance of the composite due to the improvement in hardness.

## 3.4  Effect of the Load on Wear Loss

Figure 4 shows the rate of weight loss by varying the load and the thermal aging time for a constant sliding distance of 4 m/s. With increasing the thermal aging time from 3 to 12 h, weight loss or wear rate decreases. The reduction in wear rate is due to the increase in hardness due to thermal aging. Figure 4 depicts that weight loss increases with increasing the load from 9.8N to 49N. According to Eq. (3), wear rate is directly proportional to the applied load. Also, the contact between the composite sample surface and the silicon carbide paper increases as the load increases from 9.8 to 49N. Due to friction, the wear loss or wear rate increases as the load increases.

$$W = KF/H \qquad (4)$$

where W is the wear rate, K is the wear coefficient, F is the load, and H is the hardness of the softer material.

Equation (4) shows Archard's wear equation, the relation between the wear loss or wear rate with the hardness of the soft surface [27]. According to Eq. (4), the wear rate is inversely proportional to the hardness, and the wear rate decreases as the hardness increases (Fig. 5).

Figure 6 shows the optical micrographs of the developed GFRPMCs sample surfaces before and after the sliding wear test. Figure 6a depicts the composite sample surface before the wear test. Figure 6b-e shows the wear mechanisms due to



Fig. 5  Weight loss versus load of the GFRPMCs with SiC filler
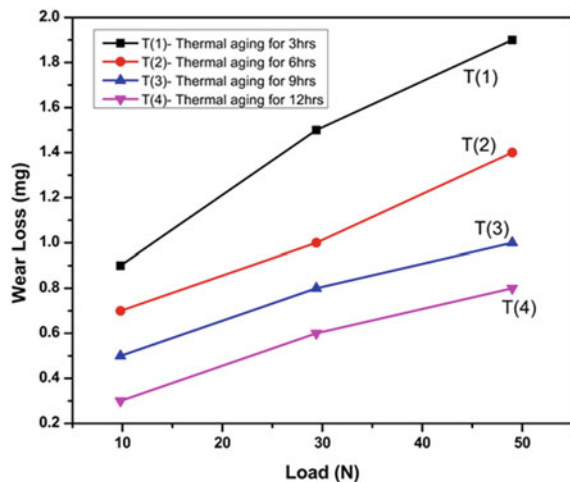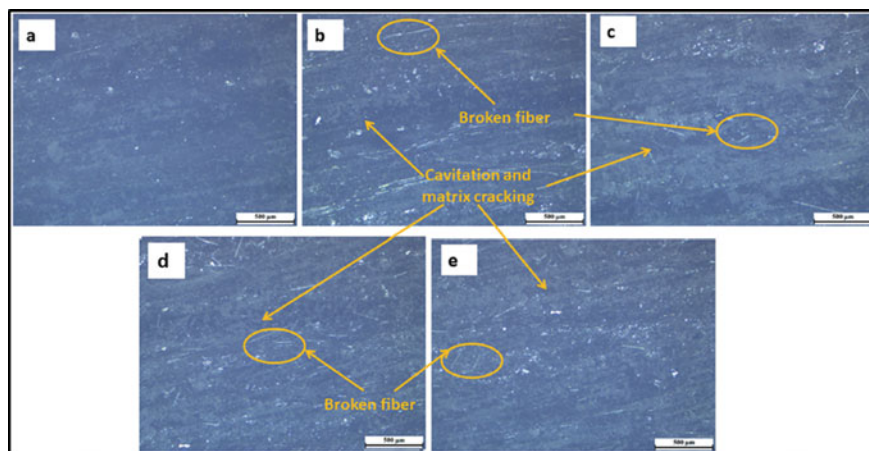
**Fig. 6** Optical micrographs of the worn out surfaces of the thermally aged composite samples **a** before wear, and after wear at 50N **b** 3 h thermally aged, **c** 6 h thermally aged, **d** 9 h thermally aged, and **e** 12 h thermally aged

sliding wear are matrix cracking, breaking of fibers, and cavitation occurring in all the composite sample surfaces. However, the 12 h thermal aging composite sample surface shows relatively low matrix cracking, breaking of fibers, and cavitation than the thermal aging at 9, 6, and 3 h composite samples. The high hardness and low loss or wear rate of the 12 h thermally aged composite sample provide a higher wear-resistant capacity than the other thermally aged composite samples.

## 4   Conclusions

The following conclusions obtained from the present work.

  (i).   The amount of water absorption is more for 12 h composite sample than 3, 6, and 9 h during thermal aging.

 (ii).   Thermal aging improves the hardness of the developed GFRPMCs with SiC as filler material.

(iii).   The wear rate or wear loss increases with increasing the sliding speed.

(iv).   Thermal aging reduces the wear rate or enhances the wear resistance of the GFRPMCs with SiC as filler material.

 (v).   However, increasing the sliding speed and load, the wear rate increases for all the thermal aged composite samples.

# References

1. S. J. M, S. K. L, Sudarshan DS, S. K. M, Yogesha KK, Nayak SS (2021) Effect of silicon carbide fillers on the mechanical properties of glass fibre reinforced epoxy polymer composite. Inter Res J Eng Tech 8:4032–4036
2. Nayak S, Nayak RK, Panigrahi I, Sahoo AK (2019) Tribo-mechanical responses of glass fiber reinforced polymer hybrid nanocomposites. Mater Today Proc 18:4042–4047
3. Ahmad S, Ali S, Salman M, Baluch AH (2021) A comparative study on the effect of carbon-based and ceramic additives on the properties of fiber reinforced polymer matrix composites for high temperature applications. Ceram Int 47:33956–33971
4. Patel S, Sengupta R, Puntambekar U, Shingne N (2021) Materials today: proceedings effect of different types of silica particles on dielectric and mechanical properties of epoxy nanocomposites. Mater Today Proc 44:1848–1852
5. Huang Z, Zhao W, Zhao W, Ci X, Li W (2021) Tribological and anti-corrosion performance of epoxy resin composite coatings reinforced with differently sized cubic boron nitride (CBN) particles. Friction 9:104–118
6. Liang H, Xu M, Chen X, Bu Y, Zhang Y, Gao K, Min C, Hua X, Fu Y (2021) Impressive high-temperature lubrication of carbon/epoxy composites endowed by the microscopic dimensionality of carbon fillers. Wear 486–487:204109
7. Jakab B, Panaitescu I, Gamsjager N (2021) The action of fillers in the enhancement of the tribological performance of epoxy composite coatings. Poly Testing 100:107243
8. Kim MS, Rhee KY, Park SJ (2016) Pitch coating of SiC and its effects on the thermal stability and oxidation resistance of SiC/epoxy composites. Compos Part B Eng 94:218–223
9. Brostow W, Dutta M, Rusek P (2010) Modified epoxy coatings on mild steel: tribology and surface energy. Eur Polym J 46(11):2181–2189
10. Dalai RP (2010) An assessment of mechanical behaviour of fibrous polymeric composites under different loading speeds at above and sub-ambient temperatures. Master thesis, National institute of Technology, Rourkela
11. Dalai RP, Ray BC (2011) Failure and fractography studies of FRP composites: effects of loading speed and environments. In: Proceedings of the processing and fabrication of advanced materials XIX. Auckland, New Zeland
12. Dalai RP, Ray BC (2010) Cross head velocity sensitivity of fibrous composite materials. In: International conference on recent trends in materials and characterization. RETMAC
13. Kiran MD, Govindaraju HK, Jayaraju T (2018) ScienceDirect evaluation of mechanical properties of glass fiber reinforced epoxy polymer composites with alumina, titanium dioxide and silicon carbide fillers. Mater Today Proc 5:22355–22361
14. Kumar Singh S, Kumar A, Jain A (2018) Improving tensile and flexural properties of $SiO_2$-epoxy polymer nanocomposite. Mater Today Proc 5:6339–6344
15. Bharath Kumar T, Haseebuddin MR, Raghavendra N, Vishnu Mahesh KR (2018) Influence of sic on mechanical, thermal, fire and wear studies of vinylester/glass fibre composites. Mater Today Proc 5:22675–22686
16. Kwon D et al (2017) Interfacial properties and thermal aging of glass fiber/epoxy composites reinforced with SiC and $SiO_2$ nanoparticles. Compos Part B 130:46–53
17. Liu G, Zhang X, Yang J, Qiao G (2019) Recent advances in joining of SiC-based materials (monolithic SiC and $SiC_f$ /SiC composites): joining processes, joint strength, and interfacial behavior. J Adv Ceram 8:19–38
18. Kim SY, Han IS, Woo SK, Lee KS, Kim DK (2013) Wear-mechanical properties of filler-added liquid silicon infiltration C/C-SiC composites. Mater Des 44:107–113
19. Basavarajappa S, Ellangovan S (2012) Dry sliding wear characteristics of glass-epoxy composite filled with silicon carbide and graphite particles. Wear 296:491–496
20. Vaggar GB, Kamate SC, Badyankal PV (2019) A study on thermal conductivity enhancement of silicon carbide filler glass fiber epoxy resin hybrid composites. Mater Today Proc 35:330–334
21. Rana RS, Buddi T, Purohit R (2021) Effect of SiC reinforcement on the mechanical properties of Kevlar fiber based hybrid epoxy composites. Mater Today Proc 44:2478–2481

22. Akash S, Avinash S, Ramachandra M (2018) A study on mechanical properties of silk fiber reinforced epoxy resin bio-composite with SiC as filler addition. Mater Today Proc 5:3219–3228
23. Chethan S, Suresha S (2021) Effect of SiC particulates as secondary reinforcement on mechanical characteristics of epoxy composites with treated luffa cylindrica fibres. Mater Today Proc 44:1755–1760
24. Alessi S, Pitarresi G, Spadaro G (2014) Effect of hydrothermal ageing on the thermal and delamination fracture behaviour of CFRP composites. Compos Part B Eng 67:145–153
25. Moreno IG, Caminero MA, Rodriguez GP, Lopez-Cela JJ (2019) Effect of thermal ageing on the impact and flexural damage behaviour of carbon fibre-reinforced epoxy laminates. Polymers 11: 1–16
26. Kwon DJ, Shin PS, Kim JH, Baek YM, Park HS, DeVries KL, Park JM (2017) Interfacial properties and thermal aging of glass fiber/epoxy composites reinforced with SiC and $SiO_2$ nanoparticles. Compo Part B: Eng 130:46–53
27. Tabrizi AT, Aghajani H, Saghafian H, Laleh FF (2021) Correction of archard equation for wear behavior of modified pure titanium. Tribo Inter 155:1–7

# First Principle Study of Defect Induced Band Structure in Cu Substituted $Bi_2Te_3$ Topological Insulator

**Sambhab Dan, Debarati Pal, and Swapnil Patil**

**Abstract** This paper deals with the Cu substituted $Bi_2Te_3$ topological insulator's electronic band structure and its defect induced behavior. The pristine $Bi_2Te_3$ compound has a unique band structure, where the bulk band is semiconducting and the surface band is metallic. However, here, we report the modulation of the bulk-band structure with the injection of Cu atoms in the pristine $Bi_2Te_3$ compound. Our ab initio simulation reveals that 5 at.% of Cu substitution in Bi site transforms the electronic ground state of $Bi_2Te_3$ to a *p*-type one. In contrast, the intercalation of Cu atoms by a similar amount turns the electronic ground state of $Bi_2Te_3$ into an *n*-type one. We have also discussed the band structure of the carrier-compensated configuration of the Cu substituted $Bi_2Te_3$ compound with the creation of Te vacancy. Our simulation gives an excellent agreement with the experimentally.

**Keywords** Topological insulator · Chalcogenides · Fermi level · Bulk band

## 1 Introduction

Topological Insulator (TI) is a new branch of science that draws significant attention in the contemporary field of material science and technology. Although the observation of two-dimension (2D) TI was reported earlier, the invention of 3D TI brought a new vista in condensed matter physics [1]. Chalcogenides are the first investigated compound in 3D TI, and its most exciting feature lies in its novel electronic band structure [2]. The system shows a semiconducting bulk band (BB) and the metallic surface state (SS). After investigating chalcogenide compounds ($Bi_2Te_3$, $Bi_2Se_3$, $Sb_2Te_3$), a gamut of 3D TI along its doped compositions are extensively studied. The doped compositions of the 3D TI also exhibit some of the great features in fundamental science, which are enormously useful in technological applications, viz. photodetector, magnetic device, field-effect transistor (FET), laser, and so on

S. Dan · D. Pal · S. Patil (✉)

Department of Physics, Indian Institute of Technology (Banaras Hindu University), Varanasi 221005, India

e-mail: spatil.phy@itbhu.ac.in

[3]. Earlier studies revealed that Cu substituted TI based chalcogenides show fascinating features. The Cu intercalated $Bi_2Se_3$ shows superconducting behavior [4], the doping of Cu atom on the Te site in $Bi_2Te_3$ gives rise the defect induced magnetic properties [5], and a tiny amount of Cu doping in the Bi site of $Bi_2Te_3$ can raise the *p*-type to *n*-type carrier transition [6]. Our study reveals how the 5 at.% of Cu doping at various sites of $Bi_2Te_3$ can raise a *p*-type and *n*-type compound. Interestingly, our theoretical analysis unfolds the inside view of recently observed hole-dominated metallic ground state configuration in Cu substituted $Bi_2Te_3$ compound [7].

In this paper, we have studied the bulk band structure of four different stages of Cu insertion: (i) the pristine one, (ii) 5 at.% of Cu substitution in Bi site, (iii) 8 at.% of Cu substitution in Bi site, with Te vacancy, to make the system carrier-compensated, (iv) 5 at.% of Cu intercalated in the Van der Waals gap of $Bi_2Te_3$.

## 2 Methods

### 2.1 *Step by Step Procedure of Unit Cell Preparation*

To study the electronic structure, we have configured the unit cell as $2 \times 2 \times 1$ supercell. One unit cell of $Bi_2Te_3$ (Fig. 1) contains three formula units, and each formula unit contains two Bi atoms and three Te atoms. So one unit cell of $Bi_2Te_3$ compound contains 6 Bi atoms and 9 Te atoms. If we make $2 \times 2 \times 1$ supercell, the size of a supercell becomes four times of one unit cell. Such a supercell contains 24 Bi atoms and 36 Te atoms. Now, for the 5 at.% of Cu doping at the Bi site of the $Bi_2Te_3$ crystal, we have to replace one Bi atom with one Cu atom. Such an arrangement takes the final form of a supercell containing one Cu atom, 23 Bi atoms, and 36 Te atoms. This supercell is equivalent to ~4.2 at.% of Cu doping in the Bi site in the $Bi_2Te_3$ compound.

### 2.2 *Simulation Methodology and Software Used*

The bulk band structure is calculated using the Projected Augmented Wave (PAW) method as implemented in the *Vienna* Ab initio Simulation Package (VASP) [8] within the Generalized Gradient Approximation (GGA) [9] of the Perdew–Burke–Ernzerhof (PBE) scheme. We have configured the unit cell as $2 \times 2 \times 1$ supercell for the study of the electronic structure. During the structure optimization, we used the experimental lattice parameters and relaxed the atom position only. Structure optimization was done until the residual forces were less than 0.01 eV $\text{Å}^{-1}$. The electronic structures were calculated using Monkhorst–Pack $2 \times 2 \times 1$ *K*-point mesh. The spin–orbit coupling (SOC) has been included during the Self-Consistency Field

**Fig. 1** Unit cell of rhombohedral (space group: *R*-3*m*, #166) $Bi_2Te_3$ crystal
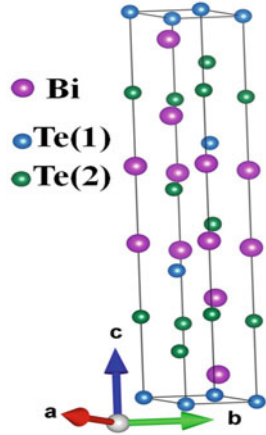


(SCF) run. The basis set of plane waves with the kinetic energy cut off ($E_{cut-off}$) of 300 eV was used in the simulation [10].

## 3 Results and Discussion

### 3.1 The Pristine One

The unit cell of the pure $Bi_2Te_3$ crystal is shown in Fig. 1. The crystal structure contains five monoatomic layers in a pattern of Te(1)–Bi–Te(2)–Bi–Te(1). The van der Waals gap is present between the two successive quintuple layers. The electronic band structure of the pure $Bi_2Te_3$ is shown in Fig. 2a. We have observed that the bulk band structure of the pure compound acts as an intrinsic semiconductor with a shallow bandgap (~170 meV) [11].

### 3.2 The Cu Substitution in the Bi Site

To make 5 at.% of Cu doping in Bi site, we have replaced one Bi atom with one Cu atom in the supercell. In pristine $Bi_2Te_3$, the Bi and Te atoms have $3^+$ and $2^-$ ionic states. Replacing one Bi atom with one Cu atom makes the system hole-doped (as the Cu atom has a $2^+$ ionic state). Such doping makes the structure a *p*-type compound (Fig. 2b). From Fig. 2b, it is also shown that the Fermi level of the compound lies deep in the valence band, indicating the hole-like metallic phase of the compound. Such a result unfolds the origin of the bulk metallic phase of the same compound in the recently published article [7].
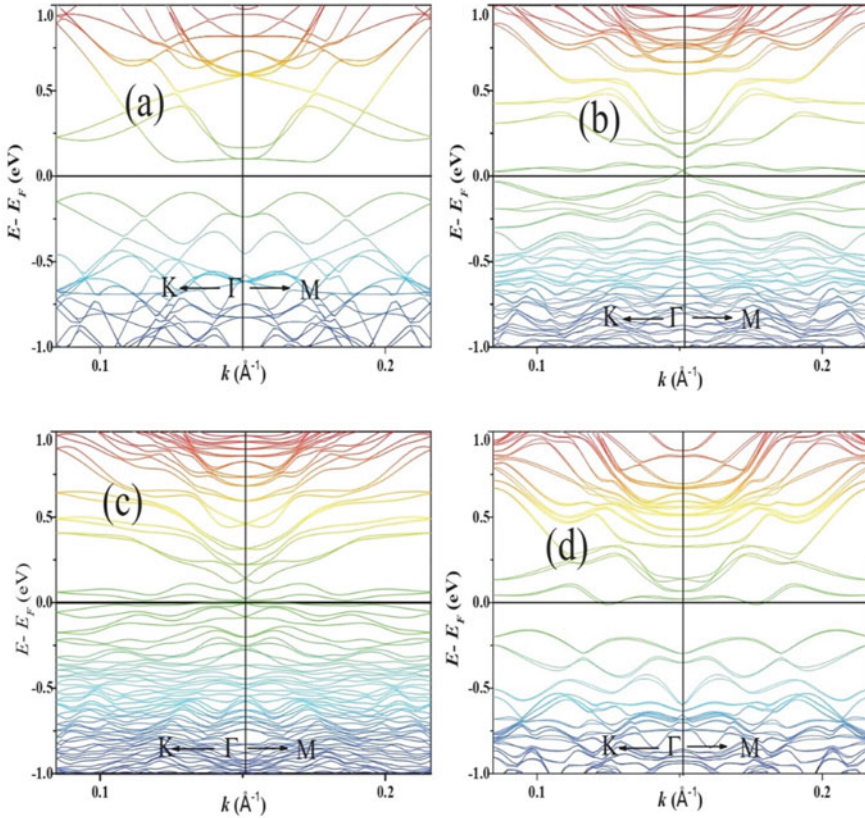
**Fig. 2** Simulated band structure of the following configurations: (**a**) pure $Bi_2Te_3$ compound, (**b**) Cu-substituted (5 at.%) $Bi_2Te_3$ compound, (**c**) Cu-substituted (8 at.%) $Bi_2Te_3$ compound with carrier-neutral configuration and (**d**) Cu intercalated (5 at.%) in the Van der Waals gap of $Bi_2Te_3$ compound

## 3.3 The Carrier-Neutral Configuration

One formula unit of the $Bi_2Te_3$ compound contains 2 Bi atoms and 3 Te atoms. Bi and Te atoms form $Bi^{3+}$ and $Te^{2-}$ ionic state; that means in one formula unit 2 Bi atom gives a total of 6 electrons to fulfil its octet and 3 Te atoms take these 6 electrons (to achieve its octet). Now, the Cu atom can form a $Cu^{2+}$ ionic state. If we replace one Bi atom with one Cu atom, 5 electrons (3 from Bi and 2 from Cu) are donated to fulfil the octet of one Bi and one Cu atom in one formula unit. These 5 electrons are taken by 3 Te atoms in that particular formula unit. But as the Te atom is in $Te^{2-}$ ionic state, 3 Te atoms need 6 (instead of 5) electrons to complete its octet. Such arrangement causes one electron crisis in the Te site and makes the system hole-doped. To make the system carrier-neutral, we have replaced two Bi atoms with two Cu atoms and created one Te vacancy. One formula unit contains only two Cu and two Te atoms

for this arrangement. In such a scenario, 4 electrons are exchanged from the Cu site to the Te site, and the system becomes carrier-neutral. This structure contains 2.7 at.% of Te vacancy with 8.3 at.% of Cu doping in the Bi site. The bulk band of such a configuration shows a *p*-type nature (Fig. 2c). During making the configuration, we have ensured that all the vacancies and substitutions are created within the same quintuple layer (one quintuple layer is equivalent to one formula unit in $Bi_2Te_3$); otherwise, it would act as an isolated defect in the crystal [10].

### 3.4 The Cu Intercalation in the van der Waals Gap

For our last configuration, we have placed one Cu atom between the two quintuple layers of the compound (5 at.% Cu intercalation). In this case, the Cu atom acts as an electron donor. Figure 2d shows that the Fermi level of such a configuration lies very close to the bottom edge of the conduction band, making an *n*-type ground state. Such a *p*-type to *n*-type evolution of the bulk band with the play of a Cu atom is widely observed experimentally [6].

## 4 Conclusion

We conclude that the substitution of Cu in the pristine $Bi_2Te_3$ compound can harvest different carrier densities depending upon the position of the Cu atom in the crystal lattice. Our result highlights that the BB of the Cu-substituted $Bi_2Te_3$ has an enormous role in the electronic transport phenomena apart from the one played by the topologically non-trivial SS. Importantly, our study simulates the two most promising experimental features, viz. carrier type transition [6] and metallic ground state configuration [7] in the Cu substituted $Bi_2Te_3$ system.

## References

1. Hasan MZ, Kane CL (2010) Rev Mod Phy 82:3045
2. Chen C, He S, Weng H, Zhang W, Zhao L, Liu H et al (2012) Proc Natl Acad Sci 109:3694–3698
3. Tian W, Yu W, Shi J, Wang Y (2017) Materials 10:814
4. Sasaki S, Kriener M, Segawa K, Yada K, Tanaka Y, Sato M, Ando Y (2011) Phys Rev Lett 107:217001
5. Singh A, Kumar S, Singh M, Singh P, Singh R, ... & Chatterjee S (2020) J Phys: Condens Matter 32:305602
6. Wu HJ, Yen WT (2018) Acta Mater 157:33–41
7. Dan S, Kumar S, Dan S, Pal D, Patil S, Verma A, ... & Chatterjee S (2022) Appl Phys Lett 120:022105
8. Kresse G, Furthmüller J (1996) Comput Mater Sci 6:15–50
9. Perdew JP, Burke K, Ernzerhof M (1996) Phy. Rev. Lett. 77:3865

10. Li Y, Zou X, Li J, Zhou G (2014) J Chem Phys 140:124704
11. Sehr R, Testardi LR (1962) J Phys Chem Solid 23:1219–1224

# An Effective Way of Reducing the Wax Pattern Shrinkage to Improve the Dimensional Accuracy of the Investment Castings

Sarojrani Pattnaik and Mihir Kumar Sutar

**Abstract** In investment casting (IC) process, the properties of the disposable patterns are eventually transferred to the cast parts. In the present research work, disposable patterns made up of waxes are used to construct the moulds for casting. The wax patterns are easy to prepare and possess very good surface texture. But, they contract upon cooling, which causes dimensional variations in castings. An attempt has been made in this study to decrease the linear shrinkage of the wax pattern without affecting its surface texture by arresting its shrinkage characteristics by adding few materials such as filler and a resin, compatible to IC waxes. The materials chosen for the conduct of experiments are paraffin wax (40%), microcrystalline wax (10%), polyethylene wax (10%), starch powder (10%) and teraphenolic resin (30%). Further, the injection process parameters, namely, die temperature (DT), wax injection temperature (WIT) and holding time (HT) of the IC process are varied at three different levels and experiments are conducted as per Taguchi's L9 orthogonal array (OA) to determine the optimum input parametric levels. The results revealed that there was a considerable reduction (4.5%) in wax pattern linear shrinkage (PLS) by the aforementioned materials.

**Keywords** Investment casting · Wax · Resin · Process parameters

## 1 Introduction

The IC process, also known as precision casting technique is a widely known method around the world to produce dimensionally accurate metal parts bearing very good surface finish. The process utilises a sacrificial wax pattern for getting a hollow mould for casting and its characteristics are ultimately transferred to the cast parts [1–4]. The major employment of the IC process is in the manufacture of turbine blades and vanes

S. Pattnaik (✉) · M. K. Sutar
Mechanical Engineering Department, Veer Surendra Sai University of Technology, Burla, Odisha, India
e-mail: sarojrani07@gmail.com

cast in superalloys, which are used in aircraft industries [5–7]. The stages involved in the process are as follows: injection moulding of a disposable pattern, ceramic coating, dewaxing, drying and metal casting, followed by minor finishing operations [8]. The wax pattern should possess desirable properties such as low ash content, good surface finish, dimensional stability, environmental friendliness, unreactivity to the refractory mould, sufficient hardness to prevent breakage, etc. [9].

The operational effectiveness of the IC process can be enhanced by improving one or more aforementioned features of the wax patterns. The diverse IC waxes are of vegetable, animal, petroleum, mineral and synthetic types. The exploration by Solomon [10] disclosed that the patterns made from only waxes are deficient in strength and are dimensionally unstable due to solidification shrinkage during and after pattern injection from the mould/die. Horton [11] proposed that the wax pattern characteristics can be increased by the substitution of various substances called additives and fillers, since they have ring-structured carbon atoms, whereas the majority of the IC waxes are of straight-chained carbon atoms, and consequently, a strong link is formed amid them. Rezavand and Behravesh [12] established that the wax pattern characteristics are affected by wax blend composition and different wax injection process parameters such as the injection temperature, the injection pressure, the holding time, the die temperature, etc. However, selecting and varying all the process parameters simultaneously would complicate the entire process. Thus, a few essential process parameters should be chosen based on available literature on wax pattern making process for experimentation. Once process parameters are decided, subsequently, the best possible values of input process parameters should be determined to obtain the best results from it.

The present competitive situation requires a greater consideration of the dimensional accuracy and surface texture of the cast products. Since, the IC process commences with the construction of wax patterns, the feature of the constructed wax patterns directly affects the overall quality of the castings. In the present research work, an attempt has been made to decrease the linear shrinkage of the wax pattern without affecting its surface texture by arresting its shrinkage characteristics owing to the addition of few materials such as filler and a resin compatible to IC waxes.

## 2   Experimentation

Each chosen constituent influences the properties of the wax patterns in some way or the other. The materials chosen for constructing the wax patterns by injection moulding process were paraffin wax, microcrystalline wax, polyethylene wax, starch powder and teraphenolic resin. The percentage of filler i.e. starch powder in the mixture was fixed to 10%, whereas the percentage of other ingredients was varied as shown in Table 1. The wax blend was forced into a properly lubricated pre-heated metallic die using a wax injection machine. The PLS and SR were measured using a digital vernier callipers and surface profilometer. Initially, the experimentation was done at fixed input injection process parameters viz. DT = 40 °C, WIT = 70 °C and

**Table 1** Different wax blend composition

| Blend no. | Waxes (% wt.) | Resin (% wt.) | | Filler (% wt.) | |
|---|---|---|---|---|---|
| | Paraffin | Microcrystalline | Polyethylene | Teraphenolic | Starch powder |
| 1. | 40 | 15 | 15 | 20 | 10 |
| 2. | 40 | 10 | 10 | 30 | 10 |
| 3. | 50 | 10 | 10 | 20 | 10 |
| 4. | 50 | 10 | 5 | 25 | 10 |
| 5. | 60 | 10 | 10 | 10 | 10 |

**Table 2** Process parameters at diverse levels

| Process parameters | Unit | Range | Level 1 | Level 2 | Level 3 |
|---|---|---|---|---|---|
| DT | °C | 45–55 | 40 | 45 | 50 |
| WIT | °C | 70–80 | 70 | 75 | 80 |
| HT | Hour | 1–2 | 1.0 | 1.5 | 2.0 |

HT = 1 h to determine the optimum wax composition among the chosen blends. It was found that blend 2 demonstrated minimal PLS and SR. Thus, it was considered as the best wax blend amongst all and used for further experimentation in order to determine the optimal input wax injection process parameters.

The wax pattern characteristics are controlled by wax composition as well as wax injection process parameters such as die temperature, wax injection temperature, holding time, etc. In the first part of experimentation, only best wax composition has been determined. Thus, further, experiments are needed to determine the optimum input wax injection process parameters. The process parameters, namely, die temperature, wax injection temperature and holding time of the IC process were varied at three different levels and experiments were conducted as per Taguchi's L9 orthogonal array to determine the optimum parametric levels. The span of chosen input process parameters is shown in Table 2. The response of the process is pattern linear shrinkage. Figure 1 exhibits the wax patterns made as per L9 experimental runs.

## 3   Results and Discussions

The experimental results are depicted in Table 3. The wax patterns should possess least shrinkage. Thus, Taguchi's lower-the-better criteria has been chosen for computing the analysis of means (ANOM) to determine the optimal input parameter setting for the chosen response [13]. The ANOM for the response, PLS, is presented in Table 4 and the graph is depicted in Fig. 2. Delta is the difference between the highest and the lowest value of PLS obtained under each process parameter. Ranking is done on the basis of decreasing order of delta. From Table 4, it is obvious that the

**Fig. 1** Wax patterns made
by injection process



optimal input process parameters for obtaining least PLS are found to be DT at level
1 i.e. 40 °C, WIT at level 1 i.e. 70 °C and HT at level 3 i.e. 2 h. Wax injection temper-
ature is found to be the most important injection process parameter impacting the
pattern shrinkage. The second most influential process parameter is die temperature,
as it is ranked no. 2. It is seen that the optimum die temperature and wax injection
temperature is at the lowest level of chosen parameters. If these temperatures are
higher, then there are chances of wax leakage in-between the joints of the die-halves.
Also, more time is available for the pattern for shrinkage, as cooling rate decreases.
The dimensional constancy of the disposable wax pattern is affected by wax blend
constituents, injection temperature, die temperature, die holding time, surrounding
temperature, etc.

The lower the die and wax injection temperatures, the more the wax is in mushy
state. Thus, it solidifies soon with very little chance of thermal contraction. However,
the wax should not be too much in a semi-solid state that it could not able to flow
to the nook and corners of the die smoothly. It would adversely affect the shape as

**Table 3** Experimental results of wax patterns

| Sl. no | Input parameters | | | Response |
|--------|---------|----------|-----------|----------|
|        | DT (°C) | WIT (°C) | HT (Hour) | PLS (%)  |
| 1      | 40      | 70       | 1.0       | 2.65     |
| 2      | 45      | 70       | 1.5       | 2.74     |
| 3      | 50      | 70       | 2.0       | 2.79     |
| 4      | 40      | 75       | 1.5       | 2.71     |
| 5      | 45      | 75       | 2.0       | 2.83     |
| 6      | 50      | 75       | 1.0       | 3.08     |
| 7      | 40      | 80       | 2.0       | 2.94     |
| 8      | 45      | 80       | 1.0       | 3.11     |
| 9      | 50      | 80       | 1.5       | 3.42     |

**Table 4** ANOM table of PLS

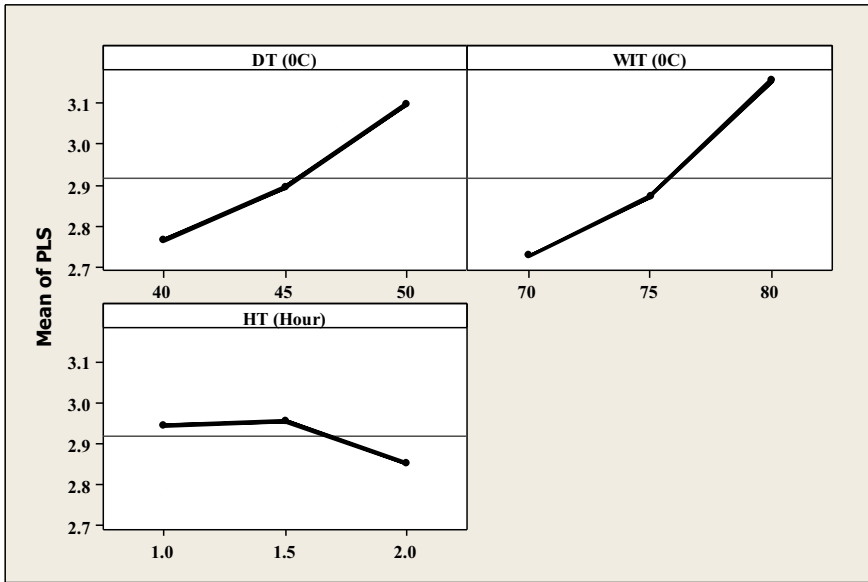| Level 1 | DT (°C) | WIT (°C) | HT (Hour) |
|---|---|---|---|
| 1 | **2.767** | **2.727** | 2.947 |
| 2 | 2.893 | 2.873 | 2.957 |
| 3 | 3.097 | 3.157 | **2.853** |
| Delta | 0.330 | 0.430 | 0.103 |
| Rank | 2 | 1 | 3 |



**Fig. 2** ANOM graph of PLS

well as the surface texture of the wax pattern. It is beneficial for the wax pattern to be at a higher holding time so that it is cooled properly inside the die and undergoes shrinkage to the fullest. It is clear from Table 4 that WIT is the most significant process parameter affecting the pattern shrinkage properties in the IC process, as it is ranked no. 1. It is followed by DT and the least significant process parameter is HT.

## 4 Confirmatory Experiments

The optimal input parametric setting i.e. WIT of 70 °C, DT of 40 °C and HT of 2 h is not found in the experimental run done as per L9 array in Table 3. Thus, there was a need to perform additional experiments at this obtained parametric setting.

**Table 5** Predicted and actual value of PLS of the wax patterns

| Optimal condition | PLS of wax patterns (%) |
| --- | --- |
| $WIT_1DT_1HT_3$ | 2.53 |

Three supplementary tests were done at the aforementioned parametric setting and the mean of the results are presented in Table 5. The least value of PLS seen in Table 3 is 2.65%. However, the PLS at the optimal condition is found to be 2.53%, which shows that there is a decrease of PLS further by 4.5% from the least value of Table 3, when the experiments are done at the obtained optimal setting. Thus, it can be said that the Taguchi predicted optimal setting is able to reduce the wax pattern shrinkage, thereby reducing the dimensional variations in castings.

The waxes chosen for this study are very cheaply and easily available throughout the world. Resins are added to provide strength to the IC waxes and thus, teraphenolic resin has been blended with the chosen waxes in the present study. The wax pattern shrinkage is unavoidable, but can be controlled or reduced to a maximum level. Literature reveals that fillers are added to restrict the wax pattern shrinkage and in this regard, starch powder has been mixed with selected waxes and resin. Ultimately, a combination of the chosen ingredients in the present study proved that it can be used as commercial pattern IC wax material worldwide, as it exhibited good pattern properties and this combination of ingredients has never been used before for investment casting. It is expected that this novel combination of wax mixture may be used by the investment casters for producing the shell moulds.

## 5 Conclusions

The conclusions drawn from the present study are as follows:

- Blend 2 containing 40% paraffin wax, 10% microcrystalline wax, 10% polyethylene, 30% teraphenolic and 10% starch powder is the best wax blend for pattern making producing least shrinkage.
- The Taguchi predicted optimal parametric setting was found to be WIT of 70 °C, DT of 40 °C and HT of 2 h.
- When the experiment was done at the obtained optimal setting, the wax pattern's linear shrinkage was further reduced by 4.5%.

## References

1. Pattnaik SR, Karunakar DB, Jha PK (2012) Developments in investment casting process-a review. J Mater Process Technol 212:2332–2348
2. Wang D, Sun J, Dong A (2019) Prediction of core deflection in wax injection for investment casting by using SVM and BPNN. Int J Adv Manuf Technol 101:2165–2173

3. Wei Q, Wang R, Xu Q (2018) Effects of process parameters on dimensional precision and tensile strength of wax patterns for investment casting by selective laser sintering. China Foundry 15:299–306
4. Pattnaik SR, Karunakar DB, Jha PK (2013) Multi-characteristic optimization of wax patterns in the investment casting process using grey–fuzzy logic. Int J Adv Manuf Technol 67:1577–1587
5. Li Y, Liu X, Lu K (2019) Preparation of fiber-reinforced shell by airflow placement fiber technology for investment casting. Int J Met Cast 13:979–986
6. Lu K, Duan Z, Liu X, Li Y (2019) Effects of fibre length and mixing routes on fibre reinforced shell for investment casting. Ceram Int 45(6):6925–6930
7. Pattnaik SR, Karunakar DB, Jha PK (2014) Utility-fuzzy-Taguchi based hybrid approach in investment casting process. Int J Interact Des Manuf 8:77–89
8. Pattnaik SR, Karunakar DB, Jha PK (2012) Optimization of multiple responses in the lost wax process using Taguchi method and grey relational analysis. Proc Inst Mech Eng Part L 227(2):156–167
9. Pattnaik SR (2017) An investigation on enhancing ceramic shell properties using naturally available additives. Int J Adv Manuf Technol 91:3061–3078
10. Kuo CC, Tasi YR, Chen MY (2021) Development of a cost-effective technique for batch production of precision wax patterns using 3D optical inspection and rapid tooling technologies. Int J Adv Manuf Technol 117:3211–3227
11. Wang D, Dong A, Zhu G (2019) Rapid casting of complex impeller based on 3D printing wax pattern and simulation optimization. Int J Adv Manuf Technol 100:2629–2635
12. Singh D, Singh R, Boparai KS (2018) Development and surface improvement of FDM pattern based investment casting of biomedical implants: a state of art review. J Manuf Process 31:80–95
13. Pattnaik S (2018) Investigation on controlling the process parameters for improving the quality of investment cast parts. J Braz Soc Mech Sci Eng 40:318

# Polarized Chitosan with Cu Substituted Hydroxyapatite Composite Exhibits Enhanced Osteogenicity and Antibacterial Efficacy In Vitro

**Subhasmita Swain, Priyabrata Swain, Sapna Mishra, and Tapash Rautray**

**Abstract** In order to obtain improved bone regeneration properties, copper-substituted inorganic bone filler implants can be utilized, in biomedical applications. There should be outstanding biocompatibility in conjunction with osteoconductivity to hasten the bone-repairing procedure. The primary objective of the ongoing study is to synthesize Chitosan (CS) with Cu substituted Hydroxyapatite (CuHA-CS) composites and the composites were electrically negatively polarized to be used as a biomedical implant material. The specimens were characterized to assess their behaviour towards biocompatibility and antibacterial properties. The composites were then cultured with MG-63 human osteoblast-like cells for studying their osteogenicity and *S. aureus* bacterial cells for understanding their antibacterial behaviour. It was inferred from the study that negative poled specimen of CuHA-CS structure improved the distribution of the osteoblast cells as well as augmented the antibacterial activities on the interface of the specimens possessing enhanced RUNX2, Osteocalcin, type-I collagen production on these specimens.

**Keywords** Hydroxyapatite · Polarization · Copper-substituted · Osteogenicity

## 1 Introduction

In the human body, the skeleton provides support and movement as well as protection for the soft tissues. The skeleton system is of scaffolding structure, comprized of bones. Bone is a living organ, possessing the capability of self-repairing (called

S. Swain · T. Rautray (✉)
Biomaterials and Tissue Regeneration Laboratory, Institute of Technical Education and Research, Siksha 'O' Anusandhan (Deemed to Be University), Bhubaneswar, Odisha 751030, India
e-mail: tapashrautray@soa.ac.in

P. Swain · S. Mishra
Depatment of Physics, Institute of Technical Education and Research, Siksha 'O' Anusandhan (Deemed to Be University), Bhubaneswar, Odisha 751030, India

bone remodeling). In the process of bone remodeling, osteoblasts, osteoclasts, and osteocytes work in harmony [1, 2].

However, bone fracture is very common. Various reasons for bone fractures, there exist several ways of fixating bone fractions. Our body is not structured to rebuild and repair the larger bone tissue damages lively itself. Thus by surgical intervention, the development of appropriate tissue engineering and enhancement of the tissue regeneration process took place. Bone grafting is a common technique to heal bone fractures. Also, there are bio-fillers and synthetic bio-implants [3, 4]. Bone is a hard tissue, a composite of 70% inorganic minerals like calcium, and phosphate, 22% protein, and 8% of water. Mostly we find calcium and phosphate in the bone as Hydroxyapatite (~70%) is a main inorganic compound of the enamel of teeth and natural bone tissues. Hydroxyapatite (HA) or (HAP) has the formula of $Ca_{10}(PO_4)_6(OH)_2$. The ideal molecular ratio of calcium and phosphorous in HAP is 1.67. HAP is a hexagonal lattice. It has a lattice constant of $a = 0.942$ nm and $c = 0.688$ nm. Hydroxyapatite is a bio-ceramic. It is a crucial biocompatible material and also a promising bone filler, and bio-cement [5, 6]. HAP is also non-inflammatory, non-toxic, and non-immunogenic. Due to its osteoconductivity, HAP is suitable for hard tissue replacements. Also, it has a similar composition and crystal structure to bone minerals.

Tri-component composites (i.e. binary blending of polymers with HAP) have good physiochemical, biological, and mechanical properties. Also, the composite (HAP-chitosan) (HAP-CS) should possess biodegradability and biocompatibility with osteoconductivity and osteoinductivity. Furthermore, the above bio-composites would exhibit better tensile strength. Gradually, these bio-composites help in the maturing of the bone matrix and are immune-deficient to the host body. CS is a well-known biopolymer and very compatible with HAP. CS is a very naturally derived polysaccharide and is also vastly used in the preparation of HAP composites as the polymer matrix. Also CS surface is hydrophilic in nature which promotes cell attachment and proliferation [7–9].

Though, HAP offers very low biocide activities and zero resistance to bacteria colonization on the implanted surface. In response to the infection filling failures, revision of surgery, and abscission of the operated limb asking for high medical expenditures happen. Henceforth to avoid these and the initial bacteria colonization, it is preferable to use additional antibacterial metal ions such as $Zn^{2+}$ or $Cu^{2+}$ ions, as a substitute for Ca ion in HAP [10]. Copper is widely known for its wide-ranging spectrum of antibacterial activities and also are used in vari ous medical fields. Moreover, copper is toxic in nature. Copper in quantity is necessary for the metabolic process. Copper-substituted HAP-CS will bear the chemical sign of Cu-HAP-CS. These doping metal ions manifest antibacterial activities and also these are not cytotoxic at a lower concentration [11, 12].

The polymerized metal-ion substituted HAP has improved ultimate tensile strength and Young's modulus. Natural bones exhibit piezoelectricity and response to external mechanical stress. To induce piezoelectric character, we need to polarize the synthetic hydroxyapatite. For the development of HAP-based bio-composites

with adapted adherence and adsorption, surface modifications are doable like Polarization, by the use of osteogenic cells along with various physiochemical approaches including the fabrication of spongy HAP ceramics. Biphasic calcium phosphate, and growth factors (i.e. bone morphogenetic protein) are added to enhance the osteoconductivity of fabricated HAP. Out of all these, static charge stored within the polarized HAP gives exceptionally good and phenomenal biological responses. By lab works it's seen that genesis of supplemented bone-like apatite takes place on the negative charge polarized HAP surface and contrastingly positive charge polarized surface hinder apatite formation. As per Ohgaki et al., cohesion and proliferation of osteoblasts happen on negatively activated polarized HAP surfaces. By these studies, it is obvious that the actions of cells on the Hydroxyapatite surface may be adapted to the intense charge-storing capability of the polarized Hydroxyapatite [13, 14].

## 2 Materials and Methods

Calcium nitrate tetra-hydrate [$Ca(NO_3)_2 \cdot 4H_2O$, 99%], Diammonium hydrogen phosphate purified [$(NH_4)_2HPO_4$, 99%], Copper (II) nitrate tri-hydrate purified [$Cu(NO_3)_2 \cdot 3H_2O$], also known as cupric nitrate, along with Ammonium hydroxide ($NH_4OH$), the analytical level chemicals are being used in this experiment.

### 2.1 Preparation of Copper-Substituted Hydroxyapatite

Supported by the wet chemicals precipitations technique, copper-substituted Hydroxyapatite (CuHAP) nanoparticles were synthesized. The needed amount of [$Ca(NO_3)_2 \cdot 4H_2O$] and [$Cu(NO_3)_2 \cdot 3H_2O$] along with the molar ratios of Cu/(Ca + Cu), 0 to 1 were dissolved in the deionized or demineralized water. $(NH_4)_2HPO_4$ was added to the solution drip by drip, subsequently under magnetic stirring. The solution was morphed to milk-white or cloudy white, and pH was adjusted to approx. 10 for the final solution with the help of $NH_3OH$ drip by drip. Later on, the final solution was heated to 70 °C for about 2 h, and with continuous stirring, 24 h of aging took place. Also, subsequent washing of the collected sample precipitated with filtration and was dried at 60 °C. By grinding and calcination at 700 °C for 3 h, the final powdered form was retrieved.

### 2.2 Preparation of CuHAP-CS Composites

To 100 ml of 10% acetic acid medium, 1 g of CS nano-powder was added. In the CS solution (4 g), CuHAP (1 g) was added, followed by continuous blending for 10 h. The homogenous solution was then kept inside of the mold of thickness and

radius 2 mm and 6 mm respectively. The mixture was frozen for 5 h at −20 °C. The solidified mixture was dried in a freeze dryer at a temperature of 35–60 °C for 36 h. Ultimately the CuHAP/CS composite was treated with an $NH_3OH$ solution. Washing and later drying at 60 °C was processed.

## 2.3 Polarization of Composites

The samples were covered with silver on either side and polarized with a negative electric field at 2 kV/mm polarizing voltage and temperature of 550 °C. Later, the silver coating was removed, and both sides were rubbed down with 400-grit emery paper. After that, to ensure there is no trace of silver particles, the specimens were quantitatively evaluated by EDX (Energy Dispersive X-ray fluorescence spectroscopic procedure) [5].

## 2.4 Characterization of Composite Samples

### 2.4.1 X-Ray Diffraction

Phase analysis of sintered CuHAP composite sample was performed using the X-ray diffraction (XRD) technique with a stepwise scan by X-ray diffractometer using Cu Kα radiation (λ ~ 1.541874 Å) at 40 kV and 20 mA in the $2\theta$ range between 20° and 80°.

### 2.4.2 Thermally Stimulated Depolarization Current (TSDC)

To estimate static stored charge by polarization, the sample was treated with TSDC. Both the negatively polarized and unpolarized composite samples were heated at a rate of 5 °C/min, up to 550 °C and TSDC, measured by a Pico ammeter (Keithley 6487). Stored electrical charges were measured by TSDC spectrum by,

$$Q_p = \frac{1}{\beta} \int J(T) dT$$

Here,

$Q_p$—Density of stored charge,

$\beta$—Rate of heating,

$J(T)$—Density of current.

### 2.4.3 Contact Angle Measurement

The water-wetting angle of the specimens was measured by a contact angle measurement system (OPTIMA VCA). SBF (simulated body fluid), and DMEM (Dulbecco's Modified Eagle's Medium) at pH 7.4 were used to find the wettability of the specimens.

### 2.4.4 Ion Releasing

In CuHAP-CS composites, the ion release properties were estimated by dipping 0.5 g of specimen in 50 mL of SBF. The concentration of $Cu^{2+}$ and $Ca^{2+}$ ions in the simulated body fluid was quantified at different periods using an inductively coupled plasma/optical emission spectrometer (OPTIMA 3300DV, ICP/OES).

### 2.4.5 In Vitro Study

For both the negatively polarized and unpolarized composite samples, in vitro study has been evaluated. Polarized composite samples (at 550 °C) were used for in vitro inspection while an unpolarized sample was used as a control in all our observations.

### 2.4.6 Cell Culture

The MG63 osteoblast-like cells (i.e., ATCC, CRL-1427) were nurtured in DMEM; GIBCO along with Penicillin (100units m/L), 10% of Fetal bovine serum (FBS) was incubated at 37 °C with atmospheric $CO_2$, 5%. For removing the adhered cells, the cultured media were changed. The MG63 of the fifth and seventh passages were used for the leading observations.

### 2.4.7 Cell Proliferation by Using MTT Assay

MTT assay [3-(4,5-dimethylthiazol-2-yl)-2,5-didiphenyltetrazolium bromide] was carried out for 1, 3 and 5 days of culture to find out the proliferation of MG63 cells on both the negatively polarized and unpolarized surfaces. Three specimens from each were taken and triplicate data points were taken from each specimen. An MTT solution of 5 mg/ml was prepared and filtered after sterilization. The solution of MTT was diluted in DMEM culture media supplemented with 10% fetal bovine serum (Dilution ~50 µl into 450 µl). Then to each sample in 24 well plates, 500 µl diluted MTT solution was added.

### 2.4.8   Osteogenic Gene Expression

In accordance to observe the mRNA expression of osteogenic genes, such as OCN ( BGLAP or osteocalcin), RUNX2 (Runt related transcription factor II), and Col-1 (type-II collagen, cell differentiation of MG63 osteogenic cells were carried out on both negative poled as well as unpoled samples with help of Bio-rad MyiQ2 system. Each cell was embedded with a density of $4 \times 10^4$ cells, cultured for 2 weeks, and later lysed by using Tirol (an INVITROGEN) to extract RNA and the RNA was reverse transcribed into cDNA using the Superscript II first-strand cDNA synthesis (Thermo) kit [15].

### 2.4.9   Antibacterial Activities Check

MTT assay was carried forward in accordance to observe the in vitro bacterial viability of CuHAP-CS specimen on the gram-positive S. aureus cells. These cells were treated in a Muller–Hinton Broth (MHB) for 6 h under 37 °C temperature, with a concentration of $1 \times 10^6$ CFU/mL. These composites were then separately kept in a $CO_2$ incubator with 1 mL of microbial cell suspension at the same temperature in the center of a 24-well plate. After 10, 20, and 30 h, the bacteria cell culture was observed. Each of the bacterial suspensions was mixed with 150 μL MTT solution. Later than that, the adherent cells were conducted for bacterial viability. Each test was carried out on a triplicate basis. The microbial viability was observed by monitoring the OD measures of the composite samples [16].

## 3   Results

In the ongoing experiment, the crystal structure of composed samples was carried out with the help of XRD characterization (Fig. 1). With a trace amount of impurities, pure phase CuHAP was obtained. At 550 °C i.e. at the highest temperature, it was found that 4.7 nA/cm$^2$ was the observed current density and at 522 °C, 5.07 nA/cm$^2$ was the maximum observed current density of negative poled CuHAP-CS specimen according to TSDC results (Fig. 2). Measurement of stored charge on the interface were carried out with the help of depolarization of polarized composited as depicted in Table 1. Figure 3 depicts the SEM micrograph of (a) CuHAP and (b) CuHAP-CS specimens.

### 3.1   Contact Angle Measurement

Figure 4 depicts the contact angles of two different aqueous media (DMEM and SBF) measured on negatively polarized and unpoled CuHAP-CS composite. In both

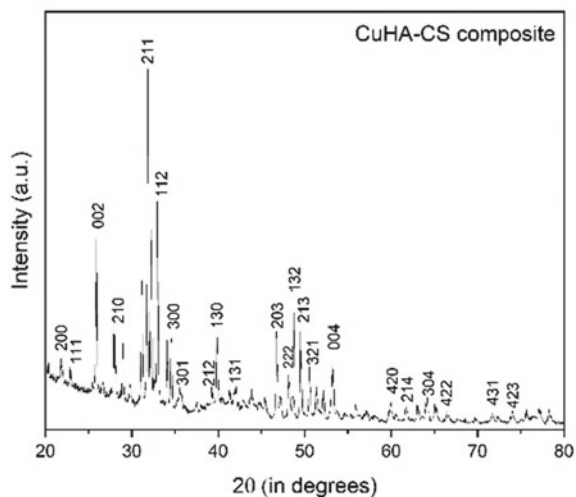**Fig. 1** XRD pattern depicting CuHA-CS composite



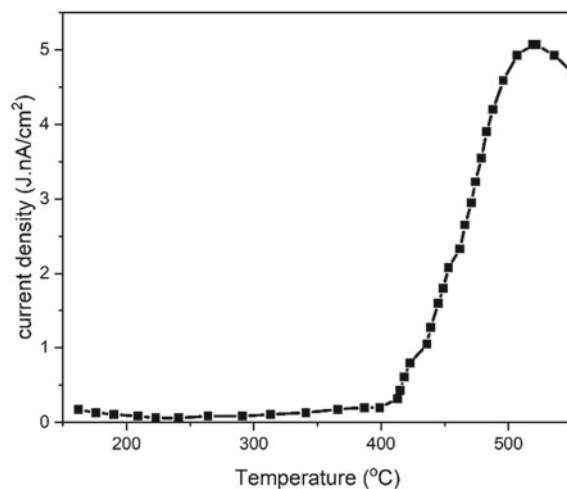**Fig. 2** TSDC thermogram of composite sample



**Table 1** Calculated stored charge and maximum current density different outcomes of from depolarization of CuHA-chitosan composite

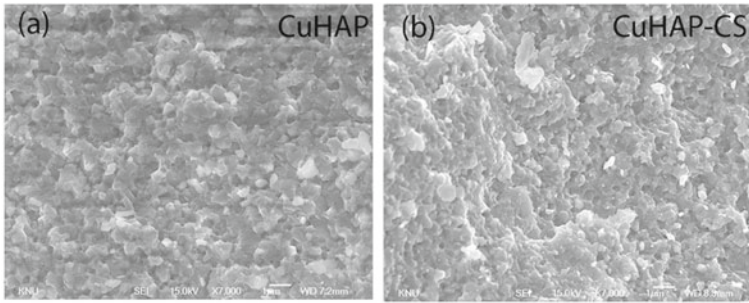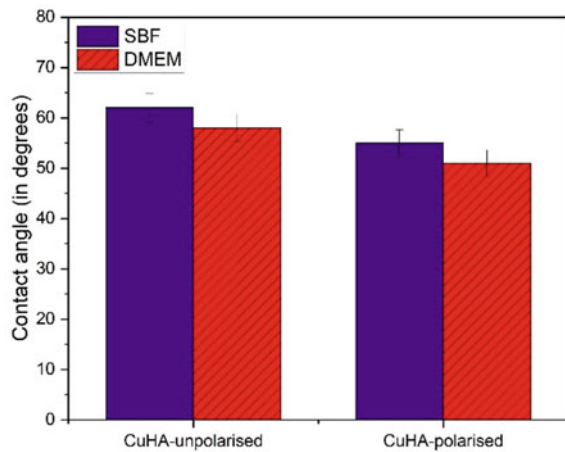| Polarization condition | Sintering atmosphere | Maximum current density (nA/cm$^2$) | Stored charge ($Q_p$) ($\mu$C/cm$^2$) |
|---|---|---|---|
| $T_p = 550$ °C, $E_p = 2.0$ kV/cm, $t_p = 1.0$ h | Air | 5.07 | 4.7 |

**Fig. 3** **a** SEM micrograph of CuHAp and **b** CuHAP-CS specimen



**Fig. 4** Contact angle of CuHA-CS negatively polarized and unpolarized specimens with SBF and DMEM media

DMEM and SBF media, negatively polarized composite exhibited lesser contact angles than the unpoled ones. It can be seen that cell media (DMEM) contact angles on 450 °C negatively polarized CuHA-chitosan composite is as low as $51° \pm 2.59$ while it was found to be $55° \pm 2.64$ for SBF. Whereas, the contact angle of SBF and DMEM were measured to be $62° \pm 2.88$ and $58° \pm 2.68$ for unpolarized CuHAP-CS composite respectively.

## 3.2 Ion Release

Gradually, the Cu ions released from the composite may stimulate the antimicrobial action on the surface of the composite. In the present study, the ion-releasing property of CuHAP-CS composite was carried out by dipping the composite in SBF at 37 °C and checking the ion concentrations in different intervals of periods by PIXE. $Cu^{2+}$ ions are released from the CuHAP-CS composite and the concentrations reach
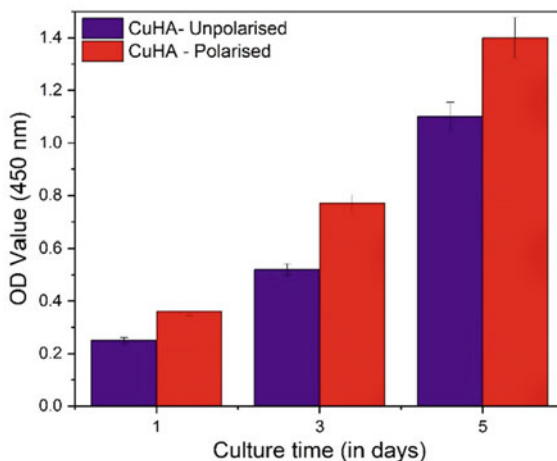
26 ppm after 12 h which is an acceptable limit of Cu release in the wound site
[17]. The released $Cu^{2+}$ ions can improve the antibacterial effect of the CuHAP-CS
composite [18].

## 3.3 MTT Assay

MG63 cell proliferating rate on either of the negatively polarized and unpolarized
CuHAP-CS composite was studied with the help of MTT assay. Figure 5 indicates a
comparison of cell density for both samples after 1, 3 and 5 days in culture. Appar-
ently, on days 1 and 3, cells proliferated rapidly on a negatively polarized CuHAP-CS
composite surface compared to an unpolarized CuHAP-CS composite surface. On
day 5, a noticeable difference in OD was observed between negatively polarized
CuHAP-CS composite and unpolarized composite surfaces. Cells grew on nega-
tively polarized CuHA-chitosan composite about 1.2 times more than the unpolarized
composite surface. Statistical analysis revealed that significant differences ($P$ value
<0.05) in cellular densities are there between the negatively polarized CuHAP-CS
composite and unpolarized composite surfaces for all cultured durations.

## 3.4 Osteogenic Gene Expression

The osteogenic gene expression of RUNX2, OCN, and COL-1, were quantified by
qRTPCR set up and the data obtained is shown in Fig. 6, Fig. 7 and Fig. 8 respectively.
This polarized specimen surface exhibited better gene expression grades. Moreover,
negatively polarized surfaces showed elevated levels of mRNA for every osteogenic

**Fig. 6** Osteogenic
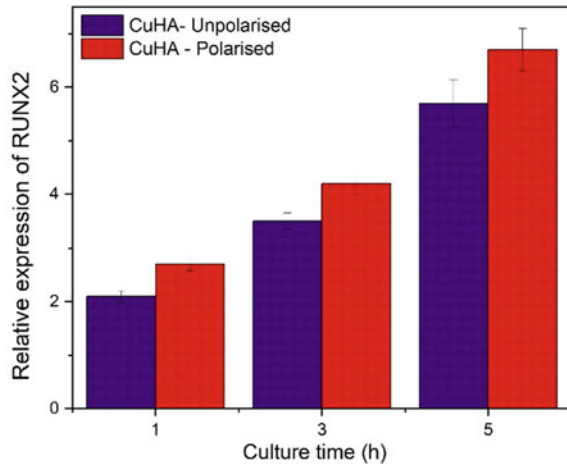expression of RUNX2 on the
composite specimens



**Fig. 7** Osteogenic
expression of OCN on the
composite specimens
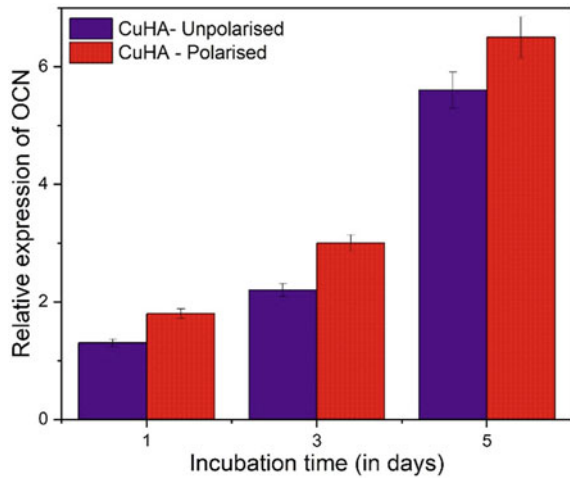


gene. The peak mRNA level was observed on negatively polarized CuHAP-CS
composite in supporting MG63 cell division.

## 3.5  Antibacterial Activity

*S. aureus* bacterial growth was studied using OD measurements at 490 nm. The
data were measured every 10 h till 30 h. For each type of bacteria, its behaviour
and growth were observed, in the presence of a negatively polarized composite as
compared to an unpolarized composite. Figure 9 shows that the number of cells

**Fig. 8** Osteogenic expression of Col1 on the composite specimens
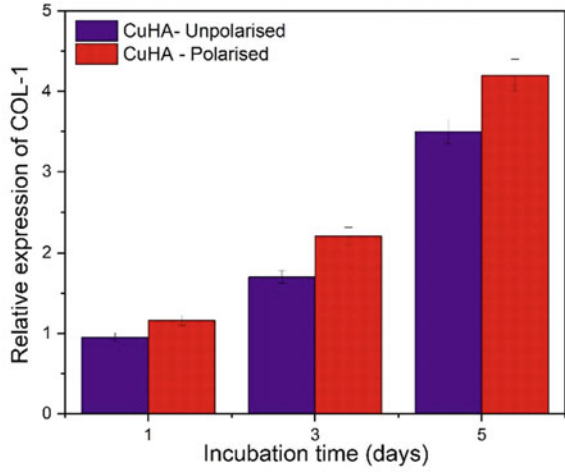


slightly decreases in the negatively polarized composite. The results indicate that the copper nullifies a portion of the bacterial colony in the unpolarized composite. But, abnormal bacterial behaviour and growth were controlled and prevented in the negatively polarized composite.

**Fig. 9** Bacterial viability of *S. Aureus* on the composite specimens
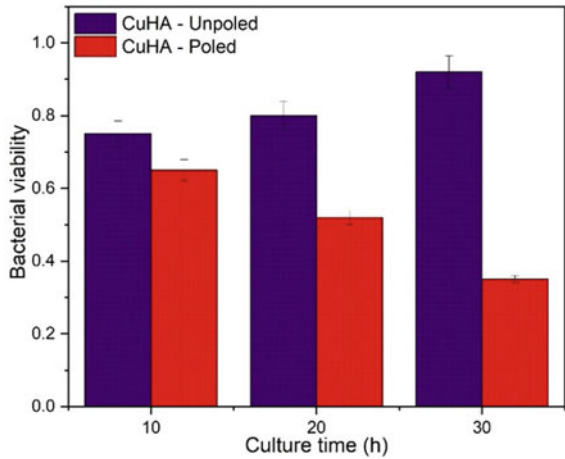
## 4 Discussion

The prime ambition of the scrutiny was to check the bio-affinity of polarized CuHAP-CS composites. Outstanding results of osteoblast proliferation, gene expression and antimicrobial activities were noticed on negatively polarized CuHAP-CS composite as compared to unpolarized CuHAP-CS composite. Based on these outcomes, the application of the negatively polarized CuHAP-CS composite may be tried for in vivo evaluation to understand its effectiveness in animal models.

The mechanisms of the polarized CuHAP aren't completely understood in the way it kills the bacteria. Ueshima et al. put forward a supportable poling prototype and mechanism for HAP. At a lower temperature (<400 °C), in the columniformed channels (OH$^-$) of HAP's hexagonal unit cell movements of protons (H$^+$) causes the polarization of HAP [19]. Also at a higher temperature (>500 °C), fragmentary desiccation of HAP and fragmentary diffusion of $O_2$ may take place with the H$^+$ movement. In the present study, the poling temperature was 550 °C, we presumed fragmentary desiccation of HAP and fragmentary diffusion of $O_2$. For the polarization of electrostatic charge storage, the CuHAP-CS with an average density of 90–91% was used in our study. As commonly known, many factors such as derived electric field, porosity, purity of phase and temperature of poling affect the CuHAP polarizability. From the discharge of the de-polarization current, it was found that CuHAP-CS at an increased temperature pointed to the polarisability of substituted HAP. At a polarization temperature of 522 °C, the highest current density of 5.07 nA/cm$^2$ was obtained. It shows that greater polarization could be possibly reached by rising the temperature. Nakamura et al. proposed, HAP compact with a higher relative density of 97% may have a charge density as high as $18 \mu C \, cm^{-2}$ as compared to our data of CuHAP-CS with an average density of 90–91% of CuHAP [20, 21].

Regeneration of tissue is a complicated procedure including consequent cellular actions. Adherence of cells is the primary step, along with cell proliferation, differentiation and maturing of the tissue. Adherence of the cell with substratum is arbitrated by protein surface assimilation on the surface of the material, allied with wettability, topography and chemistry. According to the present data, there is an enhanced proliferation rate of MG63 osteoblasts on negatively polarized CuHAP-CS composite as compared to unpolarized CuHAP-CS composite. Negatively polarized CuHAP-CS composite has the lowest contact angle in both DMEM and SBF media, due to its higher hydrophilicity and hydrogen bonding capability that can occur on the surface of this composite between free OH groups and $H_2O$ molecules [22, 23].

Unpolarized CuHAP-CS composite possesses the maximum contact angle as it is more hydrophobic in nature than the polarized ones. The wettability of biomaterials influences adherence, cellular proliferation and differentiation. Moreover, the contact angle decreased when there is an increment in the surface charge stored. As per the recent results, the wettability of CuHAP-CS composite varies along with surface charge without imparting any volumetric influences such as chemical treatment [24].

From the MTT assay study, the MG63 cell survival rates were estimated which shows the presence of copper ions having cytotoxicity at the beginning. However,

on day 7, the cell survival rate of the negatively active CuHAP-CS composite was remarkably higher than that of the unpolarized CuHAP-CS composite. It is showing that polarization of composites has enhanced results on the proliferation of MG63 cells and it inhibits the bacterial growth of *S. aureus*.

Cell proliferation, extracellular matrix maturing and mineralization are the three main phases of bone formation or development. Collagen (Col1) release enhances with prior osteoblast differentiation (osteogenic). RUNX2 is the dominant transcriptase factor for prior osteoblast differentiation. Since chitosan has been originated from the hard shells of crustaceans, it has bio-affinity and biodegradability that enhances the adherence together with Col1 and osteocalcin. In osteoblast differentiation, Osteocalcin is a late marker. Similarly, the beginning of ECM deposition starts progressively.

In the CuHAP-CS composite, influences of Cu ions on the antibacterial activities were carried out by using *S. aureus* bacteria. From the results, it was summarized that the composites with negative polarization possess greater antimicrobial efficacy than the unpoled ones, and this is achieved due to the antimicrobial property of Cu for which the interaction of the Cu ion with the bacterial membrane causes structural deformity of the membrane thus killing the bacteria. Polarization is crucial to rupture the bacterial cell membrane with an exterior electric field, inclusive of its exposure time, and pulse timespan (pulsed-field) [13]. The cause of death of bacteria may be due to the electrolysis of molecules on the bacteria cell membrane, giving rise to toxins like hydrogen peroxides, chloride molecules and oxidizing radicals.

## 5   Conclusion

The formation of pure phase CuHAP was attributed to the help of XRD characterization. Moreover, $496°$ C was the highest current density as observed from TSDC results. In comparison with unpolarized CuHAP-CS composites, enhanced osteogenicity and better antibacterial efficacy were found in negatively poled counterparts. Additionally, negatively polarized CuHAP-CS composites possess remarkably greater osteogenicity on day 5, as found from osteogenic gene expression results. Therefore, negative poled CuHAP-CS composites can be a better substitute for bone regeneration applications, that induce osteogenicity along with antibacterial properties.

## References

1. Rautray TR, Narayanan R, Kim KH (2011) Prog Mater Sci 56:1137–1177
2. Swain S, Rautray TR, Swain BP (2021) nanostructure materials and their applications. Springer, Singapore, pp 55–80
3. Kim KH, Rautray TR, Narayanan R (2010) surface modification of titanium for biomaterial applications. Nova Science Publishers, Korea

4. Swain S, Misra RD, You CK, Rautray TR (2021) Mater Technol 36:393–399
5. Swain S, Padhy RN, Rautray TR (2020) J Korean Ceram Soc 57:495–502
6. Swain S, Ong JL, Narayanan R, Rautray TR (2021) J Biomed Mater Res B: Appl Biomater 109:2154–2161
7. Pighinelli L (2013) Kucharska. Carbohydr Polym 93:256–262
8. Baino F, Novajra G, Vitale C-Brovarone (2015) Front Bioeng Biotechnol 3:202
9. Deville S, Saiz E, Nalla RK, Tomsia AP (2006) Adv Sci Technol 49:148–152
10. Xie H, Kang YJ (2009) Curr Med Chem 16:1304–1314
11. Grass G, Rensing C, Solioz M (2011) Appl Environ Microbiol 77:1541–1547
12. Turski ML, Thiele DJ, Biol J (2009) Chem 284:717–721
13. Swain S, Padhy RN, Rautray TR (2020) Mater Chem Phys 239:122002
14. Tourani H, Molazemhosseini A, Khavandi A, Mirdamadi S, Shokrgozar MA, Mehrjo M (2013) Polym Compos 34:1961–1969
15. SwainS BowenC (2021) Rautray T R. J Biomed Mater Res A 109:2027–2035
16. Swain S, Rautray TR (2020) Biol Trace Elem Res 199:1185–1193
17. Institute of Medicine, Food and Nutrition Board (2001) Dietary Reference Intakes for Vitamin A, Vitamin K, Arsenic, Boron, Chromium, Copper, Iodine, Iron, Manganese, Molybdenum, Nickel, Silicon, Vanadium, and Zinc. National Academies Press, Washington, DC
18. Grass G, Rensing C, Solioz M (2011) Appl Environ Microbiol 77(5):1541–1547
19. Ueshina M, Nakamura S, Yamashita K (2002) Adv Mater 14:591–595
20. Gittings JP, Bowen CR, Turner IG, Baxter FR, Chaudhuri JB (2008) Mater Sci Forum 587–588:91–95
21. Nakamura S, Takeda H, Yamashita K (2001) J Appl Phys 10:5386–5392
22. Li M, He P, Wu Y et al (2016) Sci Rep 6:32323
23. Shiting L, Hui K, Naihui Y et al (2011) Biochem Biophys Res Commun 410:698–704
24. Zhou J, Li B, Lu S, Zhang L, Han Y (2013) ACS Appl Mater Interfaces 5:5358–5365

# Self-lubricating Composite: A New Generation Metal Metrix Composite for Efficient Tribological Application

**Sweta Rani Biswal and Seshadev Sahoo**

**Abstract**  In a highly developed contemporary society, transport, power generation, and production are essential industrial activities associated with movable machinery and moving mechanical structures. The major concern of those machineries is associated with frictional loss. Controlling friction parameters is associated with the choice of materials used for manufacturing of those parts and so as the systems. This article provides an overview of the tribological performance of advanced functional materials. With ultra-high strength and wear resistance combinations, self-lubrification micro and nano-composites in metallic matrixes will improve the energy efficiency, system reliability, operational comfort, repair capability, and protection dissolve the challenges and opportunities occurred in the tribological applications. Evolution in the field of fabrication technology opens up many ways to develop new age self-lubricating materials with the addition of two-dimensional (2D) solid lubricants like graphite, dichalcogenides like molybdenum disulfide, tungsten disulfide, etc. which are the key aspects of this study. This study also represents the challenges and future prospects of the application of different types of self-lubricating composite. This article helps to find new gateways for fabricating composites with different combination of reinforcements.

**Keywords**  Self-lubricating composite · Solid lubricant · Automotive · MMCs

## 1  Introduction

Viewing today's scenario, environmental and energy issues and global survival has become extremely serious. Resolution of these problems is a matter of great importance for researchers in all fields. In the twenty-first century, the real catalyst for developing the modern tribology discipline was the great economic effect due to wear failures. At the same time, a large number of new technical solutions were

S. R. Biswal (✉) · S. Sahoo
Department of Mechanical Engineering, Institute of Technical Education and Research, Siksha 'O' Anusandhan (Deemed to be University), Bhubaneswar 751030, Odisha, India
e-mail: swetaranibiswal@soa.ac.in

introduced to minimize friction and wear but were still not applied to a large extent. As per many researchers, green tribology should play a key role to resolve several global energies, environmental, and resource problems where advanced functional materials are vital [1]. With this rationale in mind, the recent boom is associated with technology in the field of production and development of mechanical systems, which even includes the fields of tribology and tribo-technology.

Any application where rubbing takes place requires lubrication to avoid excess wear, accumulation of heat, seizure, and—in the worst-case—total failure of the device. As per the study, a proper mechanical system lubrication will create a design or destroy it. Taking this into account, weight liability currently requires advanced functional materials that can perform more than just their primary purpose. The possibilities in MMCs are examples of self-healing and self-lubricating materials. Self-lubricating type composites not only solve the problem of lubrication but also eradicate the use of an external lubrication supply enabling manufacturers to develop rubbing items where there is an uncomfortable or an unlikely presence of lubrication. The increased demand for self-lubricating composites will lead to market expansion and the production of lower-cost processing methods to reduce costs. It is also anticipated that the integration of various capabilities into one material would save weight. As Self-lubricant materials can work without external lubrication, they can be used for cylinder liners, pistons, CV joints, gears, and sliding surfaces, and more automotive applications. To achieve the self-lubricating property in micro and nano MMCs, solid lubricants like graphite, and dichalcogenides as reinforcement have been added [2].

This type of composite has recently gained considerable interest in various applications and it seems like they have enormous potential, but few researchers have acquired this inferior characteristic to traditional alloys that are likely to be derived from agglomeration, particle migration into grain limits, and porosity. To study these issues and draw quantitative findings on the effect of different parameters on self-lubricating composite characteristics, systematic research is needed. This article explains the features of self-lubricating composites and its applications for analysis. The emphasis of this study dealt with self-lubricating composite development with solid reinforcements. The research will provide an overview of solid lubricant's impact on tribological behavior of the composite. This study also focuses on challenges and future scope in the various industries to produce frictionless mechanical components.

## 2   Tribological Aspects of Self-lubricating Composites

The self-lubricating composites demand enhanced stiffness, the strength of wear, and a low coefficient of friction (COF). These features improve automotive application and tribological aspects in the composites. Several methods have been developed to boost the alloy tribological aspects, including morphological alterations, use of reinforcement, and changing surface. Reinforcing solid lubricants in MMCs is the

best among them. The trend to use solid lubricants in a variety of applications has been developing over the last few years.

Self-lubricating materials are those groups of materials which lubricate themselves. These are developed to be used in severe environmental conditions which do not require enough liquid lubrication to provide improved efficiency. As in those environments, Liquid lubricants like oils and greases can function as pollutants. The addition of solid lubricant provides dry lubrication and can be the only possible solution in these circumstances. MMCs are also formed by adding Solid lubricants in the form of films or scattered into bulk. But as films, lubrication depends upon its thickness. So, the best possible solution for inducing self-lubricating properties is to allow solid lubricant in bulk form reinforced into the alloy [3].

The development of self-lubricating composite has been proposed for low friction and wear without external lubrication supply. There are several ways to manufacture composite metal matrices. However, the key problems are the weakness and the dispersion of the solid lubricants with the matrix alloy. This condition was dealt with in several ways. Mixing, consolidation, vapor deposition, stir casting, the technique of pressure penetration, and the method of deposition. The most simple and economical method, however, is stir casting [4]. But due to the agglomeration of particles and reaction of solid lubricants with matrix during melting which causes the degradation in mechanical properties, P/M is adopted for many decades as an important fabrication route for the manufacture of self-lubricating composites. Through Powder Metallurgy, homogenous structures of solid lubricant particles can be achieved. Various solid lubricants such as graphite, hBN, $MoS_2$, $WS_2$, $MoSe_2$, etc. can be introduced into the metallic or ceramic matrix to induce self-lubricating properties. At high volume (up to 40 vol%), addition of solid lubricants decreases the matrix continuity degree, hampering mechanical proprieties and thus limiting the application of composites despite the reduction of the friction coefficient.

Certain high-performance iron-based composites for self-lubrication have been established in the last decade as a potential combination solution of low COF at increased mechanical strength and wear resistance [5]. Furlan et al. [6] provide a complicated connection between the solid lubricant powder particle, sintering temperature, solid lubricant form, and quantity inside the structure, as well as the COF and wear. According to the Metallurgical point of view, it is feasible to fabricate iron-based self-lubricating composites containing graphite and $MoS_2$ as solid lubricants, which has a synergistic impact, which provides low friction and wear rates in various atmospheres ($N_2$ and air). As per the report by Moazami–Goudarzi et al. [7] whatever the standard load applied, both COF and wear loss were reduced to a critical level till 2.5 vol% addition of $MoS_2$ material to Cu matrix. The formation of an intact $MoS_2$ lubricant foil on the composite surface was responsible for this. However, higher $MoS_2$ contents have been used to lower the wear resistance because the material's stiffness has been reduced. Increased normal load in wear tests has also been verified, leading to decreased friction coefficients regardless of $MoS_2$ volume fraction. A high $MoS_2$ (20–40% volume fraction) has been added to copper alloys that have led to very high wear rates.

Graphite reinforced self-lubricating composites have better wear-resistant and minimum COF at low cost. Advancement in the area of nanotechnology leads to the manufacture of self-lubricating composite with single-dimensional carbon nanotube and two-dimensional graph nanosheets addition. The addition of carbon-based nanomaterials enhances materials' specific electric, mechanical, thermal and tribological characteristics in metal matrices such as aluminum, magnesium and transition metal composites. These are attractive reinforcements in lightweight, high-fast, and high-performance metal matrix composites [8]. Many types of research show that Al + CNT and Al + graphene composites have substantially greater tribological properties than Al with graphite addition which is also true for Cu matrix.

In comparison with graphite and $MoS_2$, hexagonal boron nitride (hBN) has special lubricant properties that have better thermal stability. hBN offers an excellent chance to create self-lubricating composite material for the automotive sector [9]. Moorthy et al. [4] described the effect of hBN on dry wear. The accumulation in the matrix of both fly ash and hBN particles increases aluminum composite wear resistance. Also at higher loads, 4 wt% of hBN had better lubricity and at interfaces, hBN was formed with a highly worn surface, which played a promising role in reducing the COF and the wear rate. Wozniak et al. [10] manufactured an auto lubricating AA6061 matrix with a variety of graphene, $MoS_2$, and hBN weight fractions through powder metallurgy. $WS_2$ is a good solid lubricant that has very weak van der Waals forces because of its lamellar crystal structure. Therefore, it is rather simple to slide between layers which give the composite a very low friction coefficient. Many self-lubricating composite metal matrices have been prepared, such as AgCu, Al, Cu, and Mg, reinforced with $WS_2$ which have improved tribological efficiency. $WS_2$ was combined with other solid lubricants, such as $MoS_2$-graphite, in MMCs in order to broaden the effective range of work. Generally, Powder metallurgy, a fabrication method used to manufacture self-lubricating composites based on $WS_2$.

There have been, unfortunately, very few studies to show $WS_2$ decomposition mechanism and its effect on tribological properties during preparation [11–14]. The researchers have discovered the greater impact of solid lubricant on tribological behavior of self-lubricating composites which is well explained through a comparative analysis on solid lubricants reinforcements mentioned in Table 1. The wear track images of different solid lubricant reinforced hybrid composites are represented in Fig. 1.

## 3   Current Potential Applications, Challenges, and Its Perspective

The fundamental mechanisms of the tribological phenomenon have been considerably understood, along with the development of numerous self-lubricating materials, and solid lubricants. New technological solutions such as new fabrication methods, and additives (including nanomaterials and solid lubricants); not only open up a new

**Table 1** Comparative analysis on wear properties of self-lubricating composite

| Matrix | Solid lubricant | Minimum wear parameter [load] | Optimum COF/wear rate | References |
|--------|-----------------|-------------------------------|-----------------------|------------|
| Al | h-BN | 30 N | 0.1, 0.059 mm$^3$ m$^{-1}$ | [4] |
| Fe | MoS$_2$, graphite | 7 N | 0.08 and $8 \times 10^{-6}$ mm$^3$ N$^{-1}$ m$^{-1}$ | [6] |
| Cu | MoS$_2$ | 4 N | 0.21 | [7] |
| Al | h-BN | 24.5 N | 0.22 | [9] |
| Al | h-BN | 10 N | 0.42, $120 \times 10^{-2}$ mm$^3$ m$^{-1}$ | [10] |
| Cu | WS$_2$ | 10 N | 0.2, $2 \times 10^{-5}$ mm$^3$ N$^{-1}$ m$^{-1}$ | [11] |
| Cu | Graphite, WS$_2$ | 5 N | 0.16 | [15] |
| Steel | MoS$_2$ | 12 N | 0.08, $2.7 \times 10^{-7}$ mm$^3$/Nm | [18] |
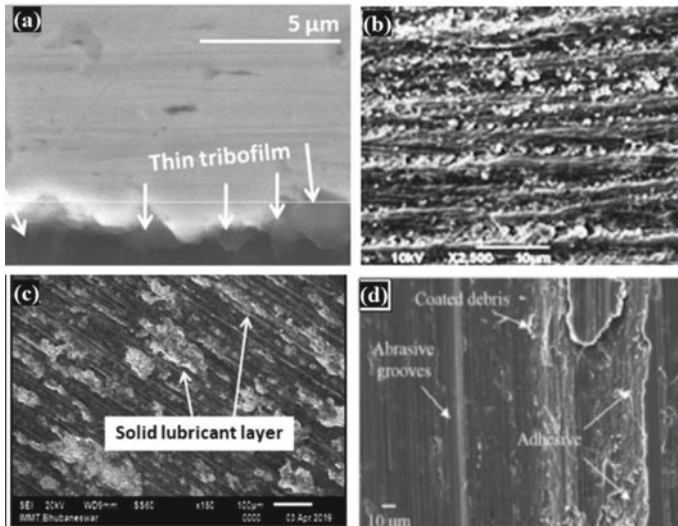


**Fig. 1** Wear images of **a** CU–rGO–MoS$_2$ [19], **b** LM16–SiC–Ni–Gr [20], **c** Al–SiC–h-BN [9], and **d** Al–SiC–Gr [17]

gateway for designing self-lubricating automotive parts but also help to design new electronic components and technology. Self-lubricating composites in addition with micro- and nano sized Graphite, MoS$_2$, WS$_2$, hexagonal BN, or other strong lubricant MMCs can be used in Cylinder liners, pistons, cv joints, equipment surfaces which can replace the liquid lubrication system [2].

However, a few challenges are still pivotal for self-lubricating composites. Addition of CNTs, Graphene, MoS$_2$, and WS$_2$ through liquid metallurgy processing

method is difficult as these additives are highly reactive with molten matrices. Agglomeration of $MoS_2$ and WS2 particles is a major problem during solid processing method [15]. Moreover, other sources of carbon like graphene and CNTs are costly in comparison with graphite and result in high production cost [16]. Although graphite provides reduced wear rate and COF at very low cost but in contrary, the mechanical properties decreased. Such deficiencies should be overcome by adding hard particles such as SiC and $Al_2O_3$ into Al + Gr composites [17]. Self-lubricating composites with hBN has a non-wetting property, which makes it extremely difficult to achieve greater interface strength. The previous studies indicate that magnesium added enhances the composite's wettability. There are several papers reporting on self-lubricating composites, but mainly focused on the mechanical or tribological effect of solid lubricants. The potential reactions between solid lubricants and matrices that could result in the loss of lubrication characteristics of solid lubricants have hardly been discussed by researchers. There is a vast scope for exploring the self-lubricating hybrid composites with better mechanical and tribological properties at a low cost.

# References

1. Omrani E, Moghadam AD, Menezes PL, Rohatgi PK (2016) Influences of graphite reinforcement on the tribological properties of self-lubricating aluminum matrix composites for green tribology, sustainability, and energy efficiency—a review. Int J Adv Manuf Technol 83(1):325–346
2. Dorri Moghadam A, Schultz BF, Ferguson JB, Omrani E, Rohatgi PK, Gupta N (2014) Functional metal matrix composites: self-lubricating, self-healing, and nanocomposites-an outlook. Jom 66(6):872–881
3. Sahoo S (2021) Self-lubricating composites with 2D materials as reinforcement: a new perspective. Reinf Plast 65(2):101–103
4. Moorthy AA, Natarajan N, Palani PK, Suresh M (2013) Study on tribological characteristics of self-lubricating aa2218–fly ash–white graphite composites. Int J Eng Technol 5(5):4193–4198
5. Moghadam AD, Schultz BF, Ferguson JB, Omrani E, Rohatgi PK, Gupta N (2014) Functional metal matrix composites: self-lubricating, self-healing, and nanocomposites-an outlook. Jom 66(6):872–881
6. Furlan KP, da Costa Gonçalves P, Consoni DR, Dias MVG, de Lima GA, de Mello JDB, Klein AN (2017) Metallurgical aspects of self-lubricating composites containing graphite and $MoS_2$. J Mater Eng Perform 26(3):1135–1145 (2017)
7. Moazami-Goudarzi M, Nemati A (2018) Tribological behavior of self-lubricating $Cu/MoS_2$ composites fabricated by powder metallurgy. Trans Nonferrous Metals Soc China 28(5):946–956
8. Tjong SC (2013) Recent progress in the development and properties of novel metal matrix nanocomposites reinforced with carbon nanotubes and graphene nanosheets. Mater Sci Eng R Rep 74(10):281–350
9. Sahoo S, Samal S, Bhoi B (2020) Fabrication and characterization of novel Al-SiC-hBN self-lubricating hybrid composites. Mater Today Commun 25:101402
10. Wozniak J, Kostecki M, Cygan T, Buczek M, Olszyna A (2017) Self-lubricating aluminium matrix composites reinforced with 2D crystals. Compos B Eng 111:1–9
11. Xiao JK, Zhang W, Zhang C (2018) Microstructure evolution and tribological performance of $Cu-WS_2$ self-lubricating composites. Wear 412:109–119

12. Biswal SR, Sahoo S (2022) Structural and mechanical properties of a novel Al-Al$_2$O$_3$-WS$_2$ hybrid composites. Mater Lett 307:131017
13. Biswal SR, Sahoo T, Sahoo S (2021) Prediction of grain boundary of a composite microstructure using digital image processing: a comparative study. Mater Today: Proc 41:357–362
14. Biswal SR, Sahoo S (2020) Fabrication of WS$_2$ dispersed Al-based hybrid composites processed by powder metallurgy: effect of compaction pressure and sintering temperature. J Inorg Organomet Polym Mater 30(8):2971–2978
15. Cao H, Qian Z, Zhang L, Xiao J, Zhou K (2014) Tribological behavior of Cu matrix composites containing graphite and tungsten disulfide. Tribol Trans 57:1037–1043
16. Khanna V, Kumar V, Bansal SA (2021) Mechanical properties of aluminium-graphene/carbon nanotubes (CNTs) metal matrix composites: advancement, opportunities and perspective. Mater Res Bull 138:111224
17. Zhou MY, Ren LB, Fan LL, Zhang YWX, Lu TH, Quan GF, Gupta M (2020) Progress in research on hybrid metal matrix composites. J Alloy Compd 838:155274
18. Singh N, Sinha SK (2021) Tribological performances of hybrid composites of epoxy, UHMWPE and MoS$_2$ with in situ liquid lubrication against steel and itself. Wear 486:204072
19. Nautiyal H, Kumari S, Tyagi R, Rao US, Khatri OP (2021) Evaluation of tribological performance of copper-based composites containing nano-structural 2D materials and their hybrid. Tribol Int 153:106645
20. Mahaviradhan N, Sivaganesan S (2021) Tribological analysis of hybrid aluminium matrix composites for high temperature applications. Mater Today: Proc 39:669–675